FEASIBILITY OF A BONE MINERAL MEASUREMENT TECHNIQUE BASED ON COHERENT SCATTERING OF GAMMA RAYS

By

ALOIS MARSHALL N. NDLOVU, B.Sc., M.A.Sc.

A Thesis

Submitted to the School of Graduate Studies

in Partial Fulfilment of the Requirements

for the Degree

Doctor of Philosophy

McMaster University

BONE MINERAL MEASUREMENT BASED ON COHERENT SCATTERING

DOCTOR OF PHILOSOPHY (1990)
(Physics)

MCMASTER UNIVERSITY
Hamilton, Ontario

TITLE: Feasibility of a Bone Mineral Measurement Technique Based on Coherent Scattering of Gamma Rays

AUTHOR: Alois Marshall N. Ndlovu
M.A.Sc. (National University of Ireland, Dublin)

SUPERVISOR: Professor C.E. Webber

NUMBER OF PAGES: xix, 258

ABSTRACT

The investigation of the feasibility of a bone mineral measurement technique based on coherent scattering of gamma rays was performed using a HPGe detector.

Considerations of detector efficiency and resolution, absorbed dose to bone, spectral separation between coherent and Compton peaks, variation of differential coherent cross section and scattering volume with scattering angle led to the selection of a photon source energy of 103.2 keV (Sm^{153}) and a scattering angle of 40^{o}.

Bone phantoms (aqueous solutions of K_2HPO_4) were used to examine how the coherent intensity emanating from a scattering volume at the centre of an object varied with object dimensions and solution effective atomic number. Simulation and experimental measurements with solutions in cylindrical polyethylene containers of varying sizes indicated that the ratio of the coherent count rate to the transmission count rate was independent of container dimensions (at least up to 7 cm diameter). For ease of comparison, all the ratios at different concentrations were normalised to that of water obtained in an identical measurement geometry. The normalised coherent-to-transmission ratios were related to solution effective atomic number by a power function with an exponent of 3.30 ± 0.15.

When the rate of change of the normalised ratio with effective atomic number is used as an indicator of the sensitivity of the technique, the coherent-to-transmission method is almost twice as sensitive as a coherent-to-Compton technique.

In-vitro bone mineral measurements were made in the calcaneus (heel bone), an easily accessible site in which 90% of bone mineral is trabecular. Prior to the measurements the spatial distribution of mineral was investigated with a Norland 278-A single photon absorptiometry (SPA) machine in slices of several calcanei. Cortical bone was restricted to a thin peripheral region of the calcaneus.

Three whole calcanei, one of which had its calcium content deliberately reduced by soaking overnight in hydrochloric acid, were selected for measurement using the coherent-to-transmission technique. For the first measurement each bone was submerged in water only. For the second measurement the trabeculae were filled with corn oil, to simulate marrow fat, and again each bone was submerged in water. The latter measurements were about 50% lower than the first, indicating a large "marrow fat" effect. However, both sets of results can be explained by assuming a power relationship between the normalised coherent-to-transmission ratio and the effective atomic number of the scattering

volume contents.

Cuboid samples of side approximately 16 mm were cut out of the posterior region of each calcaneus and ashed. A plot of the normalised coherent-to-transmission ratio versus the ashed weight per unit volume (bone mineral density) of the three calcanei yielded a straight line. While this indicates that the normalised coherent-to-transmission ratio is an indicator of bone mineral, a larger number of samples will be required to establish a robust calibration curve.

ACKNOWLEDGEMENTS

It is a pleasure and a privilege to be a student of Professor C.E. Webber. I thank him unreservedly for his sound advice, his cheerful guidance and his boundless patience.

My gratitude also extends to the other members of my supervisory committee, Professors W.V. Prestwich and M.S. Patterson for their valuable suggestions and probing questions. I would also like to thank the staff of the McMaster Reactor and Health Physics and Kenrick Chin at the Nuclear Research Building for sorting out some of my technical problems.

Thanks are due to my colleagues, Jeff Johansson, Ted Sokolowski, Dave Beachey, Peter Williams, John Benjamins etc., and special thanks to Tom Farrell for his incisive comments and ideas.

Thanks are also due to the staff in the Physics Department Office and all the guys, too numerous to mention individually, in the Hamiltonian Operators soccer squad and the baseball teams "Degenerate States" and "Nuclods". They all made me feel at home.

Most important of all, I wish to express my heartfelt gratitude to my family, my wife Happiness and daughter Noma for their patience and understanding. Without their selfless support, materially and emotionally, this task

would have been almost impossible to complete.

Finally, I wish to say "thank you" to Cheryl McCallion who did a brilliant job of typing this manuscript.

DEDICATED TO THE MEMORY OF
my dear brother, Rabson
my witty uncle, Alex
and my buddy and cousin, Roy

TABLE OF CONTENTS

LIST OF ILLUSTRATIONS

LIST OF TABLES

CHAPTER 1

METHODS OF IN VIVO BONE MASS MEASUREMENT

1. Introduction

For the majority of people, especially women, reduction of bone mass is an inevitable result of aging and leads to an increased risk of bone fracture. These osteopenic fractures, especially those involving the proximal femur, carry a high morbidity and an increased mortality. Over the years sustained efforts have been made to develop methods that will identify those individuals with low bone mass. Once identified it is necessary to quantitate the progression of the condition and monitor response to therapy.

By and large, the desirable features of an ideal method depend upon the clinical reason for the measurement. For the initial diagnosis of reduced mass the measurement must be accurate and able to predict a normal or expected value for a given individual. On the other hand if the clinical intention is to monitor disease progression or to evaluate response to therapy the measurement must be precise and accuracy is not of the utmost importance. Other features of an ideal method are low radiation dose and low monetary cost and for purposes of mass-screening, simplicity

(to perform) and convenience for the patient.

Metabolic bone diseases like osteoporosis are a result of loss of bone mineral from both compact bone and trabecular bone. The remodelling rate of trabecular bone is about eight times that of compact bone (ICRP #23, 1974), thus when bone mineral concentration falls, the changes in both the effective atomic number and the physical density of bone will be first manifest in the former compartment (Frost, 1966; Rasmussen et al., 1974).

Measurements of total and/or partial attenuation coefficients of beams of gamma rays through bone have led to the development of techniques to measure bone mineral concentration and bone density (Cameron and Sorenson, 1963; Garnett et al., 1973; Clarke and Van Dyk, 1973; Webber and Kennett, 1976; Puumalainen et al., 1976). In theory, all photon attenuation mechanisms can be used as a basis for a non-invasive assessment of the concentration of bone mineral in trabecular bone (Webber, 1979). The decision as to which mechanism to exploit depends on, among other things, the sensitivity of each mechanism to changes in the effective atomic number and physical density of bone. The partial attenuation coefficients depend, approximately, upon density (Compton scattering), the product of effective atomic number and density (pair production) and the product of density and the square of the effective atomic number (Coherent

scattering). Thus a technique based on coherent scattering should be the most sensitive to changes in bone mineral concentration.

In the past few decades a number of techniques have become available for the assessment of bone mass. Some of these methods are reviewed in the next sections.

1.2 Bone Biopsy

Postmenopausal women often suffer vertebral, wrist and hip fractures. These are due to excessive loss of bone mass at menopause (Type 1 osteoporosis) or to a low bone mass (as a consequence of aging or of a reduced peak bone mass (Type 2 osteoporosis). A sample of bone mass taken from one site may reflect changes occurring in the skeleton at large. This has led to the use of the random biopsy in the histological evaluation and analysis of the middle-aged or s¢enescent osteopenic skeleton. In some centres bone biopsy has become the diagnostic procedure of choice in the evaluation of idiopathic osteoporosis because it allows precise quantitative and qualitative evaluation of the bone and marrow in a disorder often accompanied by normal values of various serum and urine biochemical indicators.

The iliac bone is the preferred site for the purposes of standardisation of data. A proper biopsy is performed with a trocar and must be a full thickness and adequate size

to result in a 6mm x 4 mm core and provide enough tissue for quantitative analysis. The site of the biopsy is at a locus 3.5 to 4 cm inferior and posterior to the anterosuperior iliac spine. Five micron-thick slices are taken from the specimen for histological examination. It may be stained for standard light microscopy of bone and marrow or it may be examined by polarised light microscopy, to evaluate the presence of woven bone and crystals, (indicators of classical Paget's disease, osteitis fibrosa and tumour).

Osteoporosis is a histological entity defined as a decreased mass of normally mineralised bone. The quantity of bone matrix per unit marrow space is diminished but the ratio of osteoid to calcified tissue is normal. Osteomalacia on the other hand is a separate histological entity and has osteoid accumulation due to a decrease in the rate of mineralisation. Osteomalacic bone also contains an increased quantity of uncalcified matrix. The nondecalcified biopsy was developed to distinguish osteoporosis from osteomalacia.

Bone is synthesised by the deposition of organic matrix (osteoid) which is subsequently mineralised. The mineralisation lag time is the duration between deposition of a molecule of osteoid (which is largely collagen) and its subsequent calcification. This period averages 23.5 days in man and is markedly increased in osteomalacic disease. This

is a useful distinguishing factor which is discussed further later.

Bone mineral is deposited at the calcification (mineralisation) front at the interface of osteoid and calcified matrix. The antibiotic tetracycline binds newly deposited immature bone mineral, probably by chelating calcium, and appears as a yellow-orange line at the calcification front when examined by fluorescence microscopy. Osteoid seams actively undergoing mineralisation will show a tetracycline label, while there will be no fluorescence at calcification fronts not being mineralised. An abundance of nonfluorescing calcification fronts is an indication of osteomalacia. Information regarding the rate of mineralisation is obtained by using time-spaced histological mineralisation markers. Prior to biopsy, two courses of the antibiotic are administered, separated by a known period of time, typically 14 days. This results in the appearance of two parallel fluorescent bands adjacent to the mineralising osteoid seams, the deeper one representing the first course of the drug and the more superficial one representing the second course. Dividing the mean distance between the fluorescent bands by the inter-dose time gives the cellular rate of mineralisation at the average point on the bone-forming surface. This kinetic determinant of calcification is diminished in osteomalacia,

indicating prolonged mineralisation lag time.

If the bone is evaluated histomorphometrically, light microscopy with planimetry is used to evaluate bone volume. In osteoporosis, trabecular bone volume and mean trabecular bone volume is decreased. In osteomalacia, trabecular osteoid surface, trabecular bone volume and mineralisation lag time are all elevated and calcification rate is decreased.

The most serious disadvantage of bone biopsy is that the same skeletal site cannot be re-sampled. Furthermore it is invasive and entails trauma. It has become evident that skeletons of postemenopausal osteopenic females are histologically diverse. In inexperienced hands the accuracy and/or precision of any interpretation of histological changes can only be considered tentative.

1.3 Non-Invasive Techniques

The basis of most of the current non-invasive methods of bone mass/mineral content measurement is the interaction of electromagnetic radiation with tissue. For the energy range of use in diagnostic radiology, photons of electromagnetic radiation interact with atoms of tissue by three main processes; photoelectric absorption, coherent (Rayleigh) scattering and incoherent (Compton) scattering. The interaction cross section for each of these processes

depends on the energy of the incident radiation and the average or effective atomic number and density of the tissue. The majority of the measurement techniques that will be outlined below, can be classified according to whether the detected radiation has been scattered (coherently or incoherently) or transmitted.

1.3.1 Photon Absorptiometry

The techniques of photon absorptiometry are based on the premise that bone mineral content is assumed to be directly proportional to the fraction of incident photons that interact with the bone being studied. There are two absorptiometry techniques; single and dual photon absorptiometry.

1.3.2 Single Photon Absorptiometry

This technique was first introduced by Cameron and Sorenson (1963). Single photon transmission measurements are limited to the appendicular skeleton rather than the axial skeleton. The method employs measurement of a narrow (<5 mm) diameter beam of monoenergetic photons with a well collimated detector. The beam is scanned across a limb, usually the forearm. The highly collimated pencil beam virtually eliminates scattered radiation and its monochromaticity eliminates beam hardening perturbations in

the linear attenuation coefficient as the beam passes through the limb. Beam hardening was a severe problem in earlier techniques which relied on x-ray sources. The limb is immersed in water or encased in a tissue-equivalent bolus because there must be a constant layer of tissue plus bone for the measured changes in the beam intensity to be directly related to the bone mineral content in the beam path.

Calculation of bone mass in grams per centimetre can be made if the density and the mass absorption coefficients of bone mineral and soft tissue are known or obtained from a calibration standard. The amount of bone mineral, m_b, in the photon beam path is given by the equation;

$$m_b = \rho_b \ell n\left(\frac{I_o}{I}\right) / (\mu_b \rho_b - \mu_s \rho_s) \qquad (1.1)$$

where I_o and I are the incident and emergent beam intensities; μ_b and ρ_b are the mass attenuation coefficient and the density of bone mineral and μ_s and ρ_s are the same parameters for soft tissue. The units of m_b are grams per square centimetre. In clinical use the beam is scanned across a limb and a series of measurements of m_b are summed to yield the bone mineral content in units of grams per square centimetre. Derivation of the bone width from the scan enables the conversion of mineral mass to units of

grams per centimetre. Because the basic assumption of the method is that the limb is composed only of soft tissue and bone mineral, serious errors can arise when a high fat content influences soft tissue composition (Lahtinen et al. 1980). This may occur in bones with low mineral content. Since the photon path length must be constant and since fat content must be low, single photon absorptiometry is limited to appendicular bone.

The result of the bone mineral mass measurement depends on both the extent of osteopenia and the size of the bone. The dependence of bone mineral mass on bone size necessarily means it is a function of age, height, sex and muscle mass (Christiansen et al., 1981). It therefore follows that there will be a large variance in normal and abnormal groups.

The accuracy of single photon absorptiometry is between 1% and 3% when compared to the ashweight of postmortem bone (Shimmins et al., 1972) or to the dry weight of bones (Mazess 1971). The precision of the repeated measurements is good, 2-3%, and is mostly determined by errors of repositioning for repeated measurement at the same site. Precision deteriorates considerably at sites which contain a significant fraction of trabecular bone. This is due to the fact that the cross sectional shape changes rapidly along such peripheral bones as the distal radius.

There is good correlation between cortical bone mass measured in the radius and other cortical sites such as the femoral neck, (r=0.90 Mazess 1981). Radial bone mass and total body calcium measured by neutron activation correlate well in normals, (r=0.85) but not so well in spinal osteoporotics. The technique of single photon absorptiometry has proved useful for serial measurements because of its good precision but the large overlap between osteoporotics and age-matched controls limits its diagnostic capabilities (Christiansen et al., 1981; Wahner et al., 1977; and Mazess 1981). Furthermore, the method as currently used reflects the status of peripheral long bones and effectively measures cortical bone. Thus the measurement may not have much or any bearing on overall skeletal status, especially that of labile trabecular bone.

1.3.3 Dual Photon Absorptiometry (DPA)

In dual photon (dichromatic) absorptiometry, the source emits photons at two distinct energies and transmission measurements are made at each energy. Conceptually it is an extension of the single photon absorptiometry technique and the dichromaticity eliminates the need to have a constant thickness of soft tissue around the bone. This in turn enables measurements to be made in hitherto inaccessible sites such as the spine and the

femoral neck. The measurement still relies on the premise that the object consists only of bone mineral and soft tissue. Thus a correction must be applied for each individual as the ratio of fat to lean in soft tissue varies considerably from person to person. This has reportedly been achieved by use of an iterative technique using information collected during the measurement procedure (Peppler and Mazess, 1981). Nevertheless variations in fat content within one individual between sites where there is no mineral and sites where mineral is present will lead to errors (Farrell and Webber, 1989).

1.3.4 Mathematical Theory of DPA

It is assumed that radiation quality and radiation geometry are such that both photon energies are exponentially attenuated during passage through the patient who can be considered as being composed of multiple attenuating media, m_i. Assuming a narrow beam geometry, the generalised equation for the transmission intensity is given by;

$$I_n = I_{o,n}\exp\left(-\sum_{i=1}^{k} \mu_{i,n} m_i\right) \qquad (1.2)$$

where $I_{o,n}$ is the incident unattenuated intensity of the nth photon energy; $\mu_{i,n}$ is the mass attenuation coefficient of the ith attenuating material at the nth photon energy; m_i is

the mass per unit area of the ith material and k is the number of materials. I_n is the emergent attenuated intensity of the nth photon energy.

In order to obtain a unique solution in a system of equations (linear) there must be as many independent equations as there are unknowns. Thus for a two media system with components b and s, two discrete energies must be employed. Solving equation 1.2 for m_b gives:

$$m_b = \frac{\ln\left(\frac{I_{o1}}{I_1}\right) - \left(\frac{\mu_{s1}}{\mu_{s2}}\right) \ln\left(\frac{I_{o2}}{I_2}\right)}{\mu_{b1} - \left(\frac{\mu_{s1}}{\mu_{s2}}\right) \mu_{b2}} \qquad (1.3)$$

Equation (1.3) maintains the same system as equation (1.2); b denotes bone and s denotes soft tissue. M_b represents the total mineral in a column 1 cm in cross sectional area. It is the mineral mass in the beam at each point in the scan when expressed as the amount of mineral per square centimetre scanned. Although it is frequently called the bone mineral density, its units are g/cm^2. There is a wide range of normal BMD values reported for dual photon absorption methods. The normal DPA values for BMD (lumbar spine) are 1.2 - 1.6 g/cm^2 (age 30) and 0.9 - 1.3 (age 60) (Wahner, 1987).

If fat is present in scanned tissue the body should

be categorised into three distinct components. With only two distinct energies present in the incident beam, the attenuated photon beam intensities become:

$$I_1 = I_{o1} \exp(-[\mu_{s1}m_s+\mu_{f1}(m_f-m_{fo})+\mu_{b1}m_b]) \qquad (1.4)$$

$$I_2 = I_{o2} \exp(-[\mu_{s2}m_s+\mu_{f2}(m_f-m_{fo})+\mu_{b2}m_b]) \qquad (1.5)$$

where s, b and f represent soft tissue, bone and fat respectively. The constant m_{fo} is included to indicate that if the mass of fat m_f is constant throughout the scanned area, the effect of fat can be mathematically eliminated. The simultaneous equations (1.4) and (1.5) can be solved to give the mass of bone as follows;

$$m_b = \frac{\ln(\frac{I_{o1}}{I_1}) - (\frac{\mu_{s1}}{\mu_{s2}})\ln(\frac{I_{o2}}{I_2})}{\mu_{b1} - (\frac{\mu_{s1}}{\mu_{s2}})\mu_{b2}} + \frac{[(\frac{\mu_{s1}}{\mu_{s2}})\mu_{f2}-\mu_{f1}](m_f-m_{fo})}{(\frac{\mu_{s1}}{\mu_{s2}})\mu_{b2}-\mu_{b1}} \qquad (1.6)$$

If the measurements are made where m_b is equal to zero then the second term in equation (1.6) can be evaluated. This value can then be applied to those regions where bone mineral is present. It must be noted that if fat thickness is not constant, then a third energy (hence a third equation in addition to equations (1.4) and (1.5) would be required. The feasibility of triple photon absorptiometry has been examined (Farrell, 1990).

For ashed bone samples in a phantom containing an oil and water mixture, DPA gave a very good correlation (r=0.99) between ashweight and bone mineral density (Dunn et al., 1980) and a precision of 5% was obtained in a reference spine (Prince et al., 1976). For a measurement of bone mineral density in the spinal region, DPA provides a lower dose and a greater precision than other methods like computerised tomography and neutron activation analysis (Roos et al., 1974; Wilson et al., 1977; Krolner and Nielsen 1980; Mazess, 1979). The spine is advocated as the preferred location for clinical monitoring and diagnosis of loss of bone mineral as it is the site most susceptible to spontaneous fracture attendant to osteopenia. In addition it consists predominantly of trabecular bone which has a turnover rate about eight times that of cortical bone. This higher turnover rate means that trabecular bone is more susceptible to physiological changes than cortical bone. It must be emphasised that absorptiometry measures an integral of the cortical and trabecular bone in the scan path.

1.4 Neutron Activation

Measurement of partial or total body calcium can be done using the technique of neutron activation analysis. Neutron irradiation of the rare stable isotope ^{48}Ca (0.18% abundance) present in uniform concentration in common

calcium converts, ^{48}Ca to radioactive ^{49}Ca, according to the reaction;

$$^{48}Ca(n,\gamma)^{49}Ca \qquad (1.7)$$

The induced activity is then measured following the decay of ^{49}Ca according to the equation;

$$^{49}Ca \xrightarrow[T1/2=8.9min]{\beta} {}^{49}Sc + 3.1\ MeV(\gamma) \qquad (1.8)$$

^{49}Ca activity can be interpreted directly as an indicator of skeletal mass since calcium is a constant fraction (38%) of bone mineral. This interpretation is only valid in the absence of extra-osseous calcification.

Neutron activation can be used to measure calcium in portions of the body such as the hand or the torso. Determination of calcium in the hand is the simplest of the neutron activation methods and produces the lowest radiation exposure to the individual. It also allows normalisation for size by determination of hand volume. Precision is about 3-5% and accuracy is only about 5% (Mazess, 1981). Neutron Activation is plagued by problems ranging from high local dose ($\simeq$0.03 Sv), to lack of uniformity of both neutron flux and counting geometry.

Partial body (torso) activation (a compromise between hand and total body irradiation) measures calcium in the

trunk and upper thigh. It is simpler than total body neutron activation and since the spine is a larger fraction of the irradiated tissue in this technique, the response is more sensitive to changes in trabecular bone than is the response of the hand or the total body. However there may be substantial errors of repositioning.

The total body neutron activation technique measures total body calcium directly. The subject is uniformly exposed to a beam of partially moderated neutrons. The induced ^{49}Ca activity is measured with a whole body counter. The accuracy of this technique, determined using anthropomorphic phantoms was found to be about 5% (Williams et al., 1978). Changes in subject body thickness affects both diagnostic and sequential measurements and will thus adversely affect precision. As with partial body calcium measurements, total body calcium depends on body size, sex, age and degree of skeletal osteopenia. Measured values must be normalised for these factors so that the relative deficit in skeletal mass can be determined for each individual.

Among the limitations of this method are: 1) its relatively high expense, 2) its inability to reveal that a change may be confined to a small region of the body and 3) it cannot distinguish ectopic calcification, a common condition in patients afflicted with renal osteodystrophy.

Some laboratories make use of the following reaction

to measure total body calcium;

$$^{40}Ca + n \rightarrow {}^{37}Ar + {}^{4}He \qquad (1.9)$$

The ^{37}Ar exhaled from the body is measured with proportional counters. Current methods are tedious and time consuming. The technique has a potential for measurement of bone mass changes in the spinal column, if only the problem of collecting completely the induced ^{37}Ar activity can be resolved.

1.5 Compton Scattering

This method is based on the principle that the fraction of a beam of monochromatic photons which is scattered by an object depends upon the electron density of that object. The number of scattered photons (N) detected by a detector at a fixed angle depends on the number of electrons in a sensitive volume (V) defined by the intersection of the projections of the source and detector collimators. The electron density, ρ_e, is given by the equation;

$$\rho_e = \frac{ZN_o\rho}{A} \qquad (1.10)$$

where Z is the atomic number of the scatterer (object), A is the atomic mass number, N_o is Avogadro's number and ρ is the

scatterer's mass density. The number of scattered photons N, (at fixed angle) have a reduced energy relative to the incident photons but are still monochromatic.

$$N \alpha \sigma_c \rho_e V \qquad (1.11)$$

where σ_c is the Compton cross section per electron and is constant for a fixed angle, ρ_e is the electron density and V is the scattering volume. Combining equations (1.10) and (1.11) one gets;

$$N \alpha \frac{Z\rho}{A} \qquad (1.12)$$

which indicates that if Z/A is constant for each element within the sample volume, then the number of scattered photons from that volume depends only on the mass density.

The density of bone can be determined by taking the ratio of the number of photons scattered from bone to the number scattered from a calibration standard, usually water. That is,

$$\rho_b = \{(Z/A)_w N_b\}/\{(Z/A)_b N_w\} \qquad (1.13)$$

where the subscripts b and w refer to bone and water respectively.

Corrections have to be made for attenuation of the incident photons before they are scattered and of the scattered photons before they are detected. These

corrections make the measured density independent of the thickness and the attenuation properties of tissue surrounding the sensitive (scattering) volume. The big advantage of this technique is that a restricted, geometrically defined volume may be positioned entirely within trabecular bone and as a result the mass concentration of trabecular bone alone can be measured. The density measured is the average of both inorganic and organic components of the volume of bone studied. This is the greatest problem since the volume of organic components is typically at least twice that of the inorganic.

Repositioning of the scattering volume within a bone like the calcaneus is relatively simple and the measurement is thus not a function of the thickness of the bone nor of its possible rotation. The precision of the method is so high, 1 to 3%, that the small congenitally determined difference between the right and left calcaneii can be detected in vivo (Webber and Garnett, 1976). The accuracy of the technique is about 5% (Webber and Kennett, 1976; Garnett et al., 1973).

One of the problems of the method is the evaluation of the contribution of the multiply scattered photons. This is particularly problematic when the bone studied differs from the calibration standard. In the Compton scattering technique the result obtained is an average density of all

substances present within the scattering volume.

1.6 Radiographic Photodensitometry

The technique estimates bone mass from a comparison between optical densities of radiographic images of bones and of a reference aluminum wedge. It is probably the oldest non-traumatic method of assessing bone mineral (Oeser et al., 1963). A strict standardisation of kilovoltage, exposure time and film processing is of prime importance in these measurements since routinely obtained radiographs vary widely in optical lucency (Anderson et al., 1966). The use of an aluminum wedge accounts, in part, for some of these factors. The measurements on the radiograph are made either with a densitometer as spot measurements or with a more sophisticated instrument as line or area measurements.

The bone mineral density in normal subjects measured from a combination of morphometry and film densitometry agrees with the ash content per unit volume of bone (Meema and Meema, 1969). For bone with little soft tissue covering, for example, phalanges, a precision of 5 to 10% can be achieved. Increasing overlying tissue seriously compromises both accuracy and precision because of scattered radiation. While useful measurements of clinical value can be obtained (Meema and Meema, 1975; Cohn, 1981) interest in photodensitometry has declined.

1.7 Computerised Tomography (CT)

Bone mineral determinations by computed tomography measure the spatial distribution of linear attenuation coefficients in a transaxial plane through the patient. Image planes are reconstructed from multiple measurements of the transmission of electromagnetic radiation through the object. These transmission (attenuation) measurements can be achieved using fixed or moving sources and fixed or moving detectors. From each of the many positions, attenuation results are used to calculate a back projection which provides the cross sectional image. Measured coefficients depend on the electron density and upon the effective atomic number of the tissue. Consequently the mass of material of relatively high atomic number within a region defined from the image can be determined. The region of interest can be located within the trabecular bone of a vertebral body, if this is desired.

1.7.1 Simplified Theory of the CT Method

CT is based on the relationship between the linear attenuation coefficient $\mu(E)$, of a mixture of compounds and the concentrations of each compound. A dimensionless number, H, known as the CT number is obtained which is a function of the linear attenuation coefficients of the mixture μ_m, water μ_w and air μ_a and is calculated from the

expression:

$$H = \frac{(\mu_m - \mu_w)\ 1000}{\mu_w - \mu_a}$$

In the single energy CT measurement of bone mineral it is assumed that the bone "mixture" consists of water-equivalent soft tissue and bone mineral. Bone mineral concentration, c_b, in the mixture is then given by the equation below;

$$c_b = \frac{\rho_b[H_{bm}(V) - H_{st}(V)]}{H_b(V) - H_{st}(V)} \qquad (1.14)$$

where $H_b(V)$ is the CT number of pure bone mineral at the tube potential V, $H_{st}(V)$ is the CT number of water-equivalent soft tissue, $H_{bm}(V)$ is the measured CT number of the bone mixture and ρ_b is the density of pure bone mineral. In reality, $H_b(V)$ and $H_{st}(V)$ are determined with a phantom containing mineral-equivalent components, such as dipotassium hydrogen phosphate (K_2HPO_4), scanned at the same time as the patient. The CT number for the selected region of interest in the patient's scan is then converted into a "mineral-equivalent" concentration. Fat content in the vertebrae is substantial and variable, so that the premise on which the technique is based, namely that body tissues consist entirely of bone mineral and water-equivalent soft tissue, is bound to lead to considerable error.

The dual energy CT method determines the CT numbers in a region of interest at two x-ray tube potentials. The linear set of "mixture-rule" equations, containing the fat contributions and generated at the two values of tube potential, are then solved simultaneously. While it is possible to correct for unknown fat content using the dual energy CT technique (since the linear attenuation coefficient for bone mineral is much more dependent on energy than that of fat or soft tissue), dual energy CT has the disadvantage that it doubles the radiation dose which is already substantial. In any case the precision of dual energy CT is considerably lower than that of single energy CT. Single energy CT seems acceptable for sequential measurements in a single subject but the development of a low dose, high accuracy, dual energy CT technique is crucial for diagnostic purposes. Gennant et al. (1985) have published normal bone mineral density values of 175±28 mg/cm^3 and 125±28 mg/cm^3 for younger and older women respectively.

Since vertebral bodies are not homogeneous and the mineral content of a CT slice varies with location (Bradley et al., 1978), one considerable difficulty in CT measurements is the positioning of the imaged tissue slice in the same location for sequential studies in a single subject and in the same relative position for diagnostic

measurements in groups of subjects. Some workers (Gennant et al., 1981), have developed advanced computer software to define consistently the same volume of bone within a vertebral bone.

1.8 Coherent/Compton Scattering Ratio Technique

This technique was first used for bone measurements by Puumalainen et al., (1976). As in the Compton method, the signal originates from a scattering volume defined by the intersection of the projections of the source and the detector collimators. It is thus more sensitive to the individual localised variations in object composition than a transmission method in which the signal is integrated along the beam path through the object. The coherent (Rayleigh) scattering cross section, σ_R, varies approximately as Z^2, where Z is the atomic number. The Compton cross section, σ_C, varies linearly with Z and so the ratio of signal intensities, I_R/I_C, varies as Z, where I_R and I_C are the measured intensities of the Rayleigh (coherent) and Compton signals respectively. The ratio minimises or eliminates several systematic errors in the measurement; for instance changes in the scattering volume and absorption along the incident and scattered beam paths.

1.8.1 Theory of the Technique

In the Rayleigh scattering process, photons are scattered by bound atomic electrons and the atom is neither ionised nor excited. A fuller discussion of the process is given in Section 2.4. The angular or differential Rayleigh scattering cross section, $d\sigma_R(\theta)/d\Omega$, is obtained by multiplying the differential Thomson cross section per electron,

$$\frac{d\sigma_T}{d\Omega} = \frac{1}{2} r^2(1 + \cos^2\theta)$$

by the square of the atomic form factor, $F(x,Z)$ to obtain the following equation:

$$\frac{d\sigma_R(\theta)}{d\Omega} = \frac{1}{2} r^2(1+\cos^2\theta)[F(x,Z)]^2 \text{ cm}^2/\text{atom/ster} \quad (1.15)$$

where θ is the scattering angle, r is the classical electron radius, Z is the atomic number of the scatterer, $x=(1/\lambda)\sin(\theta/2)$ is the momentum transfer parameter and λ is the wavelength of the incident radiation. The form factor is discussed in detail in section 2.4.1. The differential Compton scattering cross section, $[d\sigma_C(\theta)/d\Omega]$, is given by the product of the Klein-Nishina equation and the incoherent scattering function, $S(x,Z)$. The latter accounts for departures from the Klein-Nishina relation that occur at low

incident photon energies (see Section 2.5.2) due to the effects of electron binding.

$$\frac{d\sigma_C}{d\Omega} = \left(\frac{1}{2}r^2[1+k(1-\cos\theta)^{-2}[1+\cos^2\theta + \frac{k^2(1-\cos^2\theta)^2}{1+k(1-\cos\theta)}\right. \left.[S(x,Z)]\right) \tag{1.16}$$

where k is the photon energy in units of electron rest mass energy, mc^2. The coherent to Compton ratio can be expressed as a function of photon energy, the scattering angle and the atomic number of the scatterer by simply dividing equation 1.15 by equation 1.16 to obtain the following expression:

$$\frac{d\sigma_R}{d\sigma_C} = \frac{\{[1+k(1-\cos\theta)^2(1+\cos^2\theta)[F(x,Z)]^2\}Z}{\{1+\cos^2\theta+[k^2(1-\cos\theta)^2]/[1+k(1-\cos\theta)]\}S(x,Z)} \tag{1.17}$$

The effect of multiple scattering in a sample of significant thickness is such that in actual measurements, even with narrow beam geometry, the observed ratio is smaller than the calculated ratio. The ratio is still proportional to the value $d\sigma_R/d\sigma_C$ for a given scatterer, incident energy and scattering angle. The total atomic cross sections for coherent (σ_R) and Compton (σ_C) scattering can be approximately expressed as:

$$\sigma_R \simeq C_1 Z^n/E^m \tag{1.18}$$

and

$$\sigma_C \simeq C_2 Z \tag{1.19}$$

where C_1 is a constant, Z is the atomic number, E is the

incident energy and C_2 is another constant at the given energy E (McCullough 1975). Thus the ratio of the total atomic cross sections for coherent and Compton scattering can be approximated by dividing equation (1.18) by equation (1.19) to give:

$$\sigma_R/\sigma_C \simeq C_3 Z^{(n-1)} \qquad (1.20)$$

where C_3 is constant for a given energy. The $Z^{(n-1)}$ power dependence of the ratio of differential cross sections is not obvious from equation 1.17. However, it is implicit in the values of form factors and incoherent scattering functions tabulated by Hubbell et al., (1975). The exponent varies with scattering angle (Roy and Reed, 1968). The change in the exponent, n, as a function of scattering angle is related to the fact that at larger angles the momentum transfer parameter is higher during the scattering process, thus inner electrons with higher binding energies contribute to the process (Kissel and Pratt, 1978), while at small scattering angles only the outer electrons participate in the scattering process.

Conversion of the coherent-Compton ratio, R, to the bone mineral density requires the use of calibration phantoms. The accuracy of the technique has been determined to be 5% (Shukla et al., 1985) and the in vitro precision to be 3%. The latter was measured using a calibration phantom

intermittently over a ten-month period (Shukla et al., 1985). These evaluations of the method were performed for a system which allowed the determination of the bone mineral density of the calcaneus.

The coherent-Compton ratio technique has several advantages from a clinical point of view. Firstly it can be used to measure the density of cancellous bone where mineral changes appear sooner than in cortical bone in different metabolic diseases. Secondly, since the coherent-Compton scattering ratio is measured, slight movements of the measured bone are permissible. It is also possible to make measurements in the proximal femur and comparisons can be made between the central and peripheral bone mineral density values determined by the same method.

1.9 The Coherent Scattering Technique

In this technique coherent scattering alone is to be used for bone mineral density determination. If one considers coherent scattering alone, the partial linear attenuation coefficient will, to a first approximation, depend on the product of density, ρ, and Z^n. When the concentration of mineral in bone is reduced, both the density and the effective atomic number fall. It is therefore evident that a technique based on coherent scattering alone must be more sensitive to changes in

mineral status than either the Compton or the coherent-Compton scattering ratio method. The use of coherent scattering alone has been suggested by Kerr et al. (1980) and Mossop et al. (1987). In this thesis the technique's basis in physics is reviewed and investigated further, the possibility of developing a clinical system is explored and the first in vitro bone mineral measurements using coherent scattering alone, are reported.

1.10 Conclusions

All methods discussed have certain advantages and disadvantages. The most clinically accepted are probably DPA and CT since they allow studies of fracture-prone sites. One physical measurement which has not been made and which should reflect bone strength more reliably than current procedures is to assess the mass of mineral per unit volume of trabecular bone. Hence this work assesses the possibility of developing a system for this measurement and of assessing its potential as a clinical device.

CHAPTER 2

ASPECTS OF GAMMA RAY INTERACTIONS

2.1 Introduction

The interactions of electromagnetic radiations or photons with matter can be classified into either scattering or absorption processes. In the latter case the photon disappears, losing all its energy to the medium and in the former case the photon is deflected with or without significant loss of energy. The scattering process can be subdivided further into elastic, and inelastic scattering. Elastic scattering is the phenomenon in which the photon is scattered without imparting internal energy to the atom or molecule. Elastic scattering from atoms is called Rayleigh or coherent scattering when strongly bound atomic electrons are involved, and Thomson scattering when atomic electrons can be regarded as free, in the low energy limit. In the inelastic scattering process, the gamma ray photon emerges with reduced energy, the difference going into raising the internal energy of the atomic system either by ejecting one of the electrons or by elevating (exciting) them to higher energy states.

While the process of concern in this thesis is elastic (coherent) scattering, brief mention will be made of

absorption processes.

2.2 Elastic (coherent) Scattering

In the elastic scattering process, the whole atom receives the recoil energy. Each electron oscillates in phase. The coherent combination of radiation emitted from each electron forms the scattered photon which has virtually the same energy but a different direction from that of the incident photon. Elastic scattering from atoms is made up of contributions from Rayleigh scattering, Delbruck scattering, resonance scattering and nuclear Thomson scattering. Rayleigh scattering is the contribution made to elastic scattering by the atomic electrons. It is therefore an atomic process. The atom is neither excited nor ionised. The scattering from different parts of the atomic charge distribution is therefore coherent. Rayleigh scattering is to be distinguished from elastic scattering by the nucleus. The latter includes: (i) Nuclear Resonant Scattering which occurs when the incident photon energy falls exactly into one of the energy levels of the scattering nucleus; (ii) Nuclear Thomson Scattering which is the classical scattering process in which the incident electromagnetic radiation is scattered by the nucleus considered as a point charge. Its scattering cross-section is given by the usual electron Thomson scattering equations (Section 2.3) with the nuclear

mass replacing the electron mass, and (iii) Delbruck Scattering which is a phenomenon of scattering of photons by a Coulombic field. First predicted by Delbruck on the basis of the theory of quantum electrodynamics, in this process real or virtual electron-positron pairs are produced by a photon in the nuclear electric field. The pairs then annihilate yielding a single photon without energy modification (Delbruck 1933). It is basically a radiative correction to Nuclear Thomson Scattering and is a non-classical, non linear interaction of the electromagnetic fields.

For the small momentum transfer values, $x < 10$ $\mathring{A}^{-1}$, relevant to this work, Rayleigh scattering is the significant contributor, Delbruck and nuclear Thomson have amplitudes comparable to Rayleigh scattering only for large momentum transfer values. The differential scattering cross-sections for small angle scattering of high energy photons and for large angle scattering of low energy photons are approximately equivalent for a given momentum transfer since the latter is a function of photon energy and scattering angle.

In the next two sections the classical treatment of coherent scattering with free electrons (Thomson) will be considered. This will be followed by the modifications

necessary to explain coherent scattering from bound electrons (Rayleigh).

2.3 Thomson Scattering

According to the classical theory of the mechanism of interaction between electromagnetic radiation and free electrons, each electron responds to the force produced on it by the electric vector of the electromagnetic wave. The result is that the electron oscillates with the same frequency as that of the incident radiation. It emits scattered radiation of the same energy and the process is called Thomson (and is coherent) scattering. The application of this model is restricted to an energy region where three conditions must be satisfied for the model to be realistic. One of these conditions is that the atomic number, Z, of the irradiated material must be small so that the electrons are relatively free. Secondly, in order that the interaction is with the electron rather than with the atom as a whole, the wavelength of the incident radiation must be shorter than the characteristic size of the atom ($\sim 10^{-10}$ m). This means that the energy must be greater than 10 keV. Thirdly, this energy must still be small compared to the electron rest mass energy (511 keV) to obviate the need to consider the relativistic effects. Therefore the model is restricted to a narrow energy band. The model is

due to Thomson, who in 1929, theoretically evaluated the cross-section for scattering electromagnetic radiation from a free electron. Forces due to the electric field of the electromagnetic wave produce an acceleration of magnitude eE/m on the electron, E being the electric field due to the gamma rays and e and m being the charge and the mass of the electron respectively. Since the electric field is periodic the electron acceleration will be periodic. The accelerating electron will then radiate electromagnetic waves of the same frequency as the incident waves which constitute the scattered gamma rays.

Thomson has shown that the electric field E, at a distance, r, from an electron oscillating with instantaneous acceleration given by:

$$a = eE/m \tag{2.1}$$

is

$$E = \left(\frac{\mu_o}{\epsilon_o}\right)^{1/2} H \tag{2.2}$$

$$= \frac{ae\sin\theta}{4\pi\epsilon_o rc^2} \tag{2.2a}$$

where θ is the angle between the direction of acceleration and the displacement r, c is the velocity of electromagnetic waves, μ_o is the magnetic permeability of space, H the

magnetic field and ϵ_o is the electrical permittivity of space (or $1/2\pi\epsilon_o$ is the Coulomb law constant). Figure 2.1 illustrates the electromagnetic theory of scattering by a free electron. The electric vector $\vec{E}_i$ of the incident radiation is given by:

$$E_i^2 = E_y^2 + E_z^2 \tag{2.3}$$

Thomson considered that for unpolarised radiation the two components E_y and E_z are equal when averaged over many photons. Equation 2.3 therefore becomes:

$$E_y^2 = E_z^2 = \frac{E_i^2}{2} \tag{2.4}$$

Thomson was able to show that;

$$E_{sxy}^2 + E_{sz}^2 = E_i^2 \frac{1}{(4\pi\epsilon_o)^2}\left(\frac{e^2}{mc^2}\right)^2\left(\frac{1}{r^2}\right)\frac{1+\cos^2\phi}{2} \tag{2.5}$$

and

$$E_{sz}^2 = E_z^2 \quad \frac{1}{(4\pi\epsilon_o)^2}\left(\frac{e^2}{mc^2}\right)^2\frac{1}{r^2} \tag{2.6}$$

where E_{sxy} is the electric vector of the scattered wave which is polarised with its electric vector in the xy plane and E_{sz} is the scattered component due to the motion of the electron in the z direction and r is the distance from the

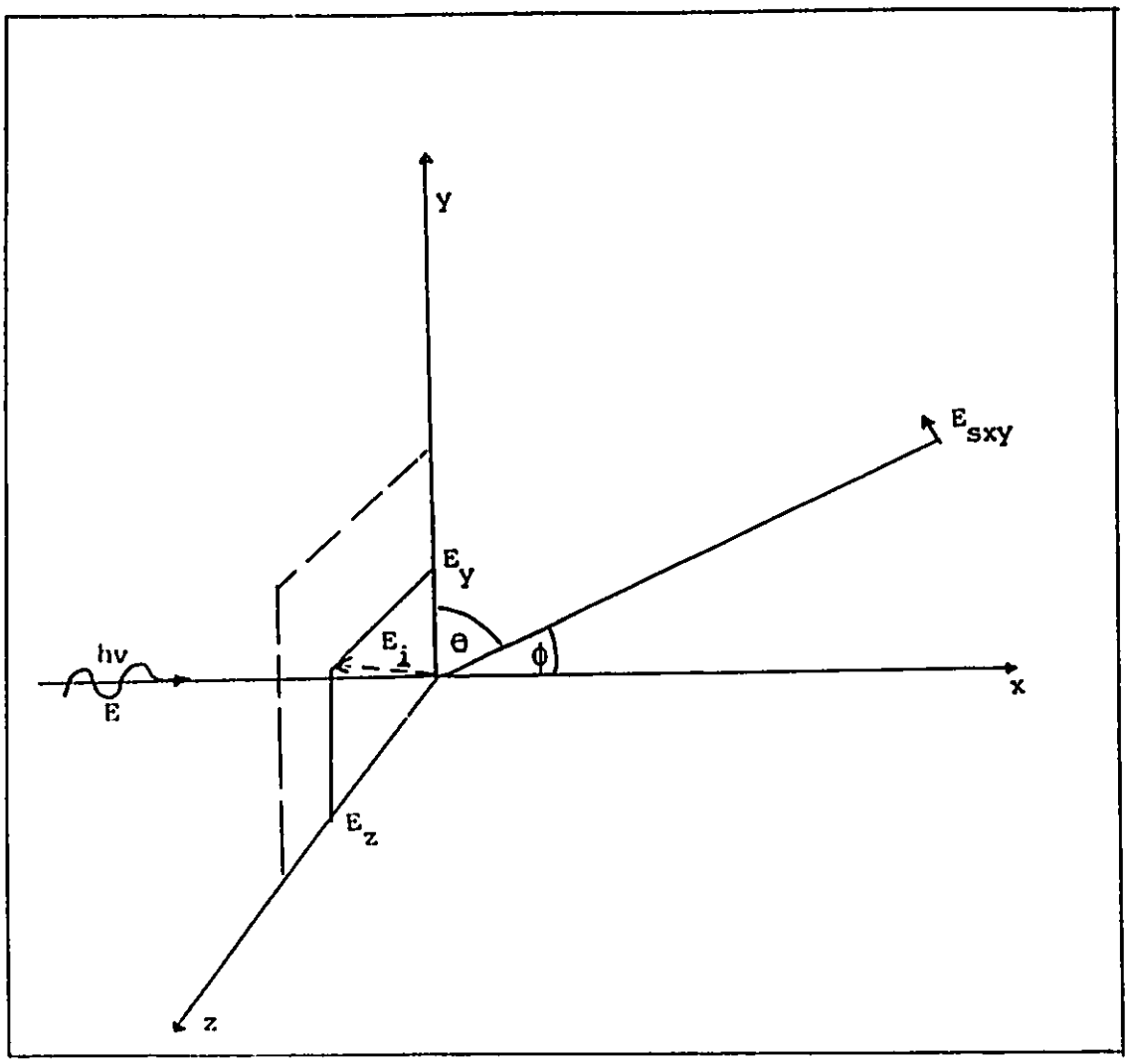

Figure 2.1 Scattering of electromagnetic radiation by a free electron.

accelerated electron to the electric field. θ is the scattering angle and is equal to $(\pi/2-\phi)$, with ϕ being the angle between the direction of acceleration of the electron and the direction of observation.

Since the intensity of electromagnetic waves is proportional to the square of the electric field intensities, the ratio of the intensities of the incident and scattered waves is given by:

$$\frac{I_s}{I_i} = \frac{1}{(4\pi\epsilon_o)^2}\left(\frac{e^2}{mc^2}\right)^2\left(\frac{1}{r^2}\right)\frac{1+\cos^2\theta}{2} \qquad (2.7)$$

It is often useful to define a differential cross-section, $d\sigma/d\Omega$, which expresses the emission or detection probability of electromagnetic radiation in a given direction, $\sigma(\theta)$. That is

$$\sigma(\theta) = \frac{d\sigma}{d\Omega} \qquad (2.8)$$

and $\sigma(\theta)$ represents the cross-section for radiation to be detected or emitted into an element of solid angle, $d\Omega$, lying at a mean angle θ to the incident direction (figure 2.2). $\sigma(\theta)$ will have units of cm^2/steradian. The total cross-section is the integral of the differential cross-section over all space, that is:

$$\sigma = \int_{\phi=0}^{2\pi} \int_{\theta=0}^{\pi} \sigma(\theta) \sin\theta d\theta d\phi$$
$$= 2\pi \int_{0}^{\pi} \sigma(\theta) \sin\theta d\theta \qquad (2.9)$$

Figure 2.2 is a diagram to illustrate the formula:

$$d\Omega = 2\pi \sin\theta d\theta \qquad (2.10)$$

where $d\Omega$ is the solid angle between two emergent cones of semi angle θ and $\theta+d\theta$ respectively and with a common apex.

The differential Thomson scattering cross-section is given by:

$$d\sigma_T = \frac{1}{(4\pi\epsilon_o)^2} \left(\frac{e^2}{mc^2}\right)^2 \frac{1+\cos^2\theta}{2} d\Omega \qquad (2.11)$$

The total scattered intensity integrated over all angles is therefore given by:

$$I_s = I_i \frac{1}{(4\pi\epsilon_o)^2} \left(\frac{e^2}{mc^2}\right)^2 \int_0^{\pi} \frac{(1+\cos^2\theta)}{2} 2\pi \sin\theta d\theta \qquad (2.12)$$

$$= I_i \frac{1}{(4\pi\epsilon_o)^2} \frac{8\pi}{3} \left(\frac{e^2}{mc^2}\right)^2$$

$$= I_i \frac{8\pi}{3} r_e^2 \qquad (2.13)$$

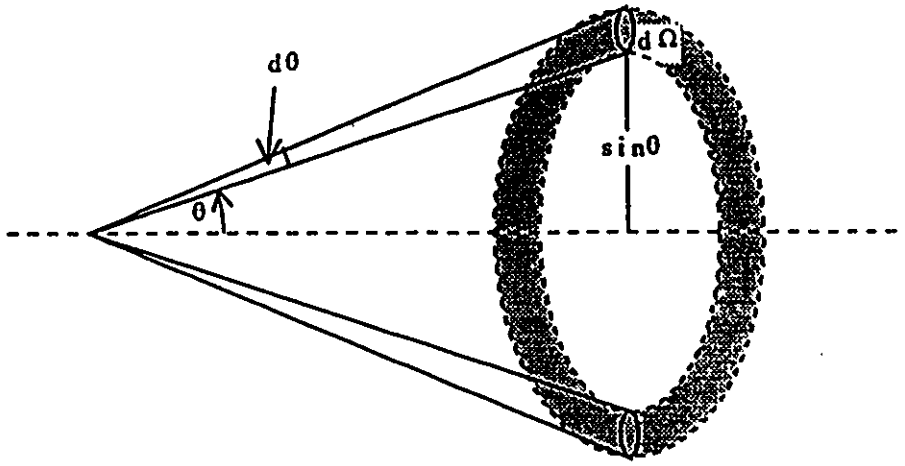

Figure 2.2 Illustration of the solid angle $d\Omega$ given by $d\Omega = 2\pi \sin\theta d\theta$

where r_e is the classical electron radius and is given by the expression:

$$r_e = \frac{\mu_o e^2}{4\pi m} \tag{2.14}$$

The cross-section per electron σ_T, for Thomson scattering of unpolarised radiation is given by:

$$\sigma_T = \frac{8\pi}{3} r_e^2 \tag{2.15}$$

Thomson also derived an expression for the differential cross-section, $(d\sigma_T(\theta))/(d\Omega)$, which is the fraction of the intensity scattered by the electron into a unit solid angle and showed that it varied with scattering angle according to the relation:

$$\frac{d\sigma_T(\theta)}{d\Omega} = r_e^2 \frac{(1+\cos^2\theta)}{2} \tag{2.16}$$

2.4 Rayleigh Scattering

For an incident photon momentum $\hbar\underline{k}_i$ and scattered photon momentum $\hbar\underline{k}_f$, an associated momentum transfer can be written as:

$$\frac{\underline{q}}{\hbar} = \underline{k}_i - \underline{k}_f \tag{2.17}$$

The momentum transfer q has units of mc. For elastic scattering one can write:

$$|k_i| = |k_f| = \frac{E}{\hbar c} \tag{2.18}$$

so that $$\hbar q = 2 \frac{E}{mc^2} (mc) \sin \frac{\theta}{2} \tag{2.19}$$

where E is the incident photon energy, $\hbar$ is the Dirac constant and θ is the scattering angle. Sometimes the momentum transfer is designated as x, in units of inverse Angstrom ($\mathring{A}^{-1}$) and is written as:

$$x = \frac{1}{\lambda} \sin \frac{\theta}{2} \tag{2.20}$$

where λ is the incident photon wavelength in Angstroms. Conversion of q-arguments to x arguments is achieved by multiplying by the factor 20.60744. In other words:

$$x(\mathring{A}^{-1}) = 20.60744\ \hbar q \text{ (in units of mc)} \tag{2.21}$$

Rayleigh scattering is the only significant contributor in the case of small momentum transfers ($q<0.5mc$ or $x < 10\ \mathring{A}^{-1}$). For larger transfers, nuclear Thomson and Delbruck scattering processes have amplitudes comparable to

the Rayleigh scattering process and must be taken into account.

Bound electrons oscillate in phase when the wavelength of the radiation incident upon an atom is comparable to or larger than the size of the atom. The scattered radiation emitted by each bound electron is also in phase and the phenomenon is called Rayleigh Scattering. In this process the electrons in an atom can be perceived to act as a single particle of charge Ze and mass Zm. In Rayleigh scattering the electrons are all forced into vibration at the frequency of the incident radiation. If this frequency is much greater than the natural frequency of the atomic electrons, the scattered radiation from all the electrons will be in anti-phase with the incident radiation. The scattered contributions will be coherent with each other and their amplitude must be added before squaring to give the scattered intensity. Since the scattering cross section per electron does not make much sense under these circumstances, it is convenient to use an atomic scattering cross-section given by:

$$\sigma_R = \frac{8\pi r_e^2}{3} F^2(x,Z) \qquad (2.22)$$

where $F(x,Z)$ is the atomic scattering form factor and is a function of scattering angle, θ, momentum transfer, x and

atomic number Z of the scatterer. The angle θ is implicit in the definition of the momentum transfer parameter.

For scattering in the forward direction, interference between scattered contributions is constructive and the amplitudes of the radiation scattered from each electron add. Thus the intensity of the scattered radiation from the atom and the atomic cross-section for Rayleigh scattering will both be a factor Z^2 greater than those for a single electron. As the scattering angle increases, the interference between scattered contributions becomes destructive and the differential cross section will be strongly peaked in the forward direction. This forward peaking increases with photon energy because a reduction in the wavelength, λ, implies greater phase difference between contributions scattered from different parts of the atom's electron cloud. Again, as the atomic number increases, the forward peaking reduces because the charge distribution becomes more dense.

Rayleigh scattering has been analysed by Franz (1935) and Moon (1950). A fraction, f_s, of the scattering occurs within an angle ϕ, called the characteristic angle.

$$f_s = \frac{0.6}{(0.8 - \lambda 8 a_T)} \qquad (2.23)$$

where a_T is the effective atomic radius according to the

Thomas-Fermi statistical model. The characteristic angle is given by the relation:

$$\phi = 2\sin^{-1}(\lambda/2a_T) \tag{2.24}$$

Equation 2.24 is valid for $\lambda < 2a_T$. In the Thomas-Fermi model

$$a_T = a_H Z^{-1/3} \tag{2.25}$$

where a_H, the Bohr radius, is given by:

$$a_H = 0.885 \frac{\hbar^2}{mc^2} \tag{2.26}$$

Franz (1935), showed that more than 75% of the Rayleigh scattering is included within the critical angle, ϕ_c, given by:

$$\phi_c = 2\sin^{-1}[(\pi/0.885)(e^2/\hbar c) Z^{1/3} \frac{mc^2}{E}] \tag{2.27}$$

When the angle of scatter is greater than the critical angle the cross section per unit solid angle $d\sigma_R/d\Omega$, is given by the expression:

$$\frac{d\sigma_R}{d\Omega} = \frac{e^4 Z^2 \pi}{(mc^2)^2 2k^3} \frac{1+\cos^2\theta}{2} \tag{2.28}$$

where $$k = 2.46\times10^{-2}\ Z^{1/3}\ \frac{E}{mc^2}\ \sin(\theta/2) \qquad (2.29)$$

Moon (1950) presents equation 2.28 as:

$$\frac{d\sigma_R}{d\Omega} = \frac{8.67 \times 10^{-33}}{\sin^3(\theta/2)} \left(\frac{Zmc^2}{E}\right)^3 \frac{1+\cos^2\theta}{2} \qquad (2.30)$$

Thomson proposed the scattering cross section formula that gives the low frequency limit for elastic photon scattering by isolated charged particles. In order to correct the Thomson formula for scattering by a charge distribution rather than a point charge, the Form Factor Approximation (section 2.4.1) was derived classically. It is used extensively to predict Rayleigh scattering amplitudes in the x and gamma ray region. It is accurate in estimating Rayleigh scattering amplitudes for light atoms for energies well above the K-shell binding and for momentum transfers small compared with $mc(\sim 20\ \text{Å}^{-1})$.

If, as in this work, the atom is regarded as being composed of 'n' atomic electrons distributed throughout the bulk of the atomic volume and a nucleus of charge Z containing the bulk of the atom's mass the nucleus appears as a point charge for an energy region about 100 keV. This energy is sufficiently high so that contributions from

electron-electron correlation and outer electron wave functions are small. The important atomic features are then described as independent electrons interacting electrostatically with a single screened central potential resulting from the charge distribution of the nucleus and all the atomic electrons. Elastic scattering of the photon by an atom is viewed as scattering by bound atomic contents, which remain bound. Since the energy of the scattered photon is almost the same as that of the incident photon, it is not possible to distinguish between the contributions of each component to the scattering. Thus the scattering amplitudes must be summed and then squared to obtain a scattering cross-section.

2.4.1 The Form Factor Approximation

The Form Factor Approximation for Rayleigh scattering is important for two reasons. First, it ties in with classical ideas, having been first derived to correct the classical Thomson scattering formula when the scattering is due to charge distribution rather than a free source (James, 1962). Second, the Form Factor Approximation is relatively easy to calculate. It requires the evaluation of a radial integral over the atomic charge density. Within the framework of classical physics, the differential Rayleigh scattering cross section, $d\sigma_R/d\Omega$, for unpolarised states is

given in the form factor approximation as:

$$\frac{d\sigma_R}{d\Omega} = r_e^2 \frac{(1+\cos^2\theta)}{2}[F(q)]^2 \qquad (2.31)$$

where q is the momentum transfer as described by equation 2.17 and $F(q)$ is the atomic form factor given by the expression:

$$F(q) = \langle \mu_o | \Sigma_{j=1}^{Z} \exp(i\underline{q} \cdot \underline{r}_j) | \mu_o \rangle$$
$$= \int \rho(\underline{r}) \exp(i\underline{q} \cdot \underline{r}) \, d\underline{r} \qquad (2.32)$$

where $|\mu_o\rangle$ is the ground state of the atom, $\underline{r}_j$ is the radius vector of the jth electron and $\rho(\underline{r})$ is the electronic charge density at $\underline{r}$. $\rho(\underline{r})$ is given by the expression:

$$\rho(\underline{r}) = \Sigma_{j=1}^{Z} \rho_j(r) = \Sigma_{j=1}^{Z} \psi_j^*(r) \, \psi_j(r) \qquad (2.33)$$

where $\rho_j(r)$ is the charge distribution of the jth electron and $\psi_j(r)$ is its wave function. This arises from the extensive computations of wave functions of many-electron atoms based on the self-consistent field method of Hartree (1928a, 1928b). It is an independent particle model in which each electron is assumed to be in the field of the nucleus and in an average field due to the other electrons.

The Hartree scheme was generalised by Fock (1930,

1934) to include effects of exchange. Slater (1951) has shown that the Hartree and the Hartree-Fock wave functions arise out of vibrational treatments in which the wave function of the many-electron atom is assumed to be the product of individual electron wave functions. For the spherically symmetric distribution, F(q) simplifies to:

$$F(q) = 4\pi\int_0 \rho(r,Z)r^2 \sin\frac{krdr}{kr} \qquad (2.34)$$

or in terms of the x-argument

$$F(x,Z) = 4\pi\int_0 \rho(r,Z)r^2 \sin\frac{(4\pi xr)dr}{4\pi xr} \qquad (2.35)$$

where $\rho(r)$ or $\rho(r,Z)$ is now the charge density at a distance r from the centre of symmetry, Z is the atomic number and k is $q/\hbar$.

Hartree (1925), Debye (1930) and Compton (1930) showed that the classical and non-relativistic quantum mechanical derivation of the form factor approximation requires the energy of the incident photon to be large compared to the binding energy of the scattering electron and the electron's velocity must be small compared to the speed of light.

In his derivation of the relativistic Rayleigh scattering cross section using second order perturbation

theory, Franz (1935, 1936) showed that the non-relativistic form factor could be derived by assuming the intermediate states to be free. Berke (1952) drew the same conclusion when he used Feynman's method to derive the form factor approximation. The form factor approximation is valid for $q<mc$ as was demonstrated by Goldberger and Low (1968) and Florescu and Gavrila (1976). Kissel et al. (1980) have also shown that the form factor does not become increasingly valid with increasing energy but that an error of the order of $Z\alpha^2$ remains at all photon energies; α being the fine structure constant.

For elements of $Z<100$ and for $2<X<6.0\text{Å}^{-1}$ which are relevant to work in this thesis, the F(x,Z) values tabulated by Hubbell and Overbo (1979), were used. They are based on the Hartree Independent Particle Model. This means that the electron-correlation effects have been neglected. Tseng et al. (1973) have demonstrated that the form factor F(x,Z) values are rather insensitive to electron-correlation effects, Weiss (1966) also estimates the errors in F(x,Z) due to the neglect of electron correlations to be of the order of 1%.

The form factor falls with increasing energy because the probability of momentum transfer without energy absorption decreases as the incident photon energy rises. The form factor also decreases as the scattering angle

increases because of destructive interference. Since momentum transfer encapsulates both energy and scattering angle it is expected, as demonstrated in figure 2.3 that the form factor will decrease rapidly with increasing momentum transfer.

From equations 2.6 and 2.31 the differential cross section per atom for Rayleigh scattering, can be written as:

$$\frac{d\sigma_R(\theta)}{d\Omega} = \frac{d\sigma_T}{d\Omega}[F(x,Z)]^2 \qquad (2.36)$$

$$= \frac{r_e^2}{2}(1+\cos^2\theta)[F(x,Z)]^2 = \sigma_R(\theta)$$

Figure 2.4 illustrates the theoretical variation of $\sigma_R(\theta)$ with photon energy and scattering angle, θ, for an element of Z=9.

Based on the various models of charge distribution mentioned above, values of F(x,Z) have been derived theoretically and have been compared with experimental observations (Hubbell et al. 1975, 1979 and Cromer 1968). For the ranges of momentum transfer up to 10 Å^{-1} and atomic numbers up to Z=18, relevant to this work, there is good agreement between theory and experiment.

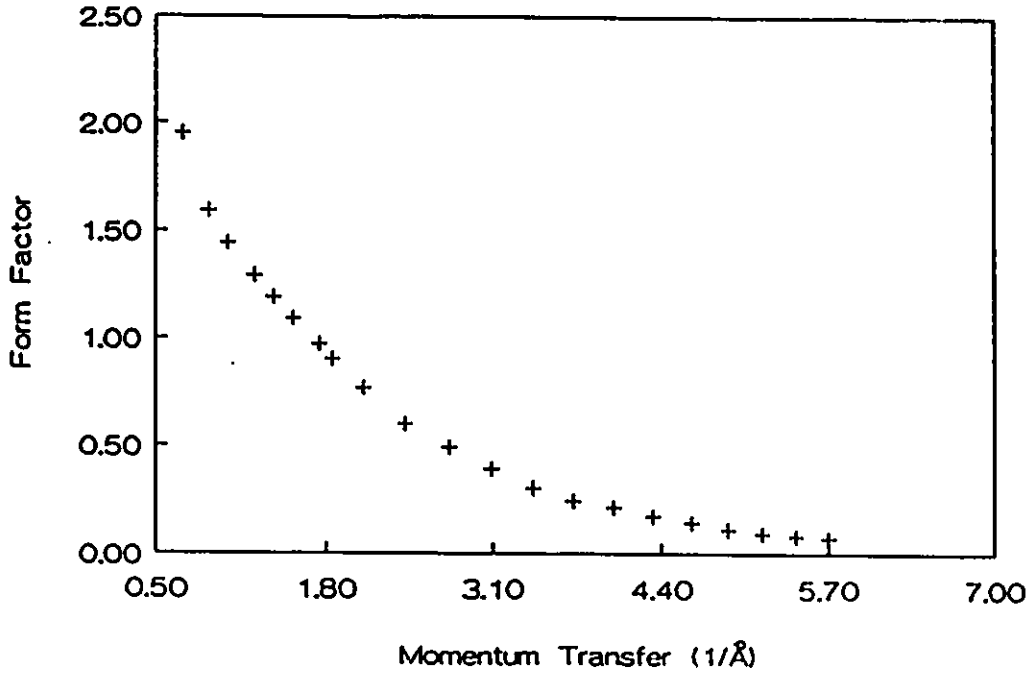

Figure 2.3 The form-factor as a function of momentum transfer.

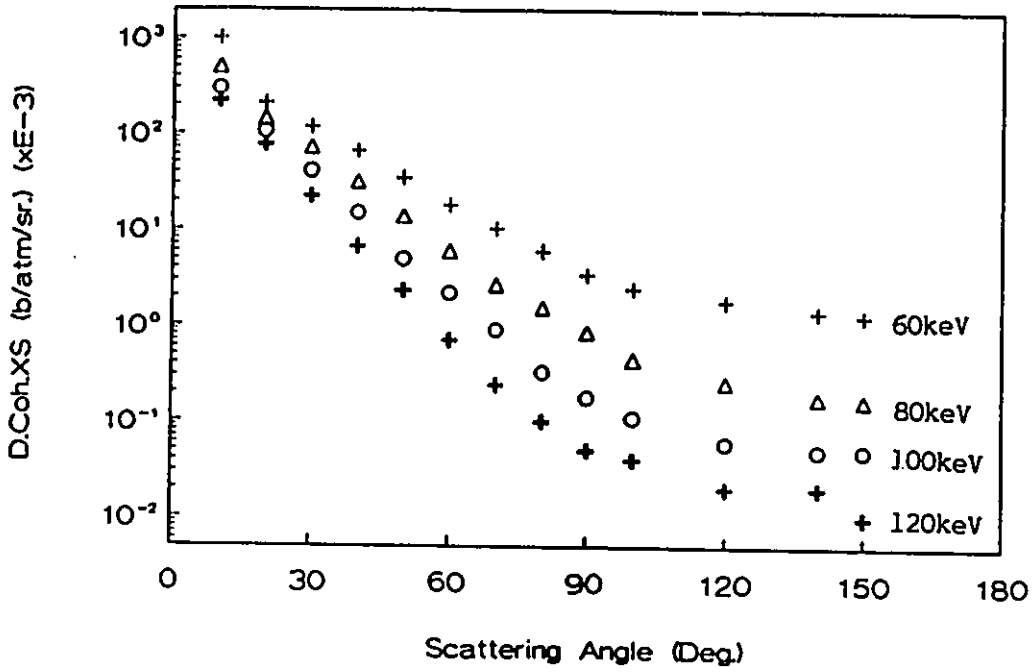

Figure 2.4 The variation of differential cross section with scattering angle for an element of atomic number 9,at various incident photon energies.

2.5 Inelastic Scattering

Inelastic or incoherent scattering can be subdivided into two categories. The first of these is scattering from free or relatively free electrons and is called Compton scattering. The second is from bound electrons and is important at photon energies below electron binding energies.

2.5.1 Compton Scattering

This type of incoherent scattering occurs when the momentum transferred to the electron by the incident photon is very much greater than the momentum of the electron when bound to the atom. The electron recoils with respect to the others, the internal energy of the atomic system is increased and the incident photon energy is correspondingly depleted. The effects of these inelastic photon interactions with different parts of the atomic system combine incoherently, that is, by addition of the intensities of the effects.

For gamma rays of energy greater than about 10% of the electron rest-mass energy, the interaction can be regarded as a collision between an electron and a photon. The electron must recoil from the collision. The scattered photon emerges from the collision less energetic than the incident photon. The difference in the energy appears as

the kinetic energy of the electron. Compton (1929) provided the theoretical explanation for the process. His equation, derived from considerations of the principles of conservation of energy and momentum is:

$$E' = \frac{E}{1+\frac{E}{mc^2}(1-\cos\theta)} = h\nu' = \frac{h\nu}{1+\alpha(1-\cos\theta)} \qquad (2.37)$$

where E' is equal to $h\nu'$ and is the energy of the emergent (scattered) photon, E is equal to $h\nu$ and is the incident photon energy, θ is the scattering angle, m the electron rest mass, c is the speed of light, ν' and ν are the frequencies of the scattered and incident photons respectively and α is equal to $h\nu/mc^2 = E/mc^2$. From equation 2.37, it is clear that mono-energetic photons scattered through a fixed angle will emerge mono-energetic (though with a lower energy). The number of photons scattered through angle θ varies with energy. The probability of scattering through a given angle, differential incoherent cross-section, was derived by Klein and Nishina (1929) when they analysed Compton scattering quantum-mechanically.

If one considers plane polarised radiation and analyses only the cases where the scattering plane also contains the electric vector of the incident radiation,

figure 2.1, the differential collision cross section for Compton scattering is given by Davisson and Evans (1952) and Dyson (1973) as:

$$d\sigma_c = \frac{r_e^2}{2} d\Omega\left(\frac{\nu}{\nu'} + \frac{\nu'}{\nu} - \sin^2\theta\right) \qquad (2.38)$$

where r_e is the classical electron radius. The incident and scattered frequencies are related by the equation:

$$\frac{1}{h\nu'} - \frac{1}{h\nu} = \frac{1}{mc^2}(1-\cos\theta) \qquad (2.39)$$

where ν' approaches ν, equation 2.38 shows that $d\sigma_c$ approaches $r_e^2 d\Omega(1-\cos^2\theta)$, which is the angular distribution for Thomson scattering of plane polarised radiation. From equation 2.39 the ratio of scattered to incident radiation frequencies can be determined as:

$$\frac{\nu'}{\nu} = \frac{1}{1+\frac{h\nu}{mc^2}(1-\cos\theta)} = \frac{1}{1+\alpha(1-\cos\theta)} \qquad (2.40)$$

An increase in E (hence in α) or in θ, causes a greater frequency shift and the differential cross section falls below the Thomson value. Thus the angular distribution becomes more peaked in the forward direction. Equation 2.38

has been expressed in a more complete form by Davisson and Evans (1952) as:

$$d\sigma_c = \frac{r_e^2}{2} d\Omega \left(\frac{\nu'}{\nu}\right)^2 \left(\frac{\nu}{\nu'} + \frac{\nu'}{\nu} - \sin^2\theta\cos^2\epsilon \right) \qquad (2.41)$$

where ϵ is the angle between the plane defined by the direction of incidence and the direction of the electric vector of the incident radiation and the scattering plane. For unpolarised radiation the requirement that $\cos^2\epsilon$ is 1/2 leads to equation 2.38.

The intensity scattered at an angle θ into angle $d\Omega$ is given by equation 2.38 multiplied by a further factor, (ν'/ν), (Dyson 1973). To obtain the total collision cross section, equation 2.38 requires integration over all scattering angles giving the expression:

$$\sigma_c = 2\pi r_e^2 \left[\frac{1+\alpha}{\alpha^3} \left\{ \frac{2\alpha(1+\alpha)}{(1+2\alpha)} - \ell n(1+2\alpha) \right\} + \frac{\ell n(1+2\alpha)}{2\alpha} - \frac{(1+3\alpha)}{(1+2\alpha)^2} \right] \qquad (2.42)$$

when $\alpha << 1$ equation 2.42 can be reduced to:

$$\sigma_c = \frac{8\pi}{3} r_e^2 \left(1 - 2\alpha + 5.2\alpha^2 - 13.3\alpha^2 + 32.7\alpha^4 \ldots\right) \qquad (2.43)$$

At low frequencies, the cross section per electron is given approximately by:

$$\sigma_c = \frac{8\pi}{3} r_e^2 (1-2\alpha) \qquad (2.44)$$

Compton scattering is a process in which all atomic electrons act independently. However, below a certain photon energy an atomic electron can no longer be considered free and its contribution to Compton scattering diminishes. The atomic cross section for this process is therefore equal to the product of the atomic number, Z times the Klein-Nishina cross section diminished at low photon energies, by the effect of atomic binding. The Klein-Nishina cross section approaches the Thomson cross section as the gamma photon energy approaches zero. Solutions to the Klein-Nishina equation have been tabulated by many workers, for example O'Kelley and Sweeney (1954).

2.5.2 Inelastic (Incoherent) Scattering from Bound Electrons

Incoherent scattering can occur from a bound electron which can either leave the atom or rise to an excited state within the atom. The cross-section is given by the product of the Klein-Nishina cross section for a free electron and the Incoherent scattering Factor, S(q) or S(x,Z), also called the incoherent scattering function. It is related to the probability that an electron absorbs energy and either leaves the atom or remains within the atom in a higher or excited state. The incoherent scattering factor can be expressed, in terms of the scattering form factor of

equation 2.32, generalised to include excited states (Grodstein 1957, Brown, 1966, Veigele 1967) as follows:

$$F_\epsilon(\vec{q},Z) = \langle \psi_\epsilon \mid \sum_{j=1}^{Z} \exp(i\vec{q} \cdot \vec{r}_j) \mid \psi_0 \rangle \qquad (2.45)$$

where ψ_ϵ now indicates the wave function of an excited or ionised stationary state as compared with the wave function ψ_0 of the ground state. The incoherent scattering factor can therefore be written as:

$$S(q,Z) = \sum_{\epsilon>0} |F_\epsilon(q,Z)|^2 \qquad (2.46)$$

The summation is over discrete states and an integral would be over continuous states, without including the ground state for which $\epsilon=0$. In order to remove the summation over excited states, Brown (1966) has rewritten equation 2.46 as:

$$\begin{aligned} S(q,Z) = \sum_{\epsilon=0} & \langle 0 \mid \sum_m \exp(-i\vec{q} \cdot \vec{r}_n) \mid \epsilon \rangle \\ & \langle \epsilon \mid \sum_m \exp(i\vec{q} \cdot \vec{r}_m) \mid 0 \rangle \\ & - |\langle 0 \mid \sum_j \exp(i\vec{q} \cdot \vec{r}_j) \mid 0 \rangle|^2 \end{aligned} \qquad (2.47)$$

where $\vec{r}_n$, $\vec{r}_m$, $\vec{r}_j$, are the radius vectors from the nucleus to the nth, mth and jth electron respectively. Usage of the closure property (Schiff 1955, Messiah 1965) allows one to

write:

$$\sum_{\epsilon=0} |\epsilon><\epsilon| = 1 \qquad (2.48)$$

The last term in equation 2.47 can be identified with $|F(q,Z)|^2$ so that in terms of the ground state wave functions only, one has the expression:

$$S(\vec{q},Z) = \sum_{m=1}^{Z}\sum_{n=1}^{Z} <\psi_0|\exp[i\vec{q}(\vec{r}_m - \vec{r}_n)]|\psi_0> - |F(\vec{q},Z)|^2$$

$$= S(x,Z) \qquad (2.49)$$

where x is the momentum transfer in units of Å^{-1}.

The differential incoherent scattering cross section per electron $d\sigma_{inc}/d\Omega$, can be expressed as:

$$d\sigma_{inc}/d\Omega = \frac{d\sigma_{KN}}{d\Omega}\left[\frac{S(x,Z)}{Z}\right] \qquad (2.50)$$

where $d\sigma_{KN}/d\Omega$ is the differential Klein-Nishina cross section per electron.

At low photon energy, the recoil momentum is small and the atom remains in the ground state. This means that the scattering is coherent and S(x,Z) is zero. When the recoil momentum is larger than the momentum of the electron in its bound state, the recoiling electron is almost certain to leave the atom and S(x,Z) is close to unity. The

dependence of S(x,Z) on energy means that at all values of S(x,Z) equal to Z, the S(x,Z)/Z is unity and the incoherent scattering cross section is given by the Klein-Nishina equation.

A longer notation for the angular distribution function (or the differential incoherent cross-section) per atom is given by the expression:

$$\frac{d\sigma_{inc}}{d\Omega} = \frac{r_e^2}{2} [1+g(1-\cos\theta)]^{-2} [1+\cos^2\theta + \frac{g^2(1-\cos\theta)^2}{1+g(1-\cos\theta)}] S(x,Z) \frac{cm^2 atom^{-1}}{ster} \quad (2.51)$$

where g is the photon energy in units of mc^2 (ie. electron rest-mass energy). Values of the incoherent scattering factor have been tabulated by Hubbell et al. (1975).

2.6 Photo-electric Effect

The photoelectric effect is a process in which a low energy photon is absorbed by a bound electron in an inner shell of the atom. The electron is ejected from the atom with kinetic energy T, where T is equal to the difference between the incident photon E and the binding energy B, of the electron in the atom. The equation describing the process can be written as:

$$T = E - B \qquad (2.52)$$

Low energy photons can interact this way only with outer electrons for which B is small. As the energy increases, the interactions are more likely to be with tightly bound K-shell electrons. The energy B is emitted promptly by the residual atom in the form of characteristic x-rays and Auger electrons from the filling of the vacancy in the inner shell. Auger electrons are outer electrons which are ejected by the photoelectric absorption of characteristic radiation. The photoelectric effect can take place with an L or M shell electron, the electron replacement could be from any outer shell and the characteristic radiation could completely escape the atom, without producing an Auger electron. The relative probabilities of all these events are calculable. Since the whole atom is involved, the probability for the photoelectric effect is described by an atomic cross section, τ_a (cm^2/atom). According to experimental evidence and various theories of photoelectric interactions (Siegbahn, 1965; Evans, 1955) the probability of the atomic photoelectric effect exhibits a rapid decrease as the energy of the incident photon increases and a rapid increase as the atomic number of the interacting material increases. The theory is complicated by screening effects of outer

electrons and the transition from non-relativistic to relativistic approximations (Grodstein, 1957).

For non-relativistic energies, the angular distribution of photoelectrons per unit solid angle is given by:

$$\frac{dN(\theta)}{d\Omega} = N(\theta) = \frac{\sin^2(\theta)}{(1-\frac{v}{c}\cos\theta)^4} \qquad (2.53)$$

where v is the velocity of the photo-electron. For unpolarised photons the probability distribution is symmetrical about the direction of the photons. The interaction cross section per atom, integrated over all angles of photoelectric emission can be written as:

$$\tau_a = k\frac{Z^n}{E^m} \qquad (2.54)$$

where k is a constant. Both theory and experiment show clearly that the proper exponents for Z and E are each non integral and are each functions of E.

2.7 Pair-production

Near an atomic nucleus (and less frequently near an atomic electron) a photon of energy at least 1.022 MeV, (2.044 MeV near an electron) can disappear with the formation of an electron-positron pair. Most of the

electrons and positrons so produced are confined to directions within mc^2/E radians from the photon direction. The pair production process has an energy threshold of 1.022 MeV in the field of the atomic nucleus and 2.044 MeV in the field of an electron (Attix 1986). Pair production is the predominant interaction mechanism at high atomic number and at high incident photon energies. The atomic cross-section, K_a, for the process, has a threshold at 1.02 MeV and levels off near 50 MeV for high atomic number material, with values that can be as high as 100 barn per atom.

In the region between 1.02 MeV and 50 MeV the cross section per atom varies approximately as the square of the atomic number, that is:

$$K_a \simeq kZ^2 \qquad (2.55)$$

where k is a complicated function of energy and atomic number.

2.8 Attenuation of Electromagnetic Radiation in Matter

All the processes described above contribute to the removal of gamma ray photons from the original photon beam. The probability that a photon will traverse a given thickness of attenuating material without suffering any kind

of interaction is simply the product of the probabilities of survival for each particular type of interaction mechanism. Thus a collimated gamma photon beam of initial intensity I_o, after traversing a thickness x of attenuator will have a residual intensity, I, given by:

$$\begin{aligned} I &= I_o \exp-(\mu_c x + \mu_r x + \mu_k x + \mu_R x) \\ &= I_o e^{-\mu x} \end{aligned} \qquad (2.56)$$

where $$\mu = \mu_c + \mu_r + \mu_k + \mu_R \qquad (2.57)$$

is the total linear attenuation coefficient and μ_c, μ_r, μ_k and μ_R are the partial linear attenuation coefficients for the processes of Compton scattering, photoelectric effect, pair production and Rayleigh scattering respectively. It has units of cm^{-1} or m^{-1}.

For any interaction process, the mass attenuation coefficient is the linear attenuation coefficient divided by the density, ρ(g/cm^3 or Kg/m^3). The mass attenuation coefficients are more fundamental than linear attenuation coefficients in that the former are independent of actual density and physical state of the attenuator. The interactions can be expressed as cross sections per atom, K_a, τ_a, R_a and C_a and when multiplied by the number of atoms per gram, the mass-absorption coefficients are obtained directly. The Compton atomic cross section can also be considered as the product of an electronic cross section and

the atomic number; that is $C_a = C_e Z$. The total mass attenuation coefficient for gamma ray interaction can be written, in units of cm^2/g or m^2/kg, as:

$$\frac{\mu}{\rho} = \frac{\mu_\tau}{\rho} + \frac{\mu_c}{\rho} + \frac{\mu_k}{\rho} + \frac{\mu_R}{\rho} \qquad (2.58)$$

where τ/ρ is the contribution of the photoelectric effect, c/ρ that of the Compton effect, k/ρ that of pair production and σ_R/ρ that of Rayleigh scattering.

For mixtures of elements or chemical compounds, the attenuation of gamma rays is assumed to depend only upon the sum of the cross-sections presented by all the atoms in the mixture. Chemical bonds have no significant effect on the gamma ray interactions as they are of the order of only a few electron volts. Thus for an attenuator of bulk density ρ, made up of a mixture of elements of mass attenuation coefficients μ_1/ρ_1, μ_2/ρ_2 μ_3/ρ_3 etc., its overall mass attenuation coefficient is given by:

$$\frac{\mu}{\rho} = \sum_i \omega_i \frac{\mu_i}{\rho_i} \qquad (2.59)$$

where ω_i is the fraction by weight of the ith element in the attenuator.

2.9 Conclusion

In the energy region of interest to this work, the principal gamma photon interaction mechanism are incoherent scattering, photoelectric effect and Rayleigh scattering. Compton scattering is of the dominant interaction process (in terms of cross-section magnitude) at energies above electron binding energies while Rayleigh scattering is the major interaction for low energies. The photoelectric effect is prominent in the intermediate energy region.

CHAPTER 3

DETECTOR CALIBRATION AND CHOICE OF PHOTON ENERGY

3.1 Introduction

In order to quantitate the number of photons coherently scattered from bone, a detector with high energy resolution is required. A right-cylindrical planar, high purity germanium detector with an active area of 400 mm^2 was available and was characterised with respect to resolution and counting efficiency.

3.2 Semiconductor Detectors

Germanium and silicon detectors are solid state analogues of gas ionisation detectors. Their major advantage compared to other detectors is a high efficiency of conversion of incident photons into electrical impulses. The amount of energy required to produce an ion-pair in a semiconductor is about ten times smaller than in a gas. Solid state materials like germanium are about 5000 times denser than gases, have greater stopping powers and are, as a result, much more efficient detectors of x and gamma rays. The electrical signal (per unit of radiation absorbed) is about ten times larger than in gas-filled detectors and allows detection and counting of individual radiation

events. The amplitude of the electrical signal is proportional to the amount of radiation energy absorbed and therefore semiconductor detectors can be used for energy-selective radiation counting.

Despite these clear advantages, semiconductor detectors have a number of problems. The first is that germanium (and silicon for that matter) conducts a significant amount of thermally induced electrical current at room temperature. This creates a background noise that interferes with detection of radiation-induced currents. Germanium detectors must, therefore, be operated at temperatures well below room temperature (actually at liquid nitrogen temperatures, ~77 K).

Another problem is the presence of impurities (in the form of atoms of other elements) which enter into and disturb the regular arrangement of Ge atoms in the crystal matrix, creating electron traps that capture electrons released in ionisation events. The result is a substantial reduction in the electrical signal available. This problem can be rectified by preparing pure samples of germanium (intrinsic or high purity germanium).

3.3 Detector Energy Calibration and Resolution

The detector used was an Aptec/NRD PhyGe Spectrometer (Model PS401A-B). The manufacturer's specifications are

Table 3.1 Detector Specifications (Manufacturer's)

Parameter	Value/Description
Geometry	planar and right cylinder
Active area	400 mm^2
Active volume	4200 mm^3
Beryllium window thickness	8 mil (=0.2 mm)
Sensitive depth	10.5 mm
Window-to-detector distance	10 mm
Detector diameter, D.	$\sqrt{400 \times 4/\pi}$ mm (= 22.6 mm)

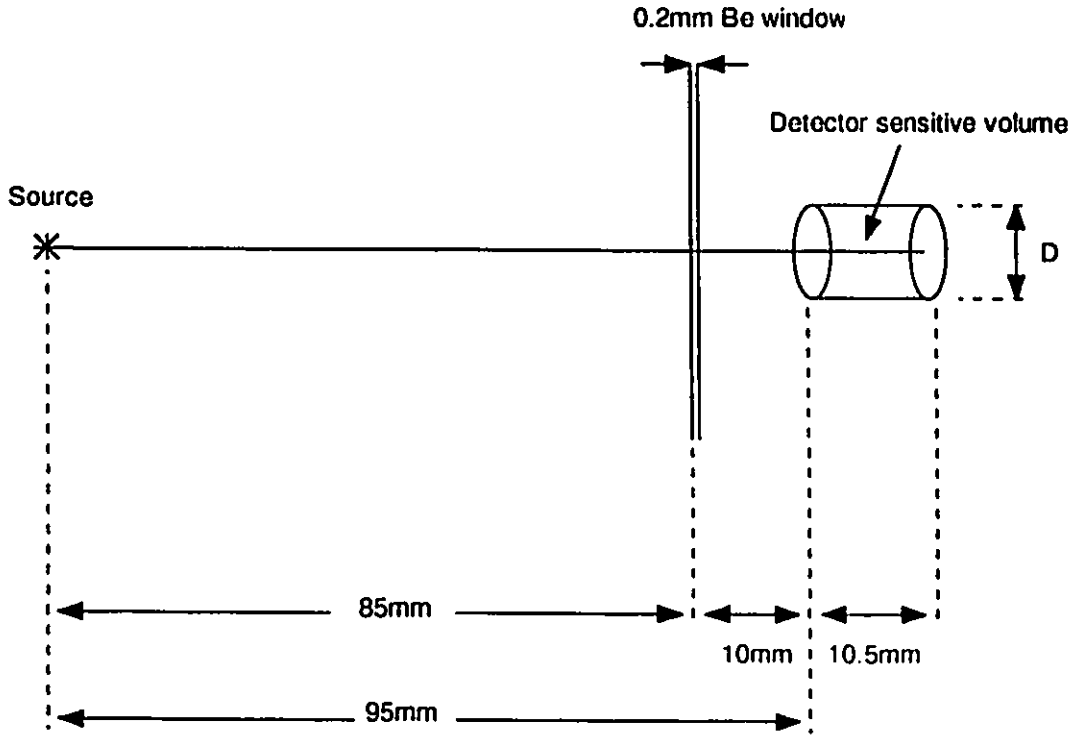

Figure 3.1 Diagram of the measuring geometry

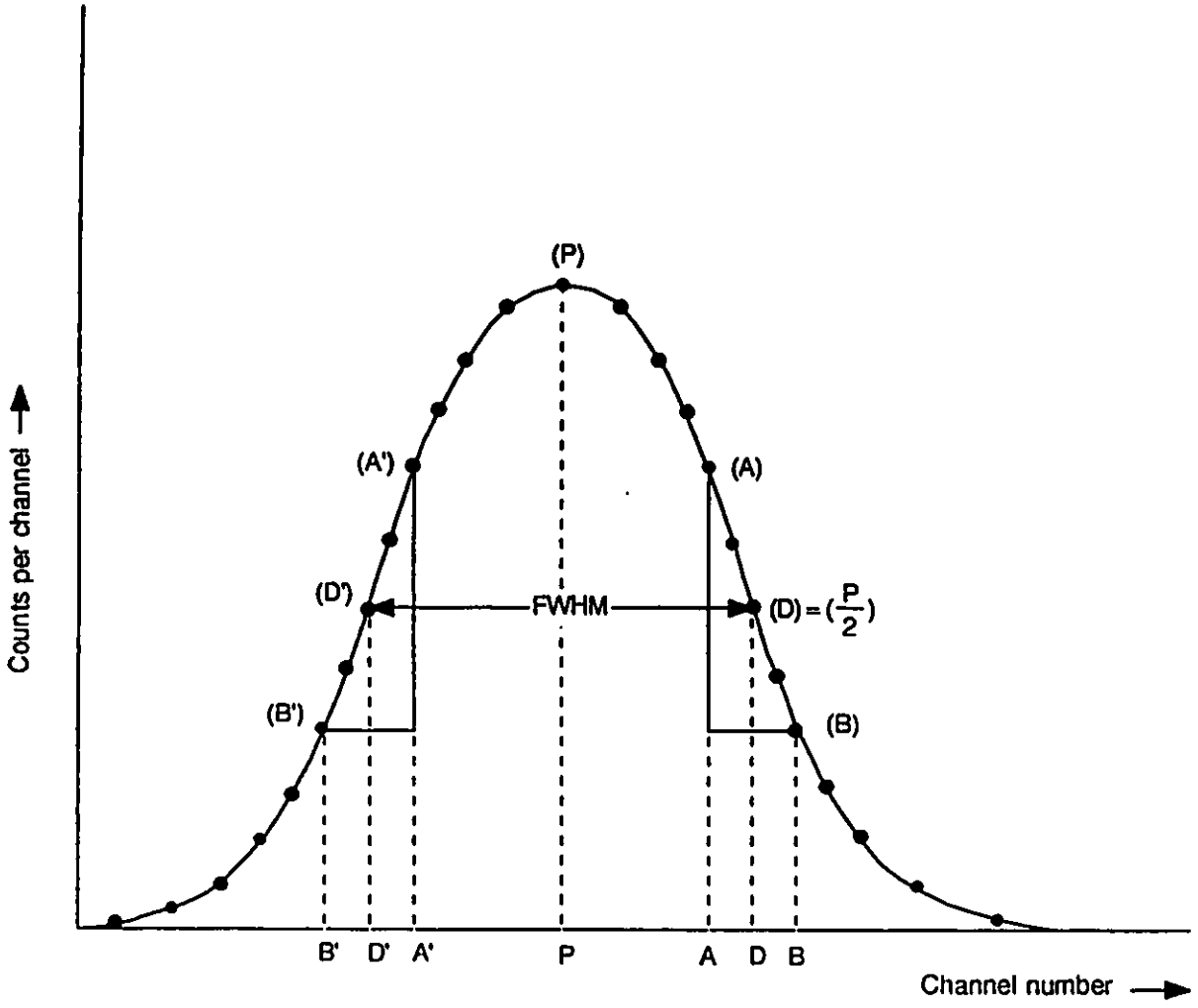

Figure 3.2 Illustrating the determination of Energy Resolution

letters represent the contents of the given channel. Thus (P) is the content or number of counts recorded in channel P.

By definition,

$$FWHM = D-D' = (A-A') + (A'-D') + (D-A) \qquad (3.1)$$

and

$$(D') = (D) = (P/2) \qquad (3.2)$$

From figure 3.2 it can be seen that

$$\frac{(A')-(B')}{A' - B'} = \frac{(A')-(D')}{A' - D'}$$

Therefore,

$$A'-D' = \frac{[(A')-(D')][A'-B']}{(A')-(B')} \qquad (3.3)$$

Similarly,

$$A-D = \frac{[(A)-(D)][A-B]}{(A)-(B)} = |(D-A)| \qquad (3.4)$$

From equations 3.2, 3.3 and 3.4, the necessary values can be substituted in equations 3.1 to yield FWHM.

3.3.2 Results

The results are given in table 3.2. The least squares fit of photon energy of the photopeaks is shown in fig. 3.3. The fitted line has a correlation coefficient of 0.9999. The slope of the line is 0.157 keV per channel.

Table 3.2 Energy Calibration and Resolution for the HPGe Detector

Source	Energy, E (keV)	Photopeak Centroid Channel No.	Energy Resolution	$\frac{FWHM}{E}$ (%)	$E^{-1/2}$
^{109}Cd	22	209	0.79	3.6	0.213
^{109}Cd	25	226	0.60	2.4	0.200
^{241}Am	60	447	0.70	1.2	0.130
^{109}Cd	80	627	0.59	0.7	0.107
^{57}Co	122	842	0.57	0.5	0.091
^{57}Co	136	933	0.75	0.5	0.086

For all the isotopes used, the number of counts in the peak centroid was at least 30,000.

Figures 3.4 and 3.5 show the energy resolution as a function of energy, E and $E^{-1/2}$ respectively. An example of the calculation of the FWHM using the NEMA method is shown below for the Am^{241} 59.6 keV photopeak.

The photopeak centroid P was 447 and (P) = 47503. Thus P/2 = (D') = (D) = 23704

A = 449 (A) = 34704

A'= 446 (A') = 35030

B = 450 (B) = 18513

B'= 445 (B') = 21018

The FWHM is obtained using equation 3.1, namely FWHM = D-D'=A-A'+A'-D'+D-A (in channel numbers).

$$A-A' = 3 \text{ (channel numbers)}$$

$$A'-D' = \frac{[(A')-(D')][A'-B']}{(A')-(B')} = \frac{35030 - 23752}{35030 - 21080} \times 1 = 0.805$$

$$D-A = |A-D = \frac{[(A)-(D)][A-B]}{(A)-(B)} = \frac{(34704 - 23752)}{34704 - 18513} \times 1 = 0.676$$

Thus FWHM = (3.000 + 0.805 + 0.676) channel numbers

= 4.481 channels

From the energy calibration graph (figure 3.3), we have a slope of 0.157 keV per channel. Therefore in terms of

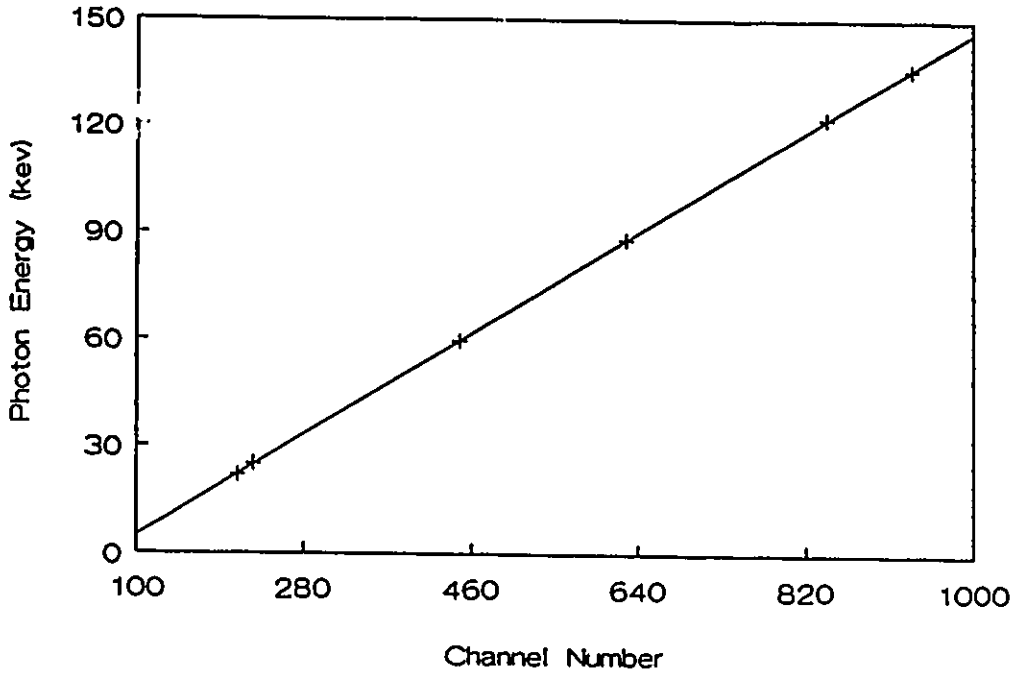

Figure 3.3 HPGe Detector Energy Calibration:
Energy VS Photopeak Centroid.

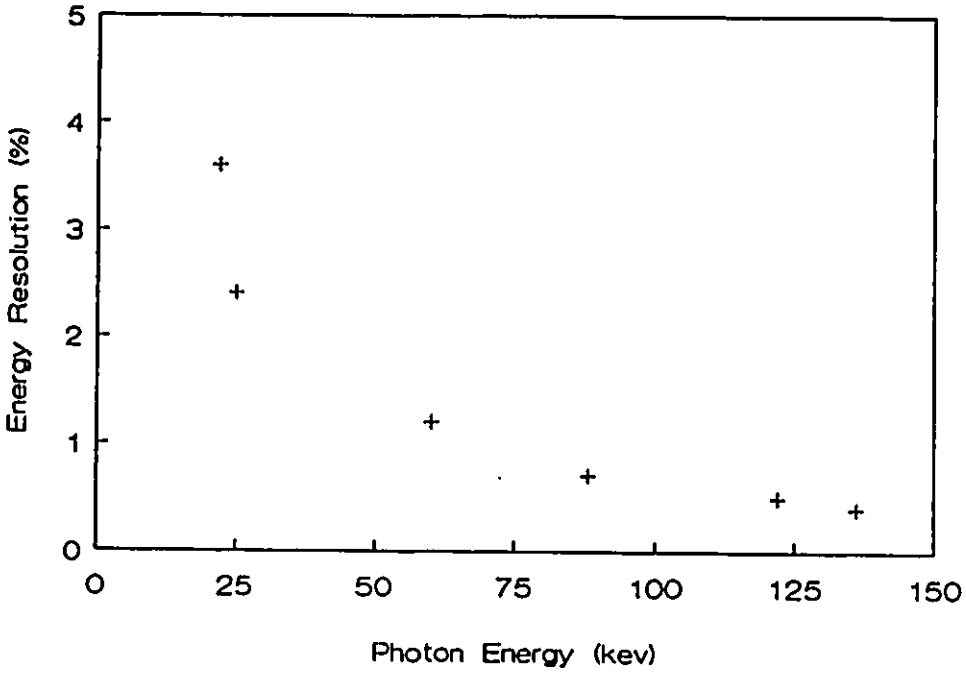

Figure 3.4 HPGe Detector Energy Resolution; FWHM/E (%) VS Photon Energy.

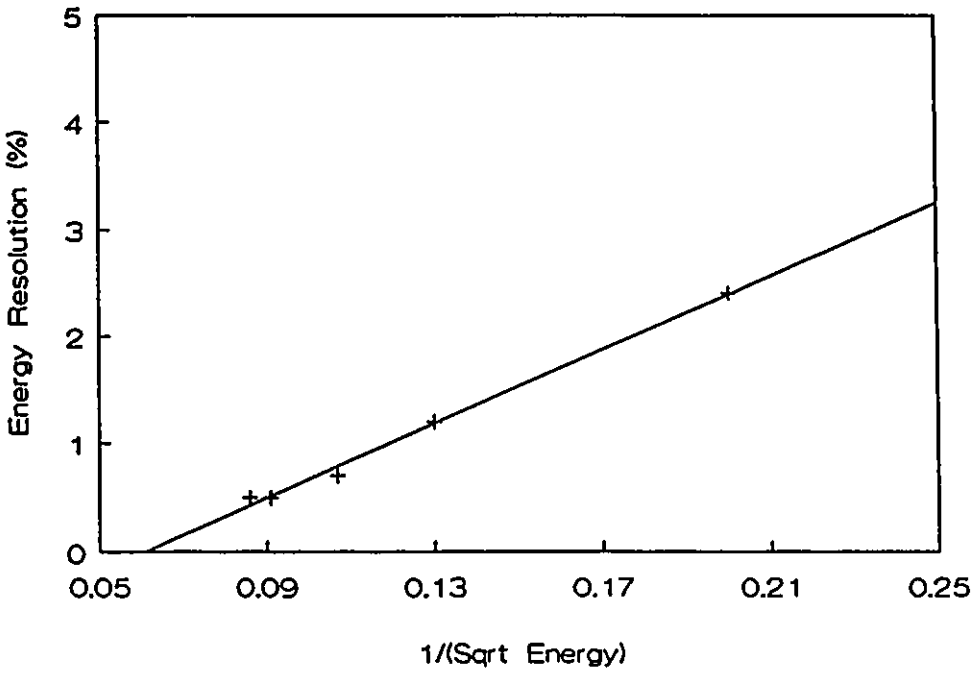

Figure 3.5 HPGe Detector Energy Resolution;

FWHM/E (%) VS $1/(E)^{\frac{1}{2}}$

energy, the full width at half maximum is 4.481 x 0.157 keV per channel, that is, 0.704 keV, at 59.6 keV. The energy resolution for the other peaks given in Table 3.2 was obtained in a similar way.

3.4 Detection Efficiency

3.4.1 Theory

The efficiency of a given detector at a particular energy, E, can be evaluated at a given distance by measuring the number of full energy peak events detected per unit time from a standardised source. The full energy peak efficiency ϵ_E, including all geometric and attenuation factors is given by the following expression:

$$\epsilon_E = R_E/b_E N \qquad (3.5)$$

where R_E is the number of photopeak counts per unit time, b_E is the emissions probability of photons of energy E and N is the disintegration rate of the standard source. Efficiency can also be written as

$$\epsilon_E = \epsilon_R G(E) \qquad (3.6)$$

where

$$\epsilon_R = \epsilon_a \cdot f_a \cdot f_{Au} \cdot f_d \cdot f_e \cdot f_c \cdot \epsilon_S \qquad (3.7)$$

and G(E) is a geometric factor which is the solid angle subtended at the source by a plane within the detector and parallel to its surface and located at the mean photon interaction depth, h(E). ϵ_R is the relative detector

efficiency. It is the product of intrinsic efficiency ϵ_a and several correction factors. The intrinsic efficiency refers to the sensitive volume of the detector, and assumes complete charge collection. The factors f_a, f_{Au} and f_d correct for attenuation in materials external to the detector face (such as air and the beryllium window), in the thin gold contact on the detector face and in the dead layer separating the gold contact from the sensitive volume, respectively. The other factors f_e and f_c correct for the escape of germanium x-rays from the sensitive volume and for effects of collimation, if any. ϵ_s is the efficiency of total charge collection.

In the high energy region (but below the pair production threshold) the relative efficiency ϵ_R simplifies to:

$$\epsilon_R \simeq \epsilon_a \epsilon_s \tag{3.8}$$

where the presence of multiple events leading to a full energy pulse requires that for normal photon incidence,

$$\epsilon_a = 1 - \exp[-\mu(E)d] \tag{3.9}$$

and

$$\mu(E) = \mu_{p.e}(E) + a(E)\mu_c(E) \tag{3.10}$$

where $\mu_{p.e}$ and μ_c are the total linear photoelectric and Compton attenuation coefficients respectively and d is the sensitive depth of the detector. The a(E) factor is the probability that Compton events occurring within the

sensitive volume deposit the full energy of the incident photon. It must be stated, again, that complete charge collection is assumed.

At low energies the intrinsic efficiency, for normal incidence, is given by:

$$\epsilon_a = 1 - \exp(-\mu_t d) \tag{3.9a}$$

where μ_t is the total attenuation coefficient.

The attenuation correction f_a, excluding self absorption in the source, is given by:

$$f_a = \exp[\Sigma(-\mu_i x_i)] \tag{3.11}$$

where μ_i and x_i are the total attenuation coefficient and thickness of the ith element placed between the source and the detector face.

The gold layer correction is for attenuation in the gold contact evaporated on the detector surface. The average thickness, x_{Au}, of this layer is usually about 300 A. To determine this thickness, gold L x-rays may be fluoresced by any convenient source of photons with energy greater than 11.92 keV, the L_3 absorption edge. The gold layer thickness is then obtained from the expression of Hansen et al. (1973)

$$x_{Au} = \frac{2C_{L\alpha}\,\bar{\epsilon}_\gamma}{w_3 f_{L\alpha} C_\gamma \bar{\epsilon}_{L\alpha} \bar{\epsilon}_\gamma} [\mu_1(f_{13}+f_{12}+f_{23}) + \mu_2 f_{23} + \mu_3]^{-1} \tag{3.12}$$

where $C_{L\alpha}$ and C_γ are the respective counting rates of gold

L_α x-rays and the excitation photons. $\bar{\epsilon}_{L\alpha}$ and $\bar{\epsilon}_\gamma$ are their respective mean intrinsic detection efficiencies. The L_3 subshell fluorescence yield for gold is $w_3(=0.13)$; μ_1, μ_2 and μ_3 are the mean L_1, L_2 and L_3 subshell attenuation coefficients for gold at the energy of the incident photons. The Coster-Kronig yields, f_{13}, f_{12} and f_{23}, are 0.56, 0.14 and 0.17 respectively for gold and the quantity $f_{L\alpha}(\simeq 0.8)$ is the intensity ratio of the L_α x-ray transitions to the sum of L_3 x-ray transitions. It is assumed in equation 3.12, that one half of the excited L_α x-rays are emitted towards the detector.

Germanium dead layer thicknesses, x_{Ge}, greater than 3000 A may be determined concurrently with the gold contact thickness by application of the expression:

$$x_{Ge} = \frac{2C_K\epsilon_\gamma}{C_\gamma\epsilon_K\mu_K w_K} \qquad (3.13)$$

where C_K/C_γ is the observed ratio of the intensities of the Ge K-x rays and the excitation photons; μ_K is the mean K shell attenuation co-efficient in Ge for excitation photons; w_K is the Ge K shell fluorescence yield and $\epsilon_K/\epsilon_\gamma$ is the ratio of intrinsic efficiencies for Ge K-x rays and the excitation photons.

Normally the specification of the beryllium window thickness issued by the manufacturer is adequate to estimate

the fractional absorption in the beryllium window.

The geometric factor is the fractional solid angle subtended by a point source at a distance r from the surface of a detector of radius a and is given by the expression:

$$G(E) = \frac{1}{2}\,(1 - [r + h(E)]\{[r + h(E)]^2 + a^2\}^{-1/2}) \qquad (3.14)$$

where h(E), the mean interaction depth for photons of energy E, is introduced in order to take into account (to a close approximation), the escape of photons from the sides of the detector. In the case where r>>a, h(E) is closely approximated by:

$$h(E) = \frac{\int_0^d h\,\exp(-\mu h)\,dh}{\int_0^d \exp(-\mu h)\,dh} \qquad (3.15)$$

which equals

$$\frac{[1-\exp(-\mu d)(1+\mu d)]}{\mu[1-\exp(-\mu d)]} \qquad (3.15a)$$

where μ is the total attenuation coefficient in germanium and d is the sensitive thickness of the detector. A theoretical analysis (Smith, 1971) of the dependence of efficiency on the source-to-detector distance, specifies an analogous quantity, h(E) given by:

$$h(E) = \frac{1}{\mu} \ln \left[\frac{2}{1 + \exp(-\mu d)} \right] \qquad (3.15b)$$

For the purposes of this exercise, where relative efficiencies were required, some of the attenuation factors described above were ignored and the geometric factor was approximated to:

$$G = \frac{A}{4\pi r^2} \qquad (3.16)$$

where A is the surface area of the detector and r is the distance from the source to the active-surface of the detector, see figure 3.1.

3.4.2 Materials and Method

Efficiencies were measured using the geometrical arrangement shown in figure 3.1. From this geometry and the data of table 3.1, the simplified geometric factor was calculated according to equation 3.16 and found to be 3.5×10^{-3}. The same sources used for energy calibration and resolution were used for efficiency determination.

The factor R_E (equation 3.5) was determined for each photopeak by setting a window about the full energy peak and integrating the counts within the window limits using the PDP 1103. The background counts obtained by a simple straight line interpolation between the window extremities,

were subtracted.

3.4.3 Results

Some of the factors in equation 3.7, for example, f_{Au} and f_d, were not determined as the thickness of the gold contact, x_{Au} and the germanium dead layer x_{Ge}, are unknown. Thus a truncated form of equation 3.7 was used to determine the theoretical efficiency at 60 keV.

The equations used were:

$$\epsilon = \epsilon_R G(E) \qquad (3.6)$$

and

$$\epsilon_R = \epsilon_a . G . f_a . f_{Be} \qquad (3.7a)$$

The theoretical efficiency for the high purity planar germanium detector at 60 keV was calculated to be 3.4×10^{-3} compared to a measured value of $2.8 \times 10^{-3} \pm 0.4 \times 10^{-3}$. The attenuation coefficient values used are given in tables 3.3 and 3.4. Experimental values were determined using equation 3.5 and are tabulated in table 3.5. The variation of absolute efficiency and relative efficiency with gamma ray energy is shown in figures 3.6 and 3.7 respectively. The significant observations from both graphs is the sharp drop in efficiency at the energies below about 30 keV. There are two probable explanations for this. One is the increase at low energies in the absorption by all materials between the source and the detector crystal. The other is the germanium

Table 3.3 Linear Attenuation Coefficients for Detector Materials at Selected Energies

Absorber/ material	density g/cm^3	linear attenuation coefficient (cm^{-1}) 60 keV	80 keV	100 keV
Gold	19.282	87.310	42.131	99.457
air (dry, at sea level)	1.29×10^{-3}	0.241×10^{-3}	0.214×10^{-3}	0.199×10^{-3}
Beryllium	1.845	0.275	0.258	0.245
Germanium	5.308	10.674	5.017	2.933

Table 3.4 Attenuation Factors in Air and Beryllium for Selected Energies

Absorber	60 keV	80 keV	100 keV
f_{air} (d_{air} = 95 mm)	0.9977	0.9980	0.9981
f_{Be} (d_{Be} = 0.2 mm)	0.9945	0.9949	0.9951

Table 3.5 Detector Efficiency at Selected Photon Energies

Source	Activity (MBq)	Energy (keV)	Absolute Intensity (b_E)(%)	Efficiency Absolute ($\times 10^{-3}$)	Efficiency Relative	(1-Relative)
^{241}Am	0.404	14	13.5	1.38	0.52	0.48
		18	21.0	1.70	0.63	0.37
		21	5.0			
		26	2.5			
		60	35.3	2.75	1.00	0.00
^{57}Co	0.004	122	85.2	2.00	0.74	0.26
		136	11.1	1.67	0.63	0.37
^{133}Ba	0.305	30-36	123	2.75	1.00	0.00
		80-81	36.2	2.64	0.96	0.04

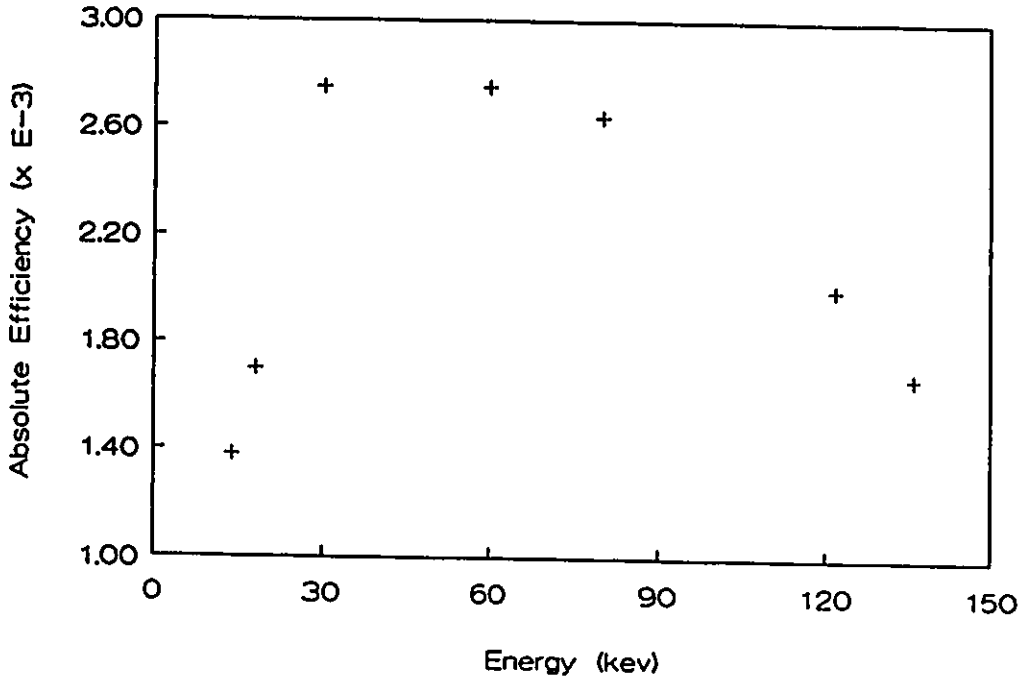

Figure 3.6 HPGe Detector Absolute Efficiency VS Energy.

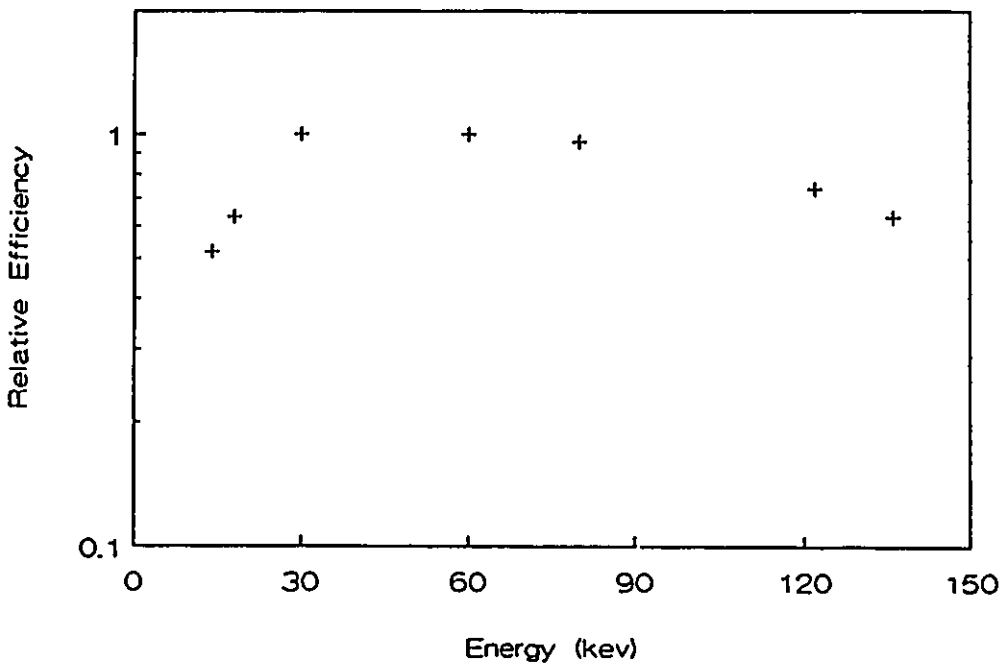

Figure 3.7 HPGe Detector Relative Efficiency VS Energy.

dead layer on the crystal surface.

At higher energies (above 100 keV), the detector efficiency again falls. This is due to the fact that at these energies, the Compton effect is the dominant attenuating mechanism and since the detector size is small, an increasing fraction of Compton scattered photons escape.

3.5 Conclusion

Detector characterisation was achieved and the following values were measured:

(i) the energy calibration fitted a straight line with a correlation coefficient of virtually 1.0 and a slope of 0.157 keV per channel.

(ii) Energy resolution was found to be 570 eV (full width at half maximum) at 122 keV which agrees with the manufacturer's determined value.

There is a good agreement between experimentally determined and theoretical values of absolute efficiency though the theoretical values are slightly higher. This is to be expected since some factors like the attenuation values for the gold contact layer and the germanium dead layer could not be determined. In the next section the parameters that are important in the selection of source photon energy and scattering angle are examined.

3.6 Selection of Photon Energy and Scattering Angle

3.6.1 Introduction

Theoretically, the mass of mineral per unit volume of trabecular bone can be measured using coherent gamma ray scattering. The potential of coherent scattering stems from the fact that the probability of occurrence is a function of both the atomic number (or the effective atomic number) and density. As discussed in Chapter 1 other techniques for mineral concentration measurement employ Compton scattering or the ratio of coherent to Compton scattering, both of which will be less sensitive than the use of coherent scattering alone. This can be seen by considering the linear interaction coefficients, μ, of the two processes. For coherent scattering, this coefficient is given by:

$$\mu_{coh} \propto n\sigma_{coh} \tag{3.17}$$

where n is the number of atoms per unit volume and σ_{coh} is the coherent atomic cross section. The atomic density is given by $n = N_o\rho/A$ where N_o is Avogadro's number, A is the atomic mass number and ρ the density. The atomic cross section for coherent scattering varies approximately as the second power of the atomic number, z. Consequently for most elements except hydrogen equation equation 3.17 becomes

$$\mu_{coh} = N_o\rho Z^2/A = k\rho Z \tag{3.18}$$

where k is a constant.

The Compton scattering coefficient is given by

$$\mu_{inc} \propto n\sigma_{inc} \qquad (3.19)$$

The Compton atomic cross-section, σ_{inc}, varies approximately as the atomic number only. So equation 3.19 becomes

$$\mu_{inc} = N_o\rho Z/A = N_o\rho Z/A = k\rho \qquad (3.20)$$

Since virtually all bone mineral disorders lead to loss of bone mineral, progression of disease will be associated with reductions in both density and effective atomic number. Hence equation 3.18 suggests that the process of coherent scattering will inevitably be a more sensitive technique to disease progression. Compton scattering techniques will only respond to changes in density (equation 3.20), while methods dependent upon the coherent to Compton ratio will only respond to atomic number changes (ratio of equation 3.18 and 3.20).

The purpose of this section is to consider some of the factors which will have to be optimised in the development of a clinical bone mineral device based on coherent scattering.

3.6.2 Selection of Incident Photon Energy

At a given energy, the atomic coherent cross-section obeys a positive power function of the atomic number, Z, of the scatterer. Figure 3.8 shows the atomic coherent cross

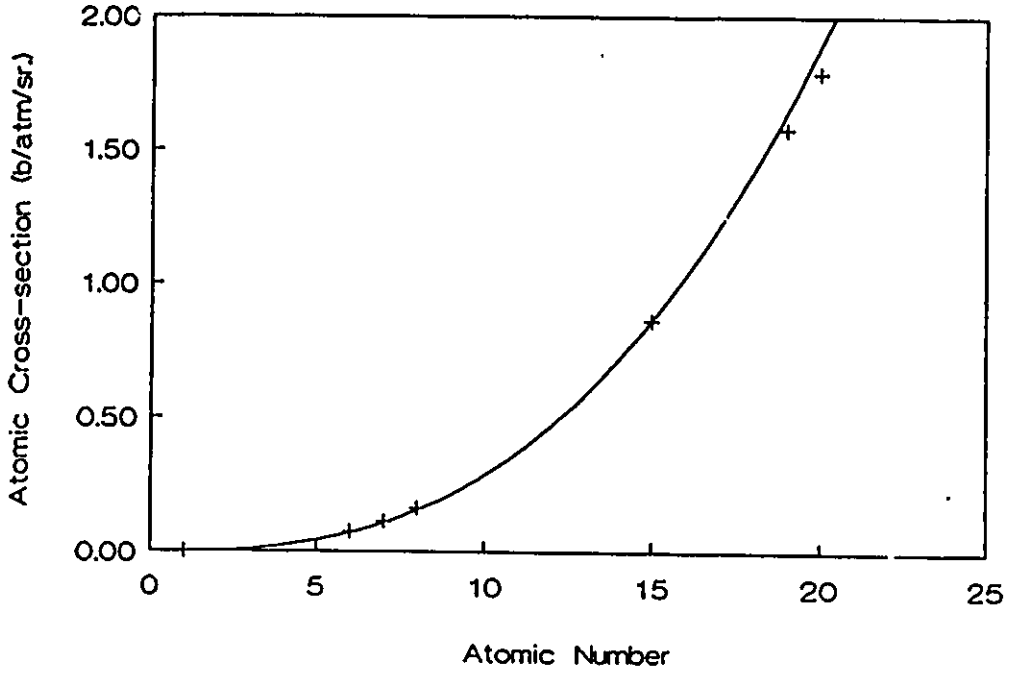

Figure 3.8 Dependence of the Total Coherent atomic cross section upon atomic number at 100kev.

sections at 100 keV for various elements taken from the tables of Veigele (1973). The fitted curve has the form aZ^n, where a is a constant and the exponent n is 2.76. For photons of 100 keV the atomic cross section of a scatterer with an atomic number similar to cortical bone is at least an order of magnitude greater than that for a scatterer with an atomic number similar to soft tissue. However the parameter of concern in a clinical system will be the differential coherent cross-section which, as shown in figure 3.9 is also a power function of the atomic number of the scatterer. Figure 3.9 also shows that the differential cross section increases more rapidly with atomic number at larger scattering angles. This means that the sensitivity of a clinical system should be greater at a larger scattering angle. The atomic form factors data used to calculate differential cross sections was taken from the tables of Hubbell et al. (1975).

The differential coherent cross-section falls rapidly with energy (figure 3.10). At approximately 60 degrees, the cross section falls by a factor of 10 for an increase in energy of from about 30 to 80 keV. It is also pertinent to mention here that the spectral resolution, that is, the energy separation between the coherent and Compton scattered photons improves with increasing angle. On the other hand, the absorbed dose to bone is higher at low photon energies,

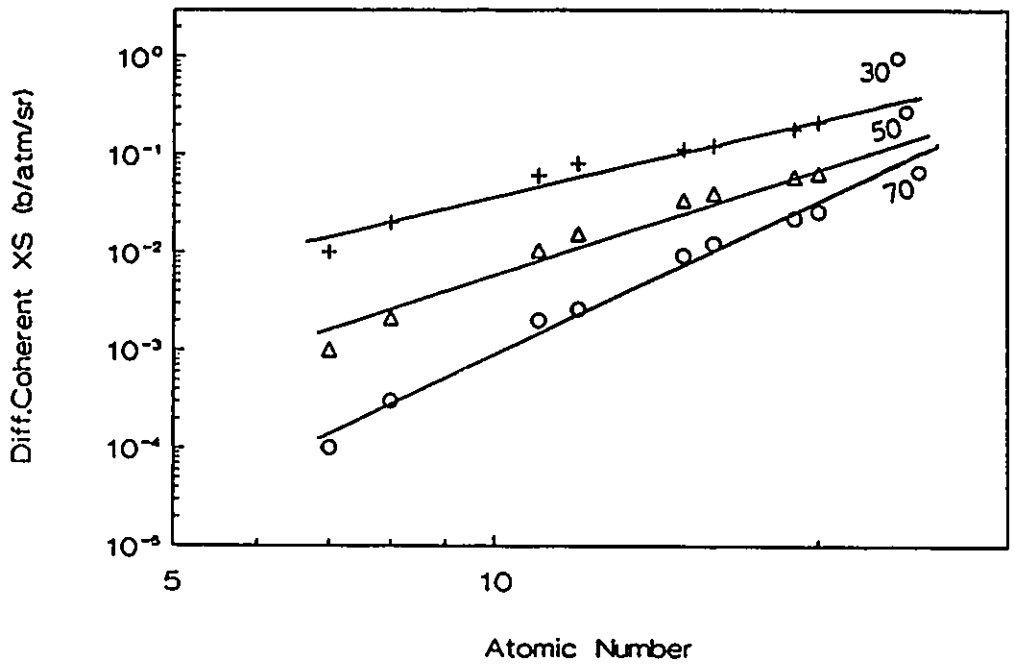

Figure 3.9 The Differential Coherent cross section at 100kev VS atomic number for scattering angles of 30^{o},50^{o} and 70^{o}.

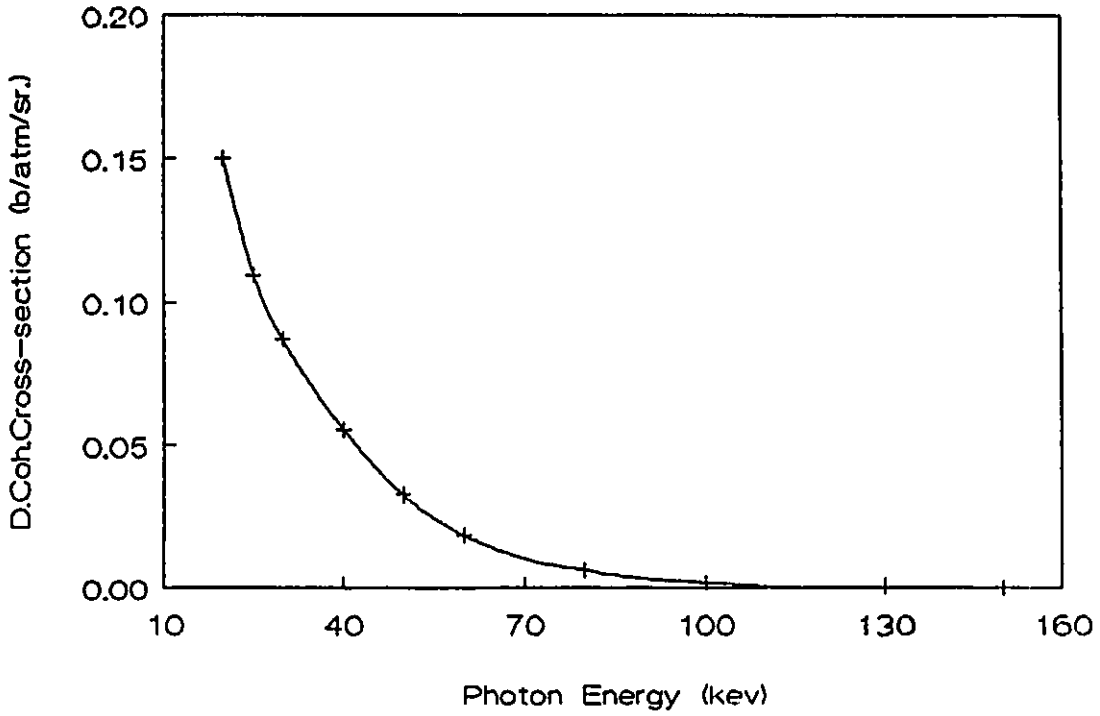

Figure 3.10 Differential coherent cross section at a fixed angle (59.5^{o}) VS Photon Energy for an element of atomic number 9.

being about four times as high at 50 keV as it is at 100 keV (figure 3.11). Thus the number of scattered photons per unit dose to the patient falls as the scattering angle increases leading to a reduction in statistical reliability. Clearly a compromise exists between spectral resolution, differential coherent cross-section (hence counting rates) and radiation dose. The desired photon energy was calculated from the energy dependencies of the efficiency of the available detector, the energy resolution of the detector, the absorbed dose to bone and the differential coherent cross section. The effect of each of these factors on the system performance is shown in figure 3.12. The overall energy dependence was computed as the sum of each individual factor and is shown in the same figure. It is evident that Sm^{153}, with its gamma photon energy of 103 keV, is acceptable as a source for these studies.

3.7 Production of the Sm^{153} Source

The isotope used as a source in these experiments, Sm^{153} was produced in the McMaster University Nuclear Reactor by neutron activation of stable Sm^{153}.

3.7.1 Theory of isotope production by neutron activation

Consider the sample (or neutron activation target) of mass m being irradiated in a neutron flux, $\phi(E)$ at neutron

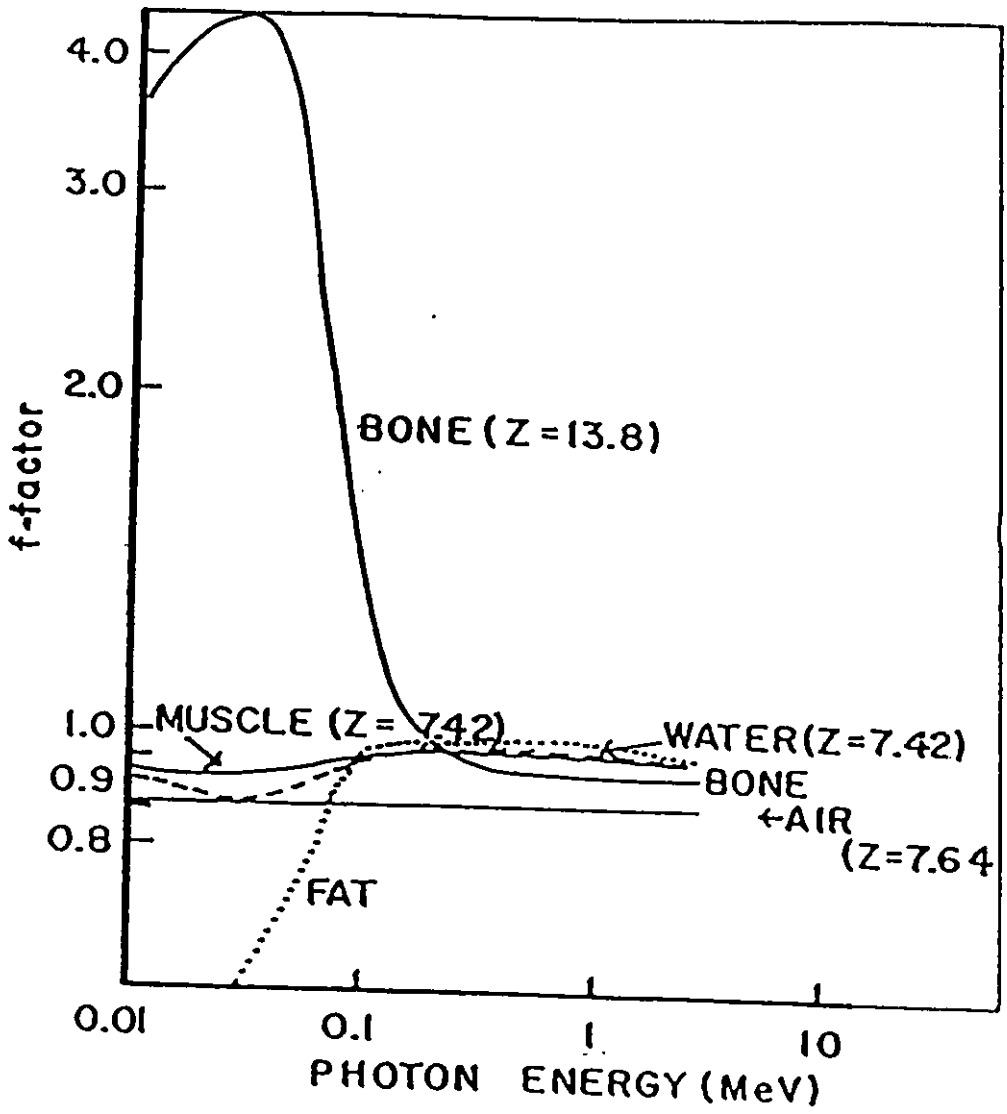

Figure 3.11 Absorbed dose F-factor vs Photon Energy for various substances. (after Hendee 1970)

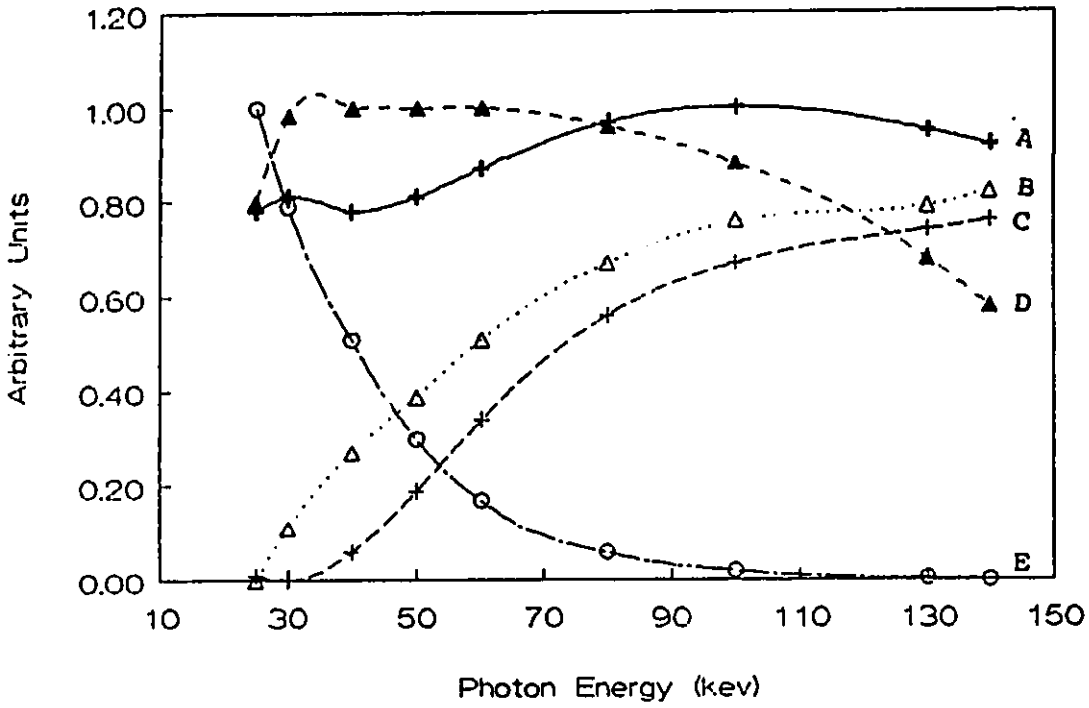

Figure 3.12 Selection of photon energy: figure of merit (A) obtained by considering the normalised detector efficiency (D), the complement of the normalised energy resolution (B), the complement of the normalised bone dose f-factor(C) and the normalised differential coherent cross section (E).

energy E, with $\sigma_j(E)$ as the neutron absorption cross section of the isotope of atomic mass A_j. Let λ_{j+1} be the decay constant of the isotope with atomic mass A_{j+1}, w_j be the weight fraction in the sample of isotope A_j, $N_j(t)$ the number of atoms of nuclide with atomic mass A_j present at time t, $\sigma_{j+1}(E)$ the neutron absorption cross section of isotope A_{j+1} at neutron energy E and m the mass of the element whose isotope A_j captures the neutron.

In general, as a consequence of neutron absorption the target atoms of atomic mass A_j are transformed into atoms with atomic mass A_{j+1} according to the equation

$$ {}^{A_j}_{Z_j}X + n \rightarrow {}^{A_{j+1}}_{Z_j}X \qquad (3.21) $$

where Z is the atomic number and ${}^{A_j}_{Z_j}X$ is the target isotope.

Atoms of the type A_{j+1} may be radioactive and may decay or they may be transformed by absorbing a neutron. The transformation of target atoms is described by the equation:

$$ \frac{-dN_j(t)}{dt} = N_j(t) \int_0^\infty \sigma_j(E)\ \phi(E)\ dE \qquad (3.22) $$

Equation 3.22 assumes that the presence of the target does not perturb the flux (Hanna, 1961; Hanna, 1963). The integration over energy in equation 3.22 is usually written

as (Tsoulfanidis 1983):

$$\int_0^\infty \sigma_j(E)\ \phi(E)\ dE = \vec{\sigma}_j \int_0^\infty \phi(E)dE$$

$$= \vec{\sigma}_j \phi \qquad (3.23)$$

$$= \sigma_j \phi$$

where the bar over the cross section symbol indicates an average cross-section over the neutron energy spectrum. While the bar is usually dropped, it is always understood that the average cross section is used.

The solution of equation 3.22, can be written using equation 3.23, as:

$$N_j(t) = N_j(0)e^{-\sigma_j \phi t} \qquad (3.24)$$

where $N_j(0) = \frac{w_j m N_A}{A_j}$ is the number of atoms of isotope A_j at time t = 0, and N_A is Avogadro's number. The net rate of production of the A_{j+1} isotope is therefore expressed as:

$$\frac{dN_{j+1}(t)}{dt} = N_j(t)\sigma_j \phi - N_{j+1}\sigma_{j+1}\phi(t) - \lambda_{j+1}N_{j+1}(t) \qquad (3.25)$$

where the terms on the right hand side of equation 3.25 are the production rate, the destruction rate and decay rate

respectively. The solution to equation 3.25, with the initial condition $N_{j+1}(t) = 0$, can be written as:

$$N_{j+1}(t) = \frac{\sigma_j N_j(0)\phi}{\lambda_{j+1}+\sigma_{j+1}\phi-\sigma_j\phi}(\exp(-\sigma_j\phi t) - \exp[-(\lambda_{j+1}+\sigma_{j+1}\phi)t]) \tag{3.26}$$

The activity of the above target is $A_{j+1}(t)$ and after irradiation for time t, it will be given by:

$$A_{j+1}(t) = N_{j+1}(t)\lambda_{j+1}$$

$$= \frac{\sigma_j N_j(0)\phi}{1+(\sigma_{j+1}-\sigma_j)\left(\frac{\phi}{\lambda_{j+1}}\right)} (\exp(-\sigma_j\phi t)-\exp[-(\lambda_{j+1}+\phi_{j+1}\phi)t]) \tag{3.27}$$

Equation 3.27 is the most general case scenario. Practical targets are chosen such that the fraction of the target nuclei destroyed is negligible, that is $\sigma_j\phi t<<1$ and the radioisotope produced has a neutron absorption cross section such that $\lambda_{j+1}>>\sigma_{j+1}\phi$.

With the above conditions satisfied, equation 3.27 reduced to:

$$A_{j+1}(t) = \sigma_j N_j(0)\phi[1-\exp(-\lambda_{j+1}t)] \tag{3.28}$$

or

$$A(t) = \sigma m N_A \frac{\phi}{A}(1 - e^{-\lambda t}) \tag{3.28a}$$

after dropping the subscripts j and j+1.

The consequences of equation 3.28 are such that for irradiation times that are short compared to the half life of the radioisotope produced, the activity increases with time. If $\lambda_{j+1}t<<1$ then $e^{-\lambda_{j+1}t}$ can be written as $1-\lambda_{j+1}t$ and the activity A_{j+1} can be written as:

$$A_{j+1}(t) \simeq \sigma_j N_j(0)\phi\lambda_{j+1}t$$

$$= \sigma_j N_j(0)\ \phi\ \frac{\ell n2t}{\ell nT_{j+1}} \qquad (3.29)$$

where T_{j+1} is the half life of the isotope produced. For irradiation times many times longer than the half life of the radioisotope, the activity reaches a saturated value A_s, which can be expressed as:

$$A_s = \sigma_j N_j(0)\phi$$

$$= \sigma_m N_A\ \frac{\phi}{A} \qquad (3.30)$$

The time required to attain a given activity A(t) is obtained by re-arranging equation 3.28 to give the expression:

$$t = \frac{T}{\ell n2}\ \ell n\ [1 - \frac{A(t)}{A_s}]$$

$$= -\frac{1}{\lambda}\ \ell n(1 - \frac{A(t)}{N\sigma\phi}) \qquad (3.31)$$

where $N = mN_A/A$ and is the number of atoms in the irradiated target.

3.7.2 Source production

The number of atoms of Sm^{152} in Sm_2O_3 for a given sample weight is N_{152} and is equal to N in equation 3.31. For Sm^{153} source production it was obtained from:

$$N_{152} = m \times \frac{304}{368} \times \frac{N_A}{152} \qquad (3.32)$$

where m is the mass of Sm_2O_3.

The neutron flux, ϕ (McMaster Reactor RIFLS position) is about 5×10^{12} neutrons cm^{-2} sec^{-1} at 2 MW power. The thermal neutron capture cross section, σ, used was 210 barns (WSU-NRC, 1970) and the decay constant λ for Sm^{153} is 0.015 hr^{-1}.

3.7.3 Sample preparation method

Samples for irradiation were prepared by a method which is now standard at the McMaster Reactor (Davis and Webber, 1978). Approximately 200 mg of Sm_2O_3 (98.2%, Oak Ridge National Laboratory) were thoroughly mixed with sufficient graphite powder to fill a graphite capsule of outer diameter 2.5 cm and height 2.5 cm. The Sm_2O_3-graphite mixture formed a cylinder 1.5 cm in diameter and 0.5 cm

thick within the capsule. Several such capsules were made. When a source was required a capsule was irradiated for 24 hours. The RIFLS facility consists of two components: a water tight sample tube and a holder permanently positioned adjacent to the reactor core reflectors. The sample tube is an aluminum cylinder 1.8 metres long and 6 cm in internal diameter. An aluminum spacer positions a graphite sample holder about 30 cm above the bottom of the sample tube at the point of maximum neutron flux. The heat generated by the sample is conducted away to the walls of the sample tube by the graphite sample holder.

At the end of the irradiation the sample, (now a source) is stored under water for up to 48 hours to allow for reduction or elimination of contaminants such as Al^{28}, Mn^{54} and Na^{24} produced in the aluminum sample tube and Ar^{41} produced in the air within the tube.

The activity of the source was determined using a calibrated Ge(Li) detector. The ratio of the activity determined at 103.2 keV to the activity determined at 530 keV was used as an index of source self-absorption - for the sources used in the experiments, this ratio was 0.84 ± 0.07.

Source purity was assessed from spectral measurements with the Ge(Li) detector. From one of the highest activity sources (185GBq) of Sm^{153} produced, less than 7.4×10^4 Bq of

Eu^{152} ($T_{1/2}$ 17.7 yrs), ^{154}Eu (16 yrs), ^{155}Eu (1.8 yrs), ^{153}Gd (242 days) and ^{46}Sc were present as contaminants. Table 3.6 lists the major emissions from the ^{153}Sm source.

3.8 Peak Area Derivation

The area under the coherent peak observed with the HPGe detector for 103 keV photons was determined by fitting the data to a function f(x), of the type

$$f(x)=\alpha_0 + \alpha_1 x + \alpha_2 x^2 + \alpha_3 x^3 + \alpha_4 x^4 + \frac{\alpha_5}{x} + \alpha_6 \exp\left\{\frac{-(x-x_0)^2}{2\sigma^2}\right\} \quad (3.33)$$

where x is the channel number, α's are parameters to be fit and σ is a photopeak width parameter. The function is the conventional description of a photopeak and a continuum. The photopeak is considered to be Gaussian in shape while the continuum is represented by a polynomial. It was discovered that the high energy tail of the Compton peak beneath the coherent peak was changing rapidly thereby causing a poor fit. The addition of term in x^{-1}, improved the fit considerably as judged by reduced χ^2 values. The fitting procedure was achieved by writing a non-linear least squares programme (Appendix 1).

An example of the fitting is shown in figure 3.13. The crosses are the data points for a typical measurement and the continuous line is the fitted function. As a

Table 3.6 Major Emissions from ^{153}Sm Source

Energy (keV)	Origin	Absolute Intensity (%)	Intensity Relative to $K_{\alpha 1}$ (%)
103.2	γ-ray	28.2	
69.7	γ-ray	4.0	
97.5	γ-ray	0.7	
40.9	Eu $K_{\alpha 2}$ x-ray		53
41.54	Eu $K_{\alpha 1}$ x-ray		100
47.0	Eu $K_{\beta 1}$ x-ray		100
48.3	Eu $K_{\beta 2}$ x-ray		7

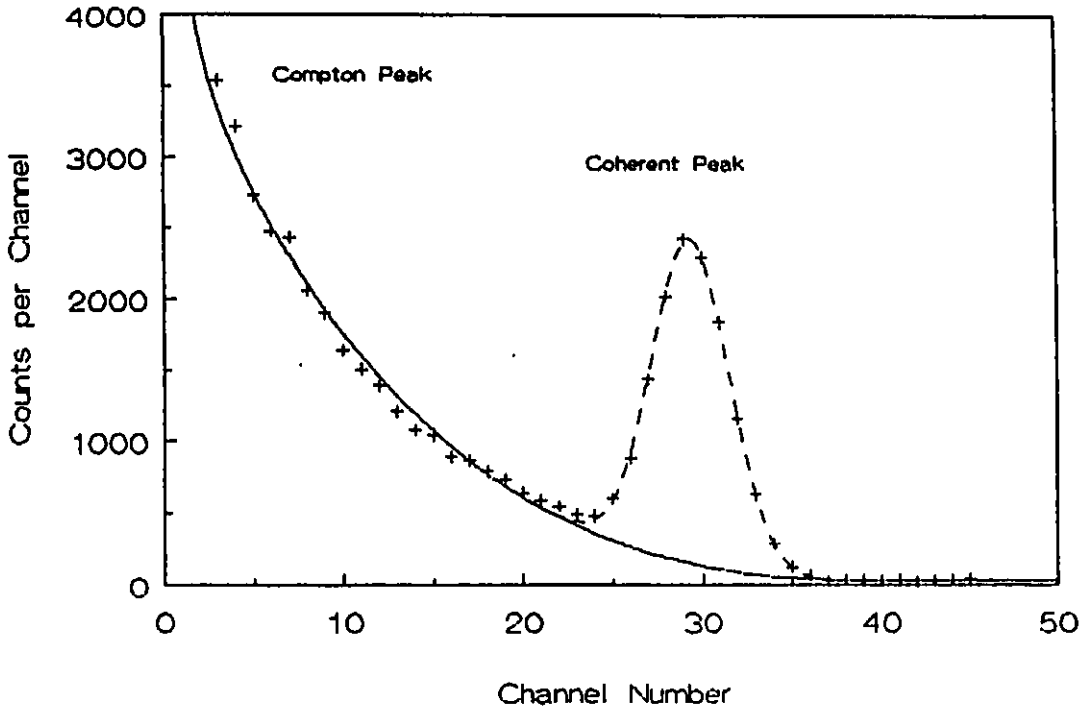

Figure 3.13 Illustrating the determination of the area under the coherent peak.

measure of the goodness of fit, reduced χ^2 (χ^2/number of degrees of freedom) values were calculated. They ranged from 1.0 to 2.5.

As a check on the validity of the above fitting programme, another fitting programme (Radford, 1985) available from Chalk River Nuclear Laboratories was used to determine the area under the coherent peak. The programme, called GELIFT, is a least-squares peak-fitting programme designed primarily for use in analysing gamma ray spectra from Germanium detectors. In this programme, the background is considered quadratic and the peak has three components: i) a Gaussian, ii) a skewed Gaussian and iii) a smoothed step function to increase the background on the low energy side of each peak. The latter two components can be each set to zero if not required.

The Gaussian component is the dominant component and arises from complete charge collection of a photoelectric event in the detector. The skewed Gaussian arises from incomplete collection due to a variety of reasons, for example, charge trapping by crystal dislocations. In a detector system with infinite resolution the Gaussian would be a delta-function and the skewed Gaussian would yield an exponential tail on the low-energy side. The convolution of a Gaussian resolution function with the exponential tail yields a function of the form (Radford, 1985).

$$f(x) = k\exp[(x-c)/\beta \cdot \mathrm{ERFC}[(x-c)/\sqrt{2}\sigma + \sigma/\sqrt{2}\beta]] \quad (3.34)$$

where k is a constant, x is the channel number, c and σ are the centroid and the standard deviation of the Gaussian component. β is the decay constant of the exponential. It corresponds to the skewness of the Gaussian.

Comparison of the coherent peak areas determined using our fitting programme and the GELIFT programme showed agreement to within five per cent.

CHAPTER 4

EXPERIMENTAL DESIGN CONSIDERATIONS AND PROCEDURES

4.1 Introduction

Source and detector collimation, together with the scattering angle, play a crucial role in determining the size of the scattering volume. In addition, the shape of the Compton scattered spectrum and the separation between the coherent and the Compton peaks each depend on both the collimation and the scattering angle.

This chapter examines these factors. It also describes the equipment and the experimental bone phantom materials used.

4.2 Experimental arrangement

The experimental arrangement was as shown in figure 4.1 A schematic diagram of the detector electronics is shown in figure 4.2. The high purity germanium detector (HPGe) and the Sm^{153} source were each housed in lead castle assemblies which, unless clamped in given positions on a goniometer-type rig, were free to rotate about a mutual vertical axis of rotation. In order to control beam divergence and detector field of view, both the source and detector collimation could be varied by

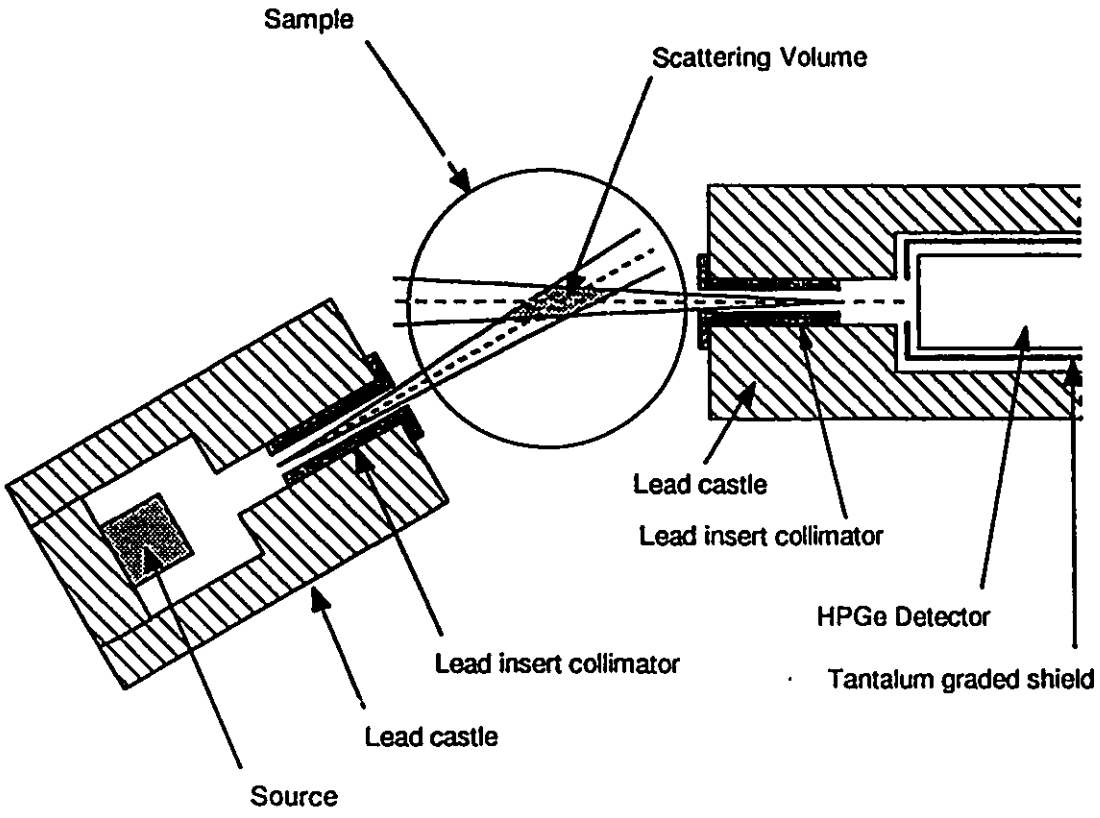

Figure 4.1 Experimental Arrangement

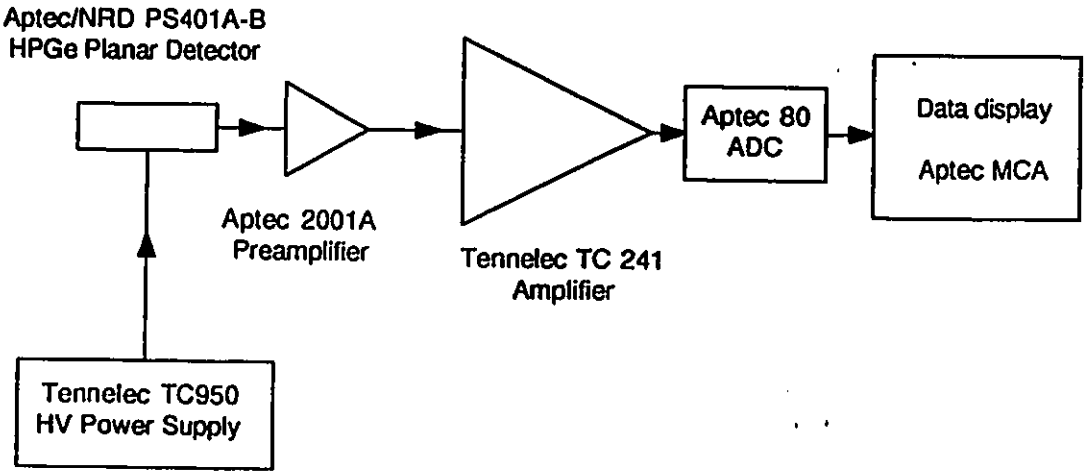

Figure 4.2 Schematic of data acquisition system

changing collimator inserts within the 1.6 cm diameter bores of the lead castles. Several types of inserts were tested. They included simple cylindrical bore lead inserts of length 2.5 cm and bore diameter 5 mm. Another insert consisted of 37 tantalum tubes 2.5 cm long, 1.5 mm internal diameter and 0.1 mm wall thickness packed into an aluminum cylinder. These cylinders fitted snugly inside the bores of the source and detector lead castles.

The bone phantom materials were aqueous solutions of dipotassium hydrogen phosphate and their preparation is discussed in detail in section 4.5. The solutions to be measured were contained in 50 mm diameter containers made of high density polyethylene of specific gravity 0.95. They were placed at the mutual vertical detector-source axis of rotation for the duration of a preset measuring time.

As shown in figure 4.1, the scattering volume, defined by the projections of the source and detector collimators, was such that it was restricted totally to the solution within the containers.

4.3 The effect of scattering angle

In addition to the effect on differential coherent scattering cross section discussed in Chapter 3, the scattering angle, θ, has a major influence on the size of the scattering volume. As indicated in figure 4.1, the

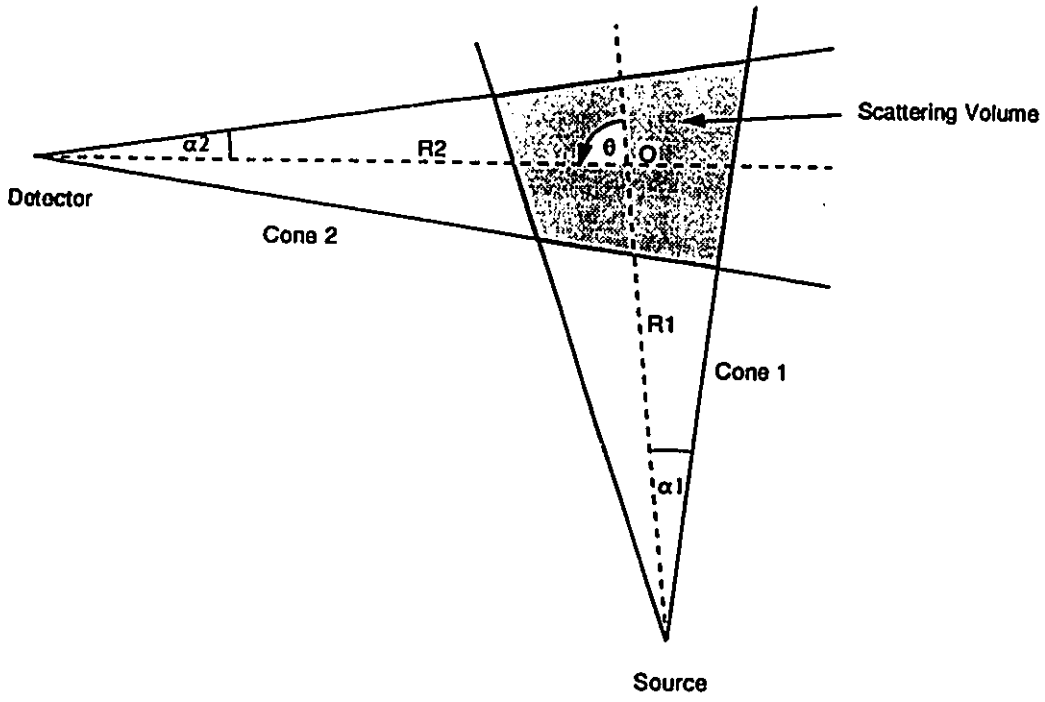

Figure 4.3 Illustration of scattering volume and cone angles and apex -to-point-of-intersection distances.

scattering volume is defined by the intersection of the projections of the source and detector collimators. It is also a function of the cone angles α_1 and α_2 and the cone apex-to-point-of-intersection distances R_1 and R_2 depicted in figure 4.3. Thus the scattering volume can be written as $V(\alpha_1\alpha_2R_1R_2\theta)$. A computer programme (Appendix 2) was written to provide a numerical estimate of the scattering volume. For fixed values of α and R, the scattering volume falls rapidly with scattering angle up to 90^o before it starts to increase again in a mirror-image manner. Figure 4.5 is a plot of the volume, relative to its value at 90^o, as a function of the scattering angle. For scattering angles up to 90^o, the variation of scattering volume with scattering angle can, as illustrated in figure 4.4 be fitted to a power function of the form.

$$\text{Volume} = k\theta^{-p} \qquad (r^2 = 0.99) \qquad (4.1)$$

where the exponent $p = 0.75\pm0.04$. The constant, k, depends on the values of the α's and the R's.

If the cone angles and the beam divergence are small, then for small distances near the point of intersection, the cones can be approximated by cylinders. This allows the use of an analytic expression, derived with the help of figure 4.6, to check the validity of the cone volumes determined by the computer programme. The analytic expression is the same as that obtained by Hubbell (1965) and was derived as

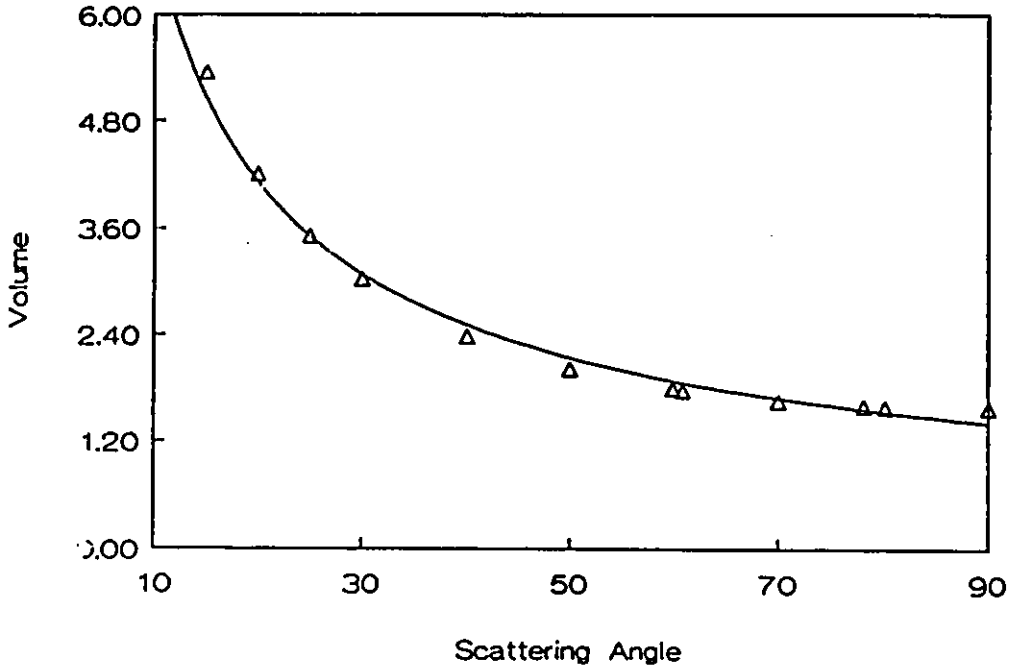

Figure 4.4 The volume of two intersecting cones as a function of scattering angle ($\alpha \simeq 5^{\circ}$ and $R \simeq 7.5$cm).

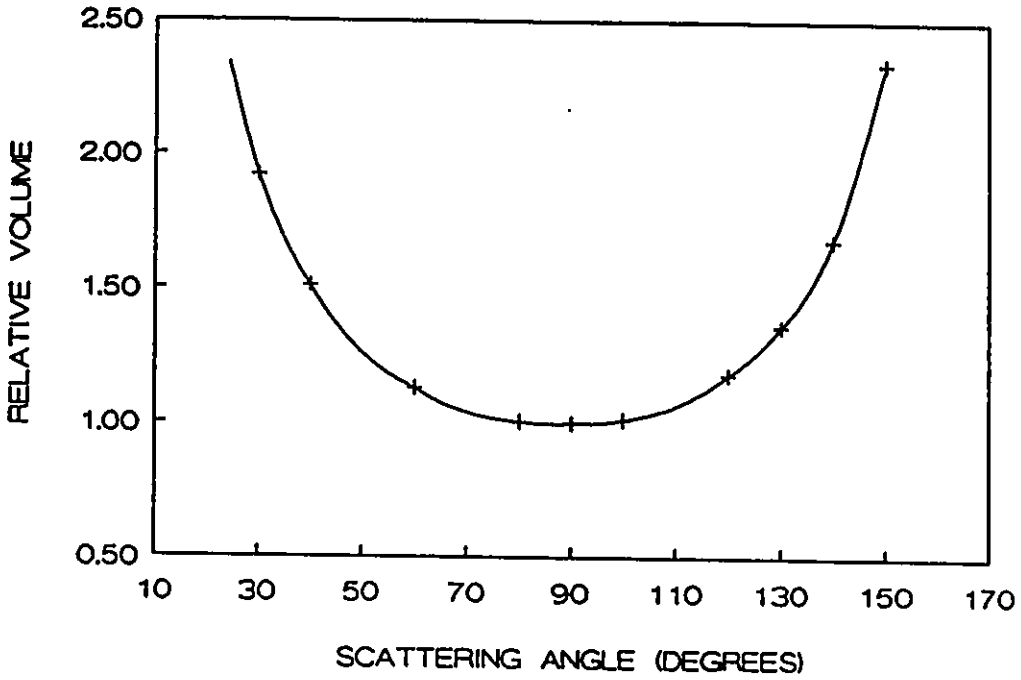

Figure 4.5 Scattering volume (relative to its value at 90^{o}) as a function of scattering angle.

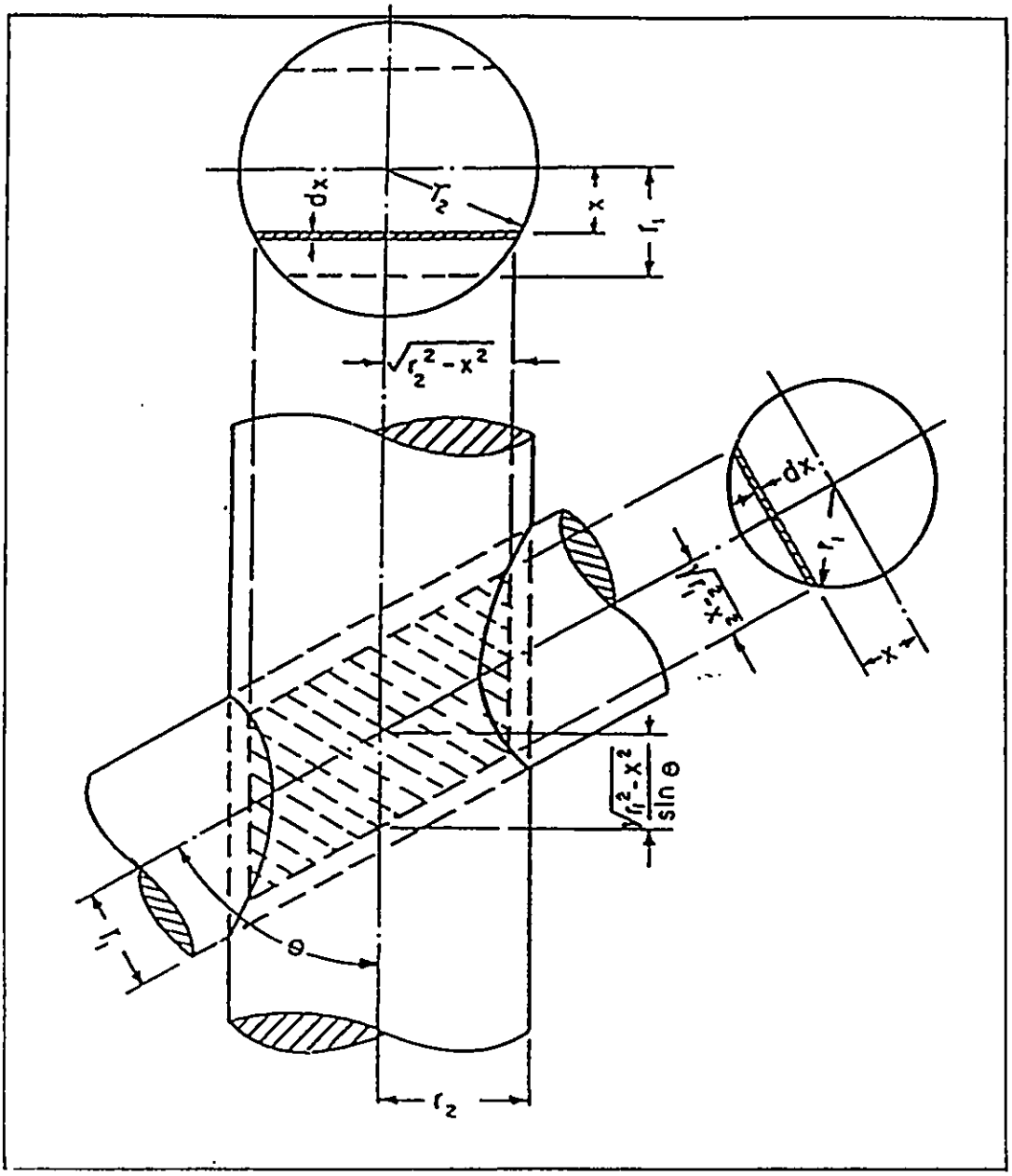

Figure 4.6 Illustrating the determination of the common volume of two intersecting cylinders (adapted from Hubbell, 1965).

follows: Consider the common volume of two cylinders of radii $r_1 \geq r_2$, with axes intersecting at angle θ (figure 4.6). Parallel to the cylinder axes at a distance x from them, a cross section which is a parallelogram can be drawn. The height of the parallelogram is $2(r_2^2-x^2)^{1/2}$ and its base is $2(r_1^2-x^2)^{1/2}/\sin\theta$. The volume integral is therefore given by

$$V(r_1 r_2 \theta) = \int_{r_2}^{r_1} 2(r_2^2-x^2)^{1/2} \frac{2(r_1^2-x^2)^{1/2}}{\sin\theta} dx$$

$$= \int_0^{r_1} (r_2^2-x^2)^{1/2} \cdot (r_1^2-x)^{1/2} dx \qquad (4.2)$$

and when $r_1 = r_2 = r$ as in our case, the integral reduces to

$$V(r,\theta) = \frac{8}{\sin\theta} \int_0^r (r^2-x^2) dx$$

$$= \frac{16r^3}{3\sin\theta} \qquad (4.3)$$

The two methods are in good agreement. The differences between the volume values determined by the two techniques are less than 10%.

The scattering angle also affects the separation between the Compton and coherent peaks. For example, at an angle of 30^o, the coherent peak is just resolved from the

Compton peak. The latter, for a primary photon of 103.2 keV, is centred at 100.48 keV and has a full width at tenth maximum (FWTM) of 2.42 keV. At 70^{o}, the coherent peak is well separated from the Compton peak whose centroid is at 91.09 keV and the FWTM is 3.24 keV. As illustrated in figure 4.7, while the separation between coherent and Compton peaks improves with increasing angle, the coherent intensity falls rapidly. In addition, small scattering angles and large scattering angles (compared to 90^{o}), produce asymmetrical scattering volumes, which can be difficult to restrict within a desired region of the object.

4.4 The effect of collimation

Source and detector collimation determine the size of the cone angles, α and therefore have an effect not only on the magnitude of the scattering volume but also on the peak spectral resolution. The former effect is clear from figure 4.1, depicting the experimental set-up. The cone angle α was determined for various collimator types. Collimation was varied by changing inserts in the bore of the lead castle housing the source. These inserts were either single or multiple-bore and also varied in length. Beam divergence was measured by placing x-ray films at known distances from the collimator face. Both the full width and the full width at half maximum for each film image were measured from film

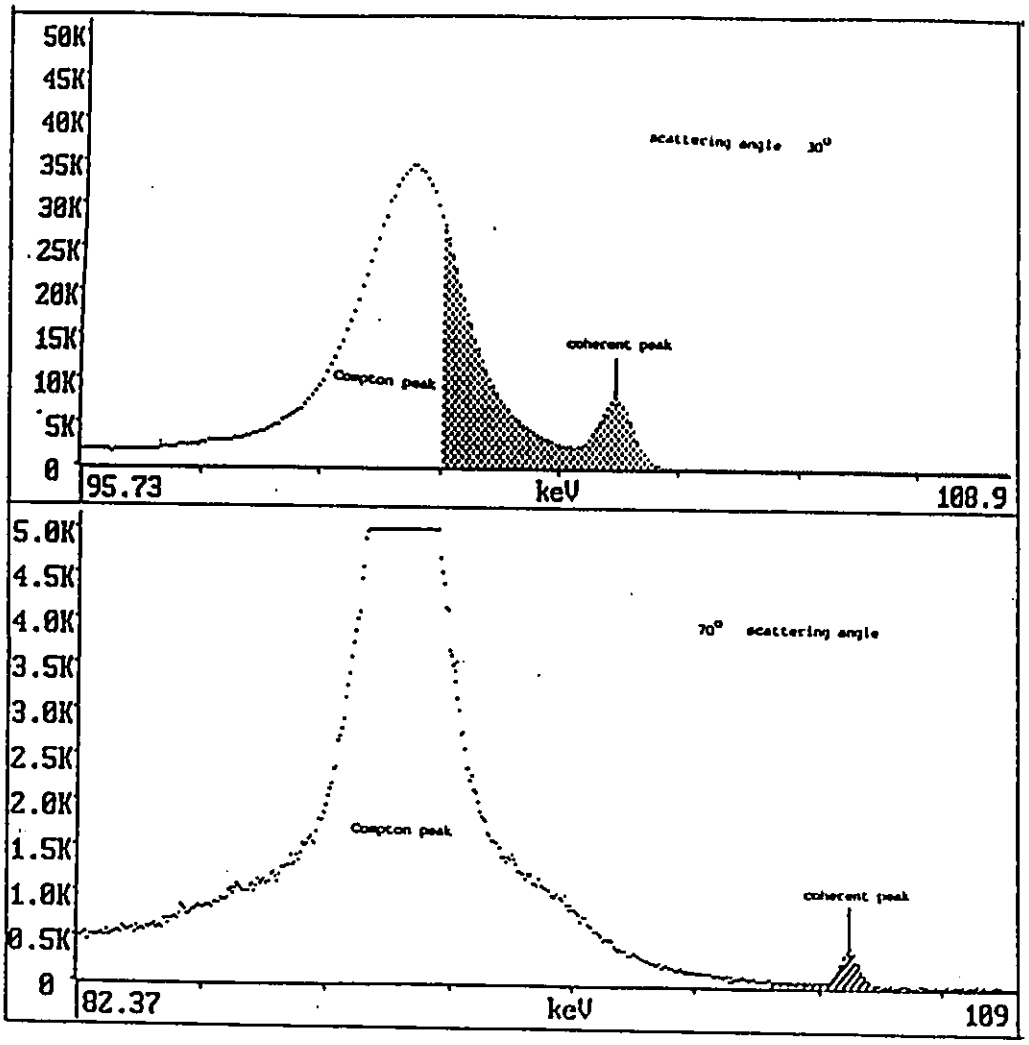

Figure 4.7 The effect of the scattering angle on peak spectral resolution and coherent count rates.

density profile obtained using a Joyce-Loebl scanning microdensitometer.

A plot of the beam full width and/or the beam full width-at-half maximum versus collimator to film distance is a straight line whose slope is the arctangent of the cone angle for the given collimator. Dividing the intercept by the slope gives the apparent position of the source with respect to the collimator face. This distance is added to the collimator-face-to-point-of-intersection distance to obtain the total distance between the cone apex and the point of intersection required for the computation of the scattering volume. As illustrated in figure 4.8, for a fixed scattering angle θ and distance, R, the variation of scattering volume with cone angle is a cubic function in α. The implication of this result is that beam divergence must be kept small so that scattering volume can be restricted to trabecular bone.

Whatever the nominal scattering angle, the maximum energy of the Compton scattered photon $h\nu'_{max}$, will depend upon the angular resolution which is, in turn, a function of the cone angle, α. A quantity, delta E, can be defined as the difference between the primary photon and $h\nu'_{max}$. It is a measure of the separation between the coherent and the most energetic Compton scattered photon. Figure 4.9 illustrates the variation of this separation with cone

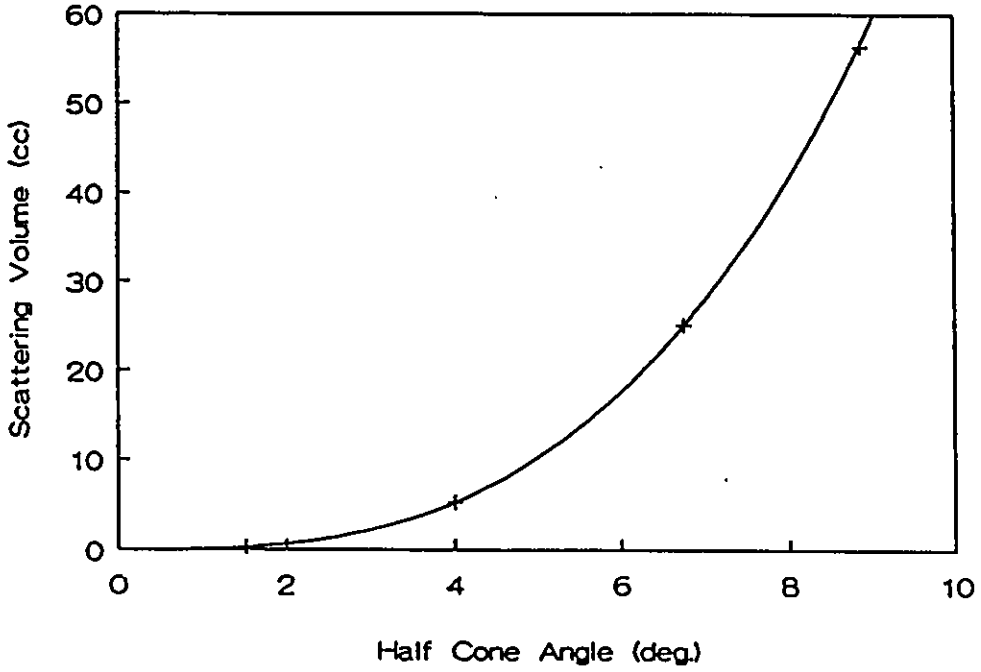

Figure 4.8 Scattering volume as a function of half cone angle, at a nominal scattering angle of 40°.

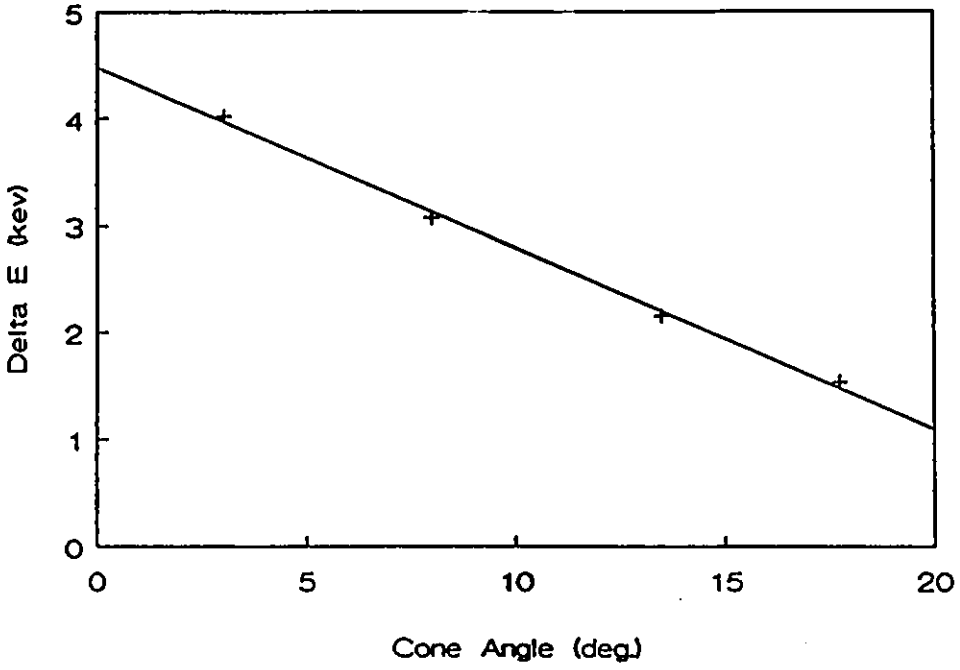

Figure 4.9 Illustrating the separation of the coherent peak and the most energetic Compton scattered photon as function of cone angle. (Nominal scattering angle of 40^{o}.)

angle. Clearly, the smaller the cone angle the better the peak spectral resolution.

4.5 Bone phantoms

Bone simulating materials had to be found for the initial scattering studies. The scattering materials chosen were water and aqueous solutions of dipotassium hydrogen phosphate, K_2HPO_4, ranging in density up to $1.71 g/cm^3$. Dipotassium hydrogen phosphate solutions were chosen for the following reasons: i) they are frequently used as radiologically-bone-equivalent material in photon attenuation and scattering studies ii) the solutions are relatively easy to prepare and iii) the solutions guarantee homogeneity throughout the sample compared with solid mixtures.

4.5.1 The effective atomic number, Z_{eff}, of K_2HPO_4 solutions

A compound may be regarded as a single element with an effective atomic number, Z_{eff}, given by (Fricke et al., 1935; Mayneord, 1937 and Spiers, 1946)

$$Z_{eff} = (\Sigma_i \alpha_i Z_i^{B-1})^{1/B-1} \qquad (4.4)$$

The effective atomic number is obtainable from the sum of the constituent elemental atomic numbers Z_i, raised to the power (B-1) and weighted according to their fractional electronic, content α_i, within the compound. The fractional

electronic content is given by:

$$\alpha_i = \frac{w_i}{q}\left(N_o \frac{Z_i}{A_i}\right) \tag{4.5}$$

where w_i is the fraction by weight of the ith element of atomic weight A_i and atomic number Z_i and q is the number of electrons per gram of the compound. In other words q is given by:

$$q = \Sigma w_i N_o \left(\frac{Z_i}{A_i}\right) \tag{4.6}$$

where N_o is Avogadro's number.

The exponent B in equation 4.4 is obtained from a power fit of the dependence of a given interaction cross-section upon atomic number. For example, the cross-section for coherent scattering σ_{coh} can be written as:

$$\sigma_{coh} = AZ^B \tag{4.7}$$

where A is a constant and B is the required exponent. The exponent varies, not only with the incident photon energy and type of interaction, but also with the elemental grouping, (that is the atomic number range) used in the power-fitting. Thus for the atomic number range $1 \leq Z \leq 25$, B is not the same as for the range $5 \leq Z \leq 15$. In general, the exponent B increases with energy. For bone, B increases by

about 11% from 10 keV to 150 keV.

Equation 4.4 was used to calculate the effective atomic number for water and aqueous K_2HPO_4 solutions of density ranging up to 1.7g/cm^3 for primary photons of energy 103 keV. Selected densities and their associated effective atomic numbers are tabulated in table 4.1. Figure 4.10 is a plot of calculated effective atomic number against density. The relationship is linear with r^2=0.99.

4.5.2 Derived differential coherent cross-sections for bone substitute materials

For an element of atomic number Z, the differential coherent cross-section $\sigma_{coh}(\theta)$ is given by:

$$\sigma_{coh}(\theta) = \frac{d\sigma_{coh}(\theta)}{d\Omega} = \frac{1}{2} r_e^2 (1+\cos^2\theta) [F(x,Z)]^2 \qquad (4.8)$$

where r_e is the classical electron radius, θ is the scattering angle, F(x,Z) is the atomic form factor and x is the momentum transfer defined in equation 2.20. For a mixture of elements, the differential linear attenuation coefficient for coherent scattering, $\mu_{coh}(\theta)$ is given by:

$$\mu_{coh}(\theta) = \rho N_o \Sigma_i \frac{w_i}{A_i} [- \frac{d\sigma_{coh}(\theta)}{d\Omega}]_i \qquad (4.9)$$

where w_i is the fraction by weight of the ith element of

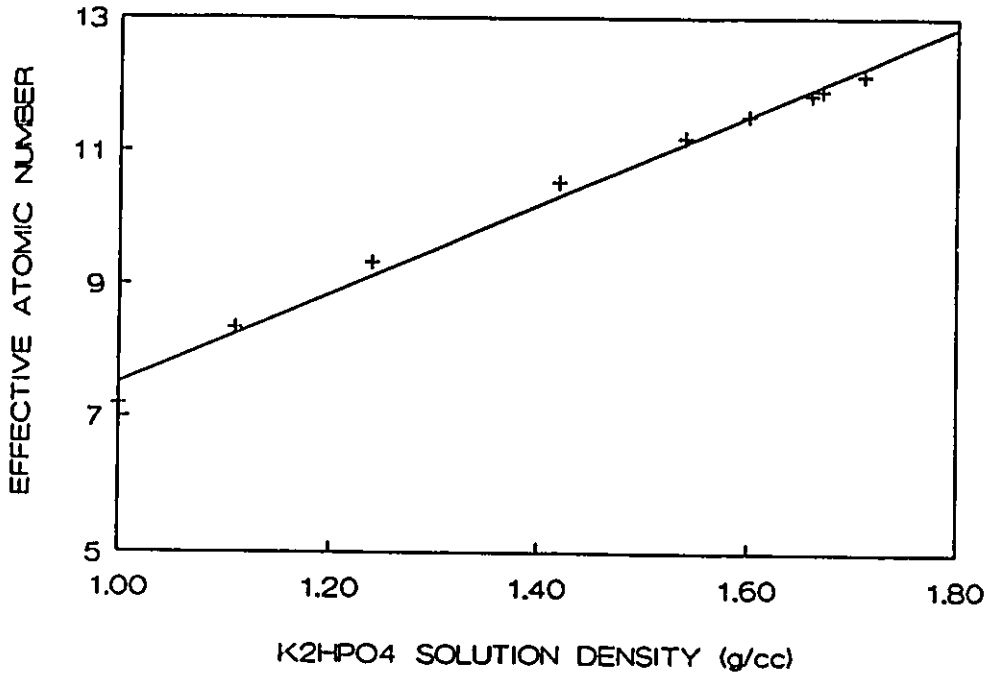

Figure 4.10 The variation of solution effective atomic number with solution density

atomic weight A_i and N_o is Avogadro's number. The quantity $\mu_{coh}(\theta)$ has units of cm^{-1} $ster^{-1}$ since it is the probability of a photon being coherently scattered at an angle θ, per unit length of beam path within the solution of density ρ. The differential coherent linear attenuation at selected angles was calculated for selected densities of K_2HPO_4 solutions using equation 4.7 and form factor data from Hubell et al., 1979. The normalised differential coherent linear attenuation coefficients, obtained by dividing the differential linear attenuation of a given solution density by that for water at the same scattering angle, were plotted against solution density. The graph in figure 4.11 indicates that as the angle of scatter increases, the change in normalised differential coherent linear attenuation coefficient per unit change in solution density also increases.

4.6 Measurements

As has already been indicated in section 4.2, water and aqueous solutions of K_2HPO_4 of varying effective atomic number were put into 50 mm diameter polyethylene containers. They were in turn positioned with care being taken to confine the scattering volume within the solution. The coherent count rate was measured as a function of scattering angle and solution effective atomic number and/or density.

Table 4.1 K_2HPO_4 solution densities and their associated effective atomic numbers

Solution density ρ (g/cm^3)	Effective atomic number (Z_{eff}) for $h\nu$=103 keV
100 (water)	7.10
1.11	8.34
1.24	9.32
1.42	10.52
1.54	11.20
1.60	11.52
1.66	11.84
1.67	11.91
1.71	12.14

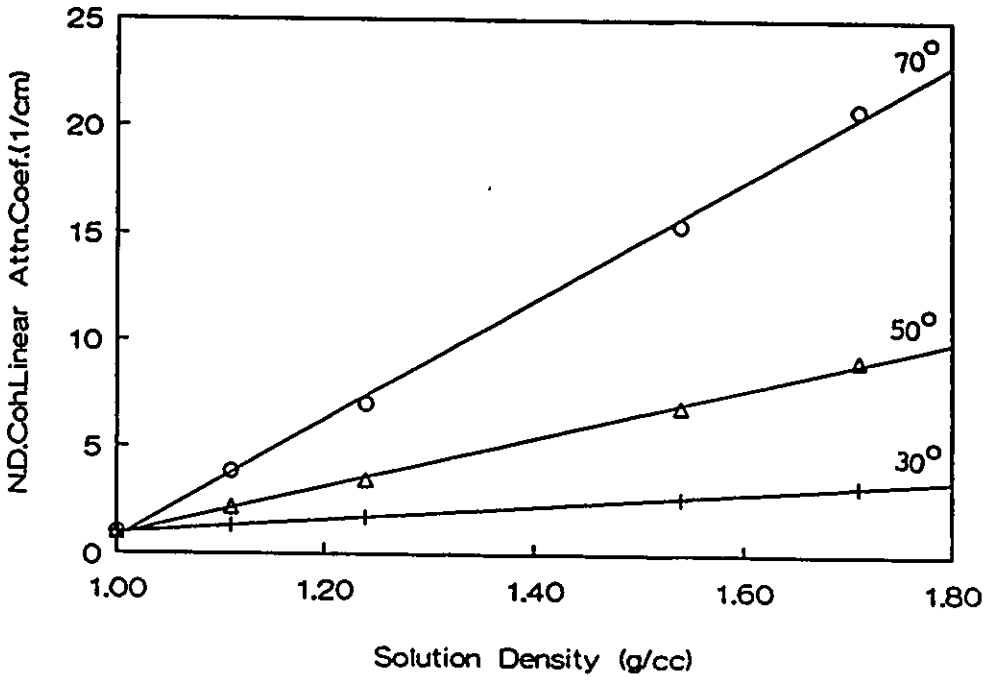

Figure 4.11 The variation of the calculated normalised differential linear coefficient for coherent scattering with solution density at selected scattering angles.

4.7 Results

The normalised count rate is the quotient of the scatter count rate for a given solution density divided by the scatter count rate for water in the same geometry. Normalised count rates for each K_2HPO_4 solution at scattering angles of 30, 40, 50 and 70 degrees are presented in table 4.2. They are also shown in figure 4.12 as functions of the effective atomic number of each solution. The data for each scattering angle were fitted to a straight line by linear regression analysis and the slopes and coefficients of determination r^2, are given in table 4.2

Figure 4.12 shows the increasing slope of the normalised count rate versus effective atomic number as the scattering angle increases. This confirms expectations from the normalised linear differential coherent coefficients plotted in figure 4.11. The change in the slope as a function of scatter angle is related to the fact that during the scattering process, the momentum transfer changes with angle. It is higher at larger angles when the inner electrons which have higher binding energies, contribute most to the process. On the other hand, at small scattering angles, just the outer electrons participate (Karellas, 1983; Compton, 1935; Kissel, 1978; Roy, 1968).

A more detailed study of the effect of scattering angle was made for the most dense solution, 1.71 g/cm^3 and

Table 4.2 Normalised count rates as a function of Z_{eff} of K_2HPO_4 solutions

Z_{eff}	Normalised count rates at these chosen scatter angles			
	θ=30	θ=40	θ=50	θ=70
7.10	1.00	1.00	1.00	1.00
8.34	1.38	1.57	2.07	3.99
9.32	1.68	2.07	3.00	6.28
11.20	2.11	2.95	4.53	11.16
12.14	2.24	3.49	5.22	12.94
slope	0.247±.017	0.491±.009	0.841±.017	2.406±.050
r_2	0.9862	0.9991	0.9987	0.9987

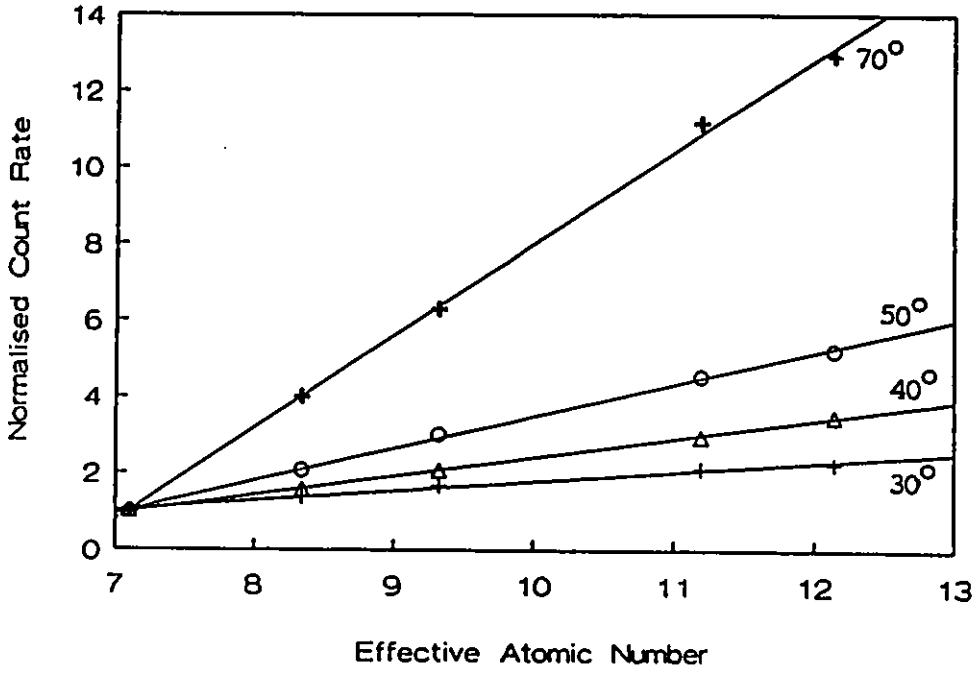

Figure 4.12. Normalised coherent count rate as a function of the solution effective atomic number at various scattering angles.

Table 4.3 Data for K_2HPO_4 solution (Z_{eff}=12.14)

Scattering angle θ(degrees)	Scattering Volume V(cc)	Count rate R(c/min)	Count rate /volume R_V
15	5.35	12547	2345.2
20	4.21	5783	1373.6
25	3.51	3003	855.6
30	3.03	1754	578.9
40	2.38	629	264.3
50	2.01	308	153.2
61	1.79	150	84.8
70	1.65	92	55.8
78	1.59	57	35.9

effective atomic number 12.14. The results are shown in table 4.3. The count rate falls by two orders of magnitude between scattering angles of 20 and 78 degrees. When the count rate, R, was plotted as a function of scattering angle, the power curve shown in figure 4.13 is obtained. The fitted curve is of the form

$$R = A\theta^{-b} \qquad (4.10)$$

The values of A and b were 1.1×10^5 and 3.3±0.1 respectively. The coefficient of determination, r^2, was 0.997.

It is implicit in the relationship between count rate and scatter angle that the count rate is also a function of the scattering volume. Experimentally, from the results of table 4.3 it was determined that for a fixed beam divergence the count rate, R, is proportional to the volume raised approximately to the fourth power, that is:

$$R \propto vol^{4.12} \qquad (4.11)$$

with a coefficient of determination r^2 of 0.98. The scattering volume used in equation 4.11 was determined using the programme in Appendix 2.

As indicated by equation 4.1 and shown in figure 4.5, the scattering volume varies with scatter angle. The volume dependence of the count rate implicit in equation 4.10 can be removed by obtaining a count rate normalised by volume. When the count rate per unit volume, R_v is plotted as a function of angle, the power curve shown in figure 4.14 is

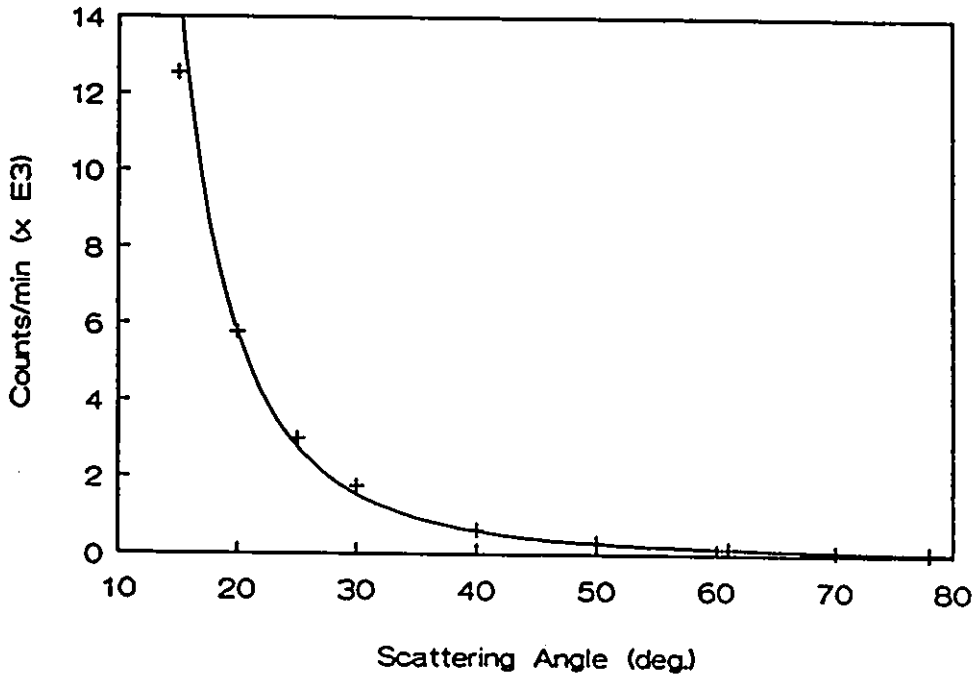

Figure 4.13 Coherent count rates as a function of scattering angle for a K2HPO4 aqueous solution of effective atomic number 12.14

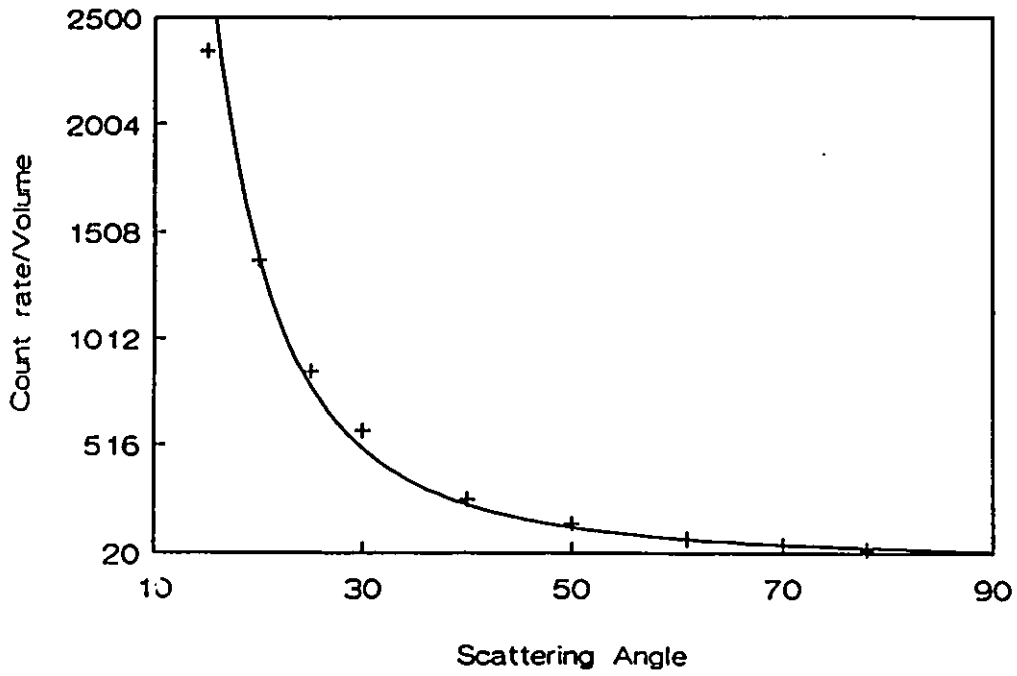

Figure 4.14 The variation of count rate per unit volume with scattering angle for a solution of effective atomic number 12.14.

obtained and the equation is

$$R_v = \text{const.}\ \theta^{-n} \qquad (4.12)$$

where n = 2.59±0.06 and the coefficient of determination is 0.99. This relationship was further validated by plotting the differential coherent cross section, $\sigma_{coh}(\theta)$, for photons of 103 keV and for an element of atomic number 12 (close to the effective atomic number of 12.14 for the aqueous K_2HPO_4 solution used) as a function of scattering angle, in the same range of angles range as for the count rate measurements. The plot, performed using data from table 4.4, is shown in figure 4.15. Its fitted power curve is of the form

$$\sigma_{coh}(\theta) = \text{constant}\ .\ \theta^{-2.68} \qquad (4.13)$$

with a coefficient of determination of 0.98. The agreement with equation 4.12 is evident. The atomic form factor data used to calculate the differential cross sections was obtained from tables of Hubbell et al. (1975).

4.8 Summary

The coherent count rate R obeys a power function relationship with scatter angle, θ and with scatter volume V. For the scatter angles examined, the following expressions have been observed.

Table 4.4 Differential coherent cross section for 103 keV photons for element Z=12, vs scattering angle (from Hubbell et al., 1975)

Scatter angle θ	$\sigma_{coh}(\theta)$ (barns/atm/str) x 10^{-2}
10	77.34
20	15.46
30	7.62
40	3.66
50	1.52
60	0.77
70	0.34

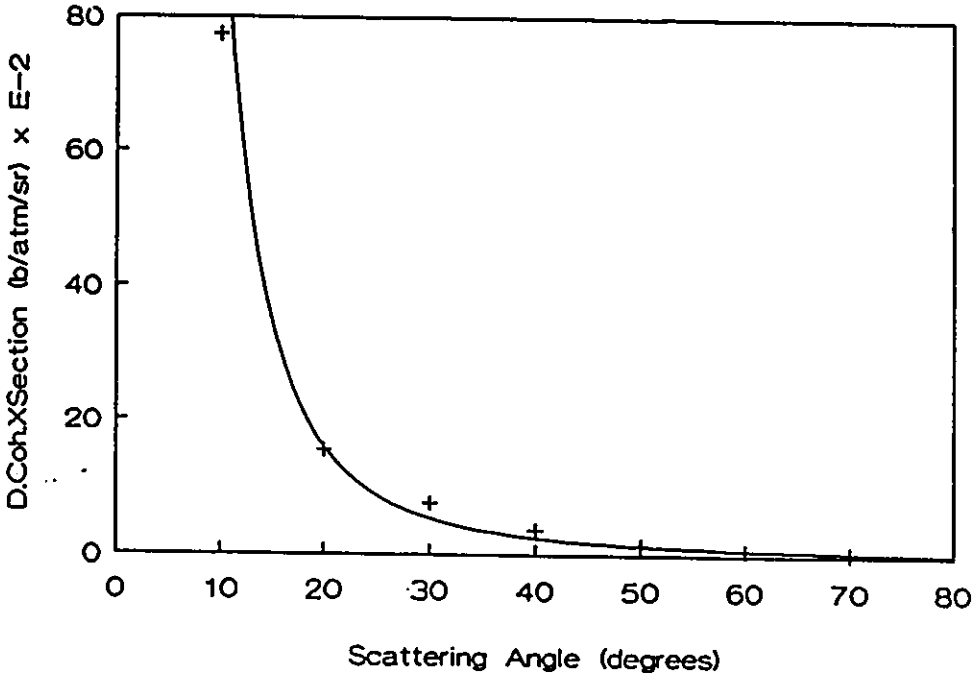

Figure 4.15 The variation of the differential coherent cross section with scattering angle for an element of atomic number 12.

$$R = A_1\theta^{-b} \quad (a)$$
$$R = A_2V^{m} \quad (b) \qquad (4.14)$$
$$R = A_3\theta^{-n} \quad (c)$$

The normalised count rate increases linearly with effective atomic number and scatter angle.

Sensitivity can be defined as the ability to detect small changes; in this case, changes in effective atomic number. It can be described as the slope of the curve which characterises the variation of the normalised coherent count rate with the effective atomic number of the aqueous K_2HPO_4 solutions. It is evident that the slope, hence the sensitivity, increases with scattering angle. Unfortunately the coherent count rate falls with increasing scatter angle and for a given acceptable preset counting time the statistical uncertainty also deteriorates.

4.9 Conclusion

The choice of small scatter angles and low photon energies gives desirably high coherent count rates but results in poor spectral separation between coherent and Compton peaks, high attenuation of the coherent photons, high absorbed dose to bone and relatively low sensitivity. If the intended measurement site is a small trabecular bone like the calcaneus, small scatter angles have an additional disadvantage in that asymmetrical scatter volumes are

produced which cannot be contained totally within the desired anatomical region.

A compromise has to be achieved between adequate counting statistics, attenuation losses (especially at low primary photon energies), dose to patient, peak spectral resolution and sensitivity. In Chapter 3 it was established that using the planar high purity germanium detector and with due regard to dose to the patient and energy resolution, the ideal primary photon energy is about 100 keV. With respect to the peak spectral resolution, sensitivity and optimum calcaneus scattering volume, a scatter angle of about 40 degrees is a satisfactory compromise, provided beam divergence is 10% or less.

CHAPTER 5

ATTENUATION CORRECTION

5.1 Introduction

Corrections have to be made for the attenuation of both the incident photons before they are scattered and of coherently scattered photons before they are detected. The measurement will then be independent of the thickness and attenuation properties of the tissues surrounding the scattering volume.

5.2 Basis for the attenuation correction procedure

The rationale employed was to explore whether the quotient of the coherent signal at a given scattering angle and the transmitted signal could be used to remove the effect of attenuation. This approach was successfully used in the development of a Compton Scattering bone densitometer (Webber and Kennett, 1976) and has been suggested by Mossop et al., (1987)

Figure 5.1 is a diagram of a non-symmetrical object with source in position 1. The transmission count rate T_1, and the coherent count rate, S_1, at angle θ can be measured. Moving the source through angle θ to position 2 the transmission count rate is now T_2 and the coherent count

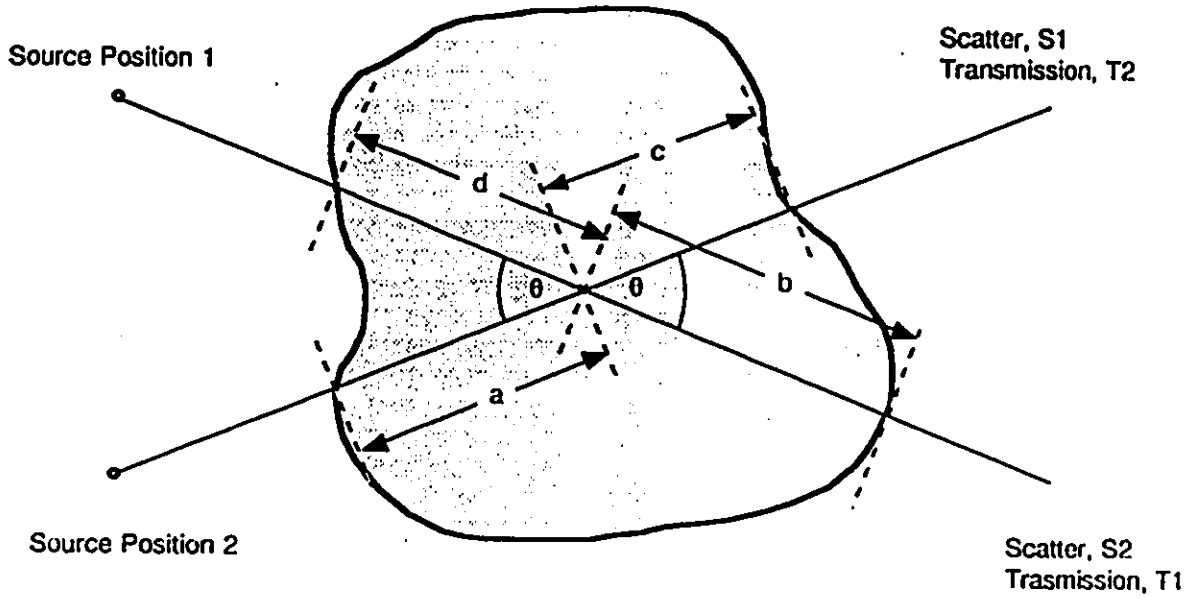

Figure 5.1 Illustrating the basis for attenuation correction.

rate is S_2. Approximate expressions for the count rates S_1,T_1, $S_2$and T_2 can be written as follows:

$$S_1 \propto I_o \exp(-\mu_i d) \cdot \exp(-\mu_i c) \quad (5.1)$$

$$S_2 \propto I_o \exp(-\mu_i a) \cdot \exp(-\mu_i b) \quad (5.2)$$

$$T_1 \propto I_o \exp(-\mu_i d) \cdot \exp(-\mu_i b) \quad (5.3)$$

$$T_2 \propto I_o \exp(-\mu_i a) \cdot \exp(-\mu_i c) \quad (5.4)$$

where I_o is the incident photon intensity, μ_i is the total attenuation coefficient for both incident and coherently scattered photons and the distances a, b, c and d are as indicated in figure 5.1

The ratio of the product of the scattered intensities to the product of the transmitted intensities is independent of the distances a, b, c and d. That is

$$\left(\frac{S_1 S_2}{T_1 T_2}\right)^{1/2} = K \quad (5.5)$$

The factor K is hereafter called the scattering ratio.

While this ratio may satisfactorily correct for attenuation in the case of line photon beams, the cancellation is not exact for a finite scattering volume. Furthermore, the volumes for the scattering and transmission measurements are not identical. Despite these potential sources of error, practical experience with a Compton scattering densitometer (Webber and Kennett, 1976; Kennett

and Webber, 1976) indicated that in that system, the effects of finite geometry on the scattering ratio were of the order or one percent of less. It seems likely therefore, that the scattering ratio is independent of attenuation and yet depends on the coherent scattering cross section.

For symmetrical objects, for example cylindrical objects in which the point of intersection coincides with the centre of the object, distances a, b, c and d are equal to the radius of the object. Consequently in practice only one scattered and one transmitted measurement are required and the scattering ratio becomes:

$$K = \frac{S}{T} \qquad (5.6)$$

5.3 Modelling the coherent/transmission ratio

If the attenuation procedure is valid, the scattering ratio should be independent of the size of the solution container size and should increase with the effective atomic number of the solution. To test these assumptions a simulation was performed for K_2HPO_4 aqueous solutions of effective atomic number ranging from 7.10 (water) to 10.52 within containers of diameter ranging from 38 mm to 73 mm.

The approach adopted for the simulation is an adaptation and extension of the method used to determine the scattering volume. Details of that method are given in

Appendix 2. Once the scattering volume is determined, points are generated randomly within it in order to determine the mean cross section per atom per photon, $\langle\sigma\rangle$. The product of $\langle\sigma\rangle$ and the number of photons in the scattering volume gives a "probability" a photon being coherently scattered at a given scattering angle, θ, and is:

$$P_S(\theta) = nV \langle\sigma\rangle \qquad (5.7)$$

where n is the number of atoms per unit volume for a solution of a given physical density; V is the scattering volume. $\langle\sigma\rangle$ is given by the expression

$$\langle\sigma\rangle = \frac{\int_V \phi(V) \frac{d\sigma(\theta)}{d\Omega} e^{-\mu\ell} . d\Omega.DR.dV}{V} \qquad (5.8)$$

where $\phi(V)$ is the photon flux density, which in general is a function of position within the scattering volume. For uniform (constant) flux density, $\phi(V)$ is simply ϕ and can be approximated as the inverse of the beam area for unit flux at the centre of rotation; ℓ is the attenuation path length measured from the photon source through the scattering point and to the detector face, μ is the total linear attenuation coefficient at the incident photon energy and for the given solution density: $d\Omega$ is the solid angle subtended by the detector and DR is the detector response profile across the detector face; $d\sigma(\theta)/d\Omega$ is the differential coherent cross

section. This cross section is given by the expression, $1/2r_e^2(1+\cos^2\theta)FF_{eff}^2$, where r_e is the classical electron radius, θ is the scattering angle and FF_{eff}^2 is the square of the effective form factor for the average scattering atom in the solution. It is given by the expression:

$$FF_{eff}^2 = \frac{\Sigma n_i FF_i^2}{\Sigma n_i} \tag{5.9}$$

where n_i is the number of atoms of element i per unit volume of solution and FF_i is the form factor for element i.

For constant photon flux, equation 5.7 can be re-written as:

$$P_s(\theta) = nV\phi < \frac{d\sigma(\theta)}{d\Omega} e^{-\mu\ell} d\Omega.DR>$$

$$= \frac{nV\phi \sum_{i=1}^{N} (\frac{d\sigma(\theta)}{d\Omega} e^{-\mu\ell} d\Omega DR)}{N} \tag{5.7a}$$

where N is the number of scattering points in the scattering volume.

For a varying flux, the probability of scatter can be written as

$$P_s(\theta) = \frac{nV \sum_{i=1}^{N} (\frac{d\sigma(\theta)}{d\Omega} e^{-\mu\ell} d\Omega.\phi.DR)}{\sum_{i=1}^{N} \phi} \tag{5.7b}$$

The transmission probability is obtained as a product

of the average attenuation probability, $\langle e^{-\mu\ell} \rangle$, and the fraction of the flux, $P(\alpha_1)$, that hits the detector. Both these factors are discussed in Appendix 3. The transmission probability can therefore be written as:

$$P_t = \langle e^{-\mu\ell} \rangle \; P(\alpha_1) \qquad (5.11)$$

where ℓ has the same definition as in equation 5.8 and α is given by the expression:

$$\alpha_1 = \tan^{-1} \left[\frac{\text{detector collimator radius}}{R_1 + R_2} \right] \qquad (5.12)$$

R_1 and R_2 are the cone apex-to-point-of-intersection distances given in figure 4.3

The probability of scatter divided by the probability of transmission gives the scatter ratio. In order to determine whether the size of the container had any effect on the scatter ratios, the scatter ratios for water and all solutions of effective atomic number up to 10.52 were normalised to the values for the smallest container. The results of the simulation are given in table 5.1 and show that size effects are unimportant. The graph of figure 5.2 is a plot of the data in table 5.1 and demonstrates the null effect of container size. The error bars are standard deviations.

Table 5.1 Simulated coherent/transmission scatter ratio at various solution effective atomic numbers and container diameters

Solution Effective Atomic number (Z_{eff})	Container diameter (cm)	Scatter ratio normalised to smallest diameter value
7.10	3.84	1.00 ± 0.05
7.10	5.00	0.98
7.10	6.00	1.00
7.10	7.28	0.96
8.34	3.84	1.00
8.34	5.00	1.09
8.34	6.00	1.03
8.34	7.28	1.07
9.32	3.84	1.00
9.32	5.00	1.01
9.32	6.00	0.97
9.32	7.28	0.97
10.52	3.84	1.00
10.52	5.00	0.97
10.52	6.00	1.01
10.52	7.28	1.04

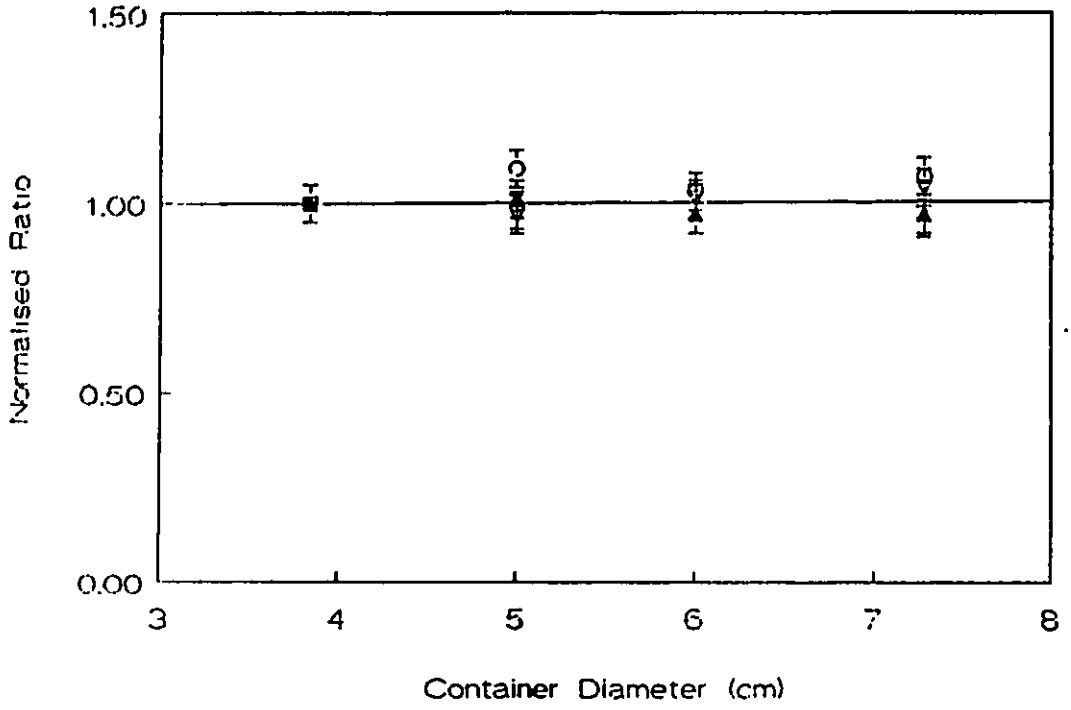

Figure 5.2 The simulated coherent/transmission ratios relative to the value for the smallest container diameter for solutions of effective atomic numbers 7.10 (+),8.34 (O),9.32 (△) and 10.52 (▽).

5.4 Measurements

Measurements were performed to confirm the simulation results. The experimental setup was as shown in Chapter 4 and the angle of scatter was 40^{o}. Various aqueous solutions of dipotassium hydrogen phosphate with effective atomic numbers in the range 7.10 (water) to 12.14, were put into polyethylene cylindrical containers with diameters in the range 3.8 cm to 7.3 cm. Each solution, as well as distilled, de-ionised water in the same sized container, was placed in turn, at the mutual axis of rotation of the source and detector. A transmission and a scatter (40^{o}) measurement were made, first keeping the container diameter constant while varying the solution effective atomic number and then keeping the solution effective atomic number constant while varying the container diameter. The measurements were first performed using the tantalum multibore collimator inserts and were repeated using the lead 5 mm diameter single bore collimator inserts.

5.5 Results

5.5.1 Container size effects

In order to determine whether the size of the container had any effects, coherent transmission ratios were measured as indicated above for K_2HPO_4 solutions in different sized containers. As in the simulation study, the

ratios were normalized to the value for the smallest container. The results are shown in table 5.2. Figure 5.3 is a plot of the normalised ratios as a function of container diameter and solution effective atomic number. For object dimensions up to 7.3 cm and for effective atomic numbers up to 10.52, there is no discernible effect of sample size on the scatter ratios.

It was stated in Chapter 1 that the ratio of the coherent and Compton scattered intensities has been used as an indicator of bone mineral status. The disadvantage of the coherent/Compton technique have been discussed in that chapter and they include the problems of multiple Compton scattering and differential attenuation of coherent and Compton scattered photons (Ling et al., 1982). However, since the Compton scattering data are simultaneously obtained with the coherent scattering data during the experiment, normalised coherent/Compton ratios were calculated in a similar manner to the coherent/transmission ratios of table 5.2. The results are given in table 5.3 and are plotted in figure 5.4. The coherent/Compton ratios are also unaffected by increases in container diameter, at least for diameters up to about 7 cm and for solution effective atomic numbers up to 10.52.

Table 5.2 Coherent/Transmission Ratios at various solution effective atomic numbers and container diameters

Z_{eff}	Container diameter (cm)	Coherent/Trans ratio normalised to smallest container diameter Experiment
7.10	3.84	1.00 ± .10
7.10	5.00	1.01
7.10	6.00	1.09
7.10	7.28	1.07
8.34	3.84	1.00
8.34	5.00	1.10
8.34	6.00	1.06
8.34	7.28	1.04
9.32	3.84	1.00
9.32	5.00	1.09
9.32	6.00	1.12
9.32	7.28	1.05
10.52	3.84	1.00
10.52	5.00	0.99
10.52	6.00	1.05
10.52	7.28	1.03

Table 5.3 Coherent/Compton ratios at various solution effective atomic numbers and container diameters

Solution Z_{eff}	Container diameter (cm)	Coherent/Compton ratio normalised to smallest container diameter
7.10	3.84	1.00 ± 0.06
7.10	5.00	1.02
7.10	6.00	0.91
7.10	7.28	1.00
8.34	3.84	1.00
8.34	5.00	1.01
8.34	6.00	1.01
8.34	7.28	0.98
9.32	3.84	1.00
9.32	5.00	1.05
9.32	6.00	1.02
9.32	7.28	1.01
10.52	3.84	1.00
10.52	5.00	1.01
10.52	6.00	1.01
10.52	7.28	1.00

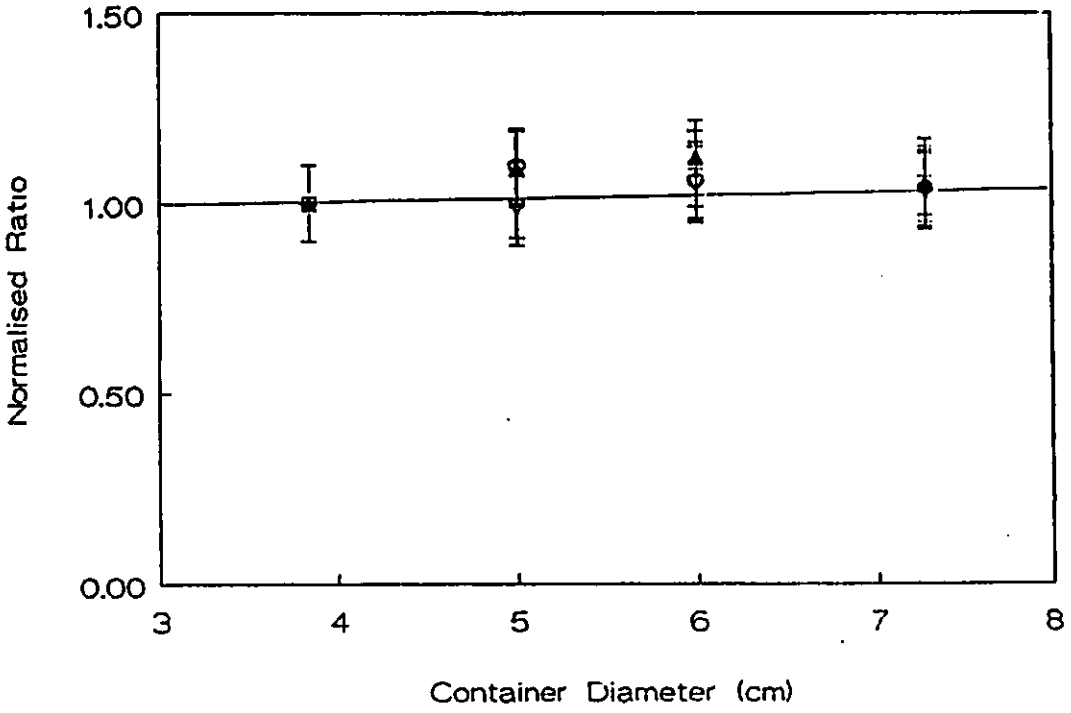

Figure 5.3 The measured coherent/transmission ratios relative to that of the smallest container for solutions of effective atomic numbers 7.10 (+), 8.34 (0), 9.32 (▲) and 10.53 (▽).

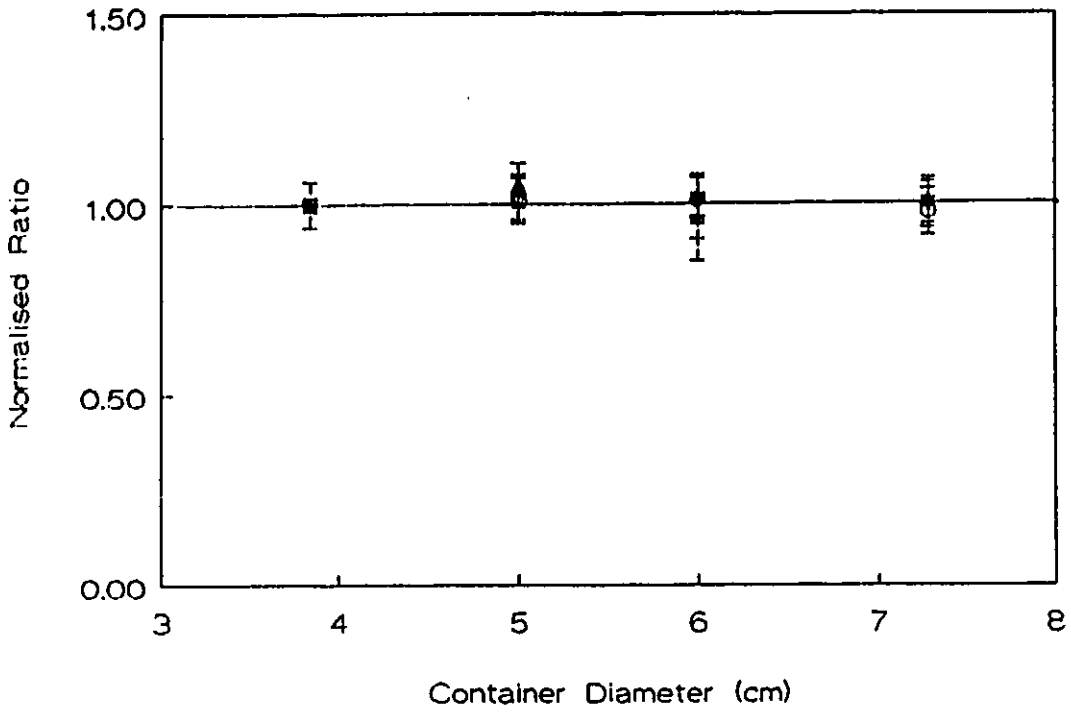

Figure 5.4 The measured coherent/Compton ratios relative to the value for the smallest container diameter for solutions of effective atomic numbers 7.10 (+),8.34 (O),9.32 (△) and 10.52 (▽).

5.5.2 Effective atomic number (Z_{eff}) effects

Once it had been established that container size effects were unimportant, the effects of solution effective atomic number, Z_{eff}, were investigated using containers 5 or 6 cm diameter. Ratios were normalised to water scatter ratios by dividing the coherent/transmission or coherent/Compton ratios at a given solution effective atomic number by their respective ratios for water in the same geometry. The results are presented in table 5.4 for the single bore lead collimators and in table 5.5 for the multibore tantalum collimators. These normalised ratios do not appear to be independent of collimator type as the tantalum collimator results are slightly higher than the lead collimator results.

Table 5.6 presents a comparison of the simulated and experimental normalised coherent/transmission scatter ratios for solution effective atomic numbers up to 10.52. In both the simulated and experimental results, the lead 5 mm diameter single bore collimator inserts were used. Overall the experimental values are about 15% higher than the simulated values. Despite an apparently steady deviation of experimental from simulated results the approach adopted in the attenuation procedure can be regarded as acceptable for the range of effective atomic numbers of interest.

Table 5.4 Normalised coherent/transmission and coherent/ Compton ratios for the lead 5 mm diameter single bore collimator

Z_{eff}	Container diameter (cm)	Normalised Ratios coherent/trans.	Coherent/Compton
7.10	5.00	1.00	1.00
8.34	5.00	1.60	1.46
9.32	5.00	2.35	1.95
10.52	5.00	3.46	2.57
11.20	5.00	4.12	2.89
11.52	5.00	4.39	3.04
12.14	5.00	5.39	3.38
7.10	6.00	1.00	1.00
8.34	6.00	1.65	1.47
9.32	6.00	2.30	1.93
10.52	6.00	3.50	2.50

Figure 5.5 is a plot of the normalised ratios of table 5.4 against solution effective atomic number. Both the coherent/ transmission and the coherent/Compton normalised ratios exhibit a power function relationship with effective atomic number. The relationship can be written as

$$NR = a_o Z_{eff}^{n} \qquad (5.13)$$

where NR is the normalised coherent/transmission or coherent/Compton ratio. For coherent/ transmission technique, the exponent, n, was determined to be 3.30±0.15 and for the coherent/Compton method n was found to be 2.38±0.08. The respective a_o values were 0.0016 and 0.0097. In both cases the coefficient of determination is 0.999. It is evident both from the graph of figure 5.5 and from the magnitudes of the power exponents, n, that the coherent/transmission technique is more sensitive to changes in effective atomic number than the coherent/Compton ratio.

5.6 Sensitivity

Sensitivity can be defined (section 4.8) as the ability to detect change. In a linear relationship, the slope can be used as an indicator of sensitivity. Since the coherent/Compton ratio has been used to quantitate bone mineral content (Ling et al., 1982), it is desirable to compare its sensitivity to that of the coherent/transmission

Table 5.5 Normalised coherent/transmission and coherent/Compton ratios for the Tantalum multibore collimator insert

Z_{eff}	Container diameter (cm)	Normalised Ratios coherent/trans.	Coherent/Compton
7.10	3.84	1.00	1.00
8.34	3.84	1.70	1.50
9.32	3.84	2.42	1.93
10.52	3.84	3.91	2.56
7.10	5.00	1.00	1.00
8.34	5.00	1.84	1.49
9.32	5.00	2.67	1.99
10.52	5.00	3.98	2.54
7.10	6.00	1.00	1.00
8.34	6.00	1.64	1.65
9.32	6.00	2.55	2.16
10.52	6.00	3.90	2.82
7.10	7.28	1.00	1.00
8.34	7.28	1.64	1.47
9.32	7.28	2.42	1.96
10.52	7.28	3.88	2.55

Table 5.6 Normalised coherent/transmission ratios. Comparison of experimental and simulated values

Z_{eff}	Normalised coherent/transmission ratios Experiment	Simulation
7.10	1.00	1.00
8.34	1.65	1.49
9.32	2.30	2.00
10.52	3.50	2.80

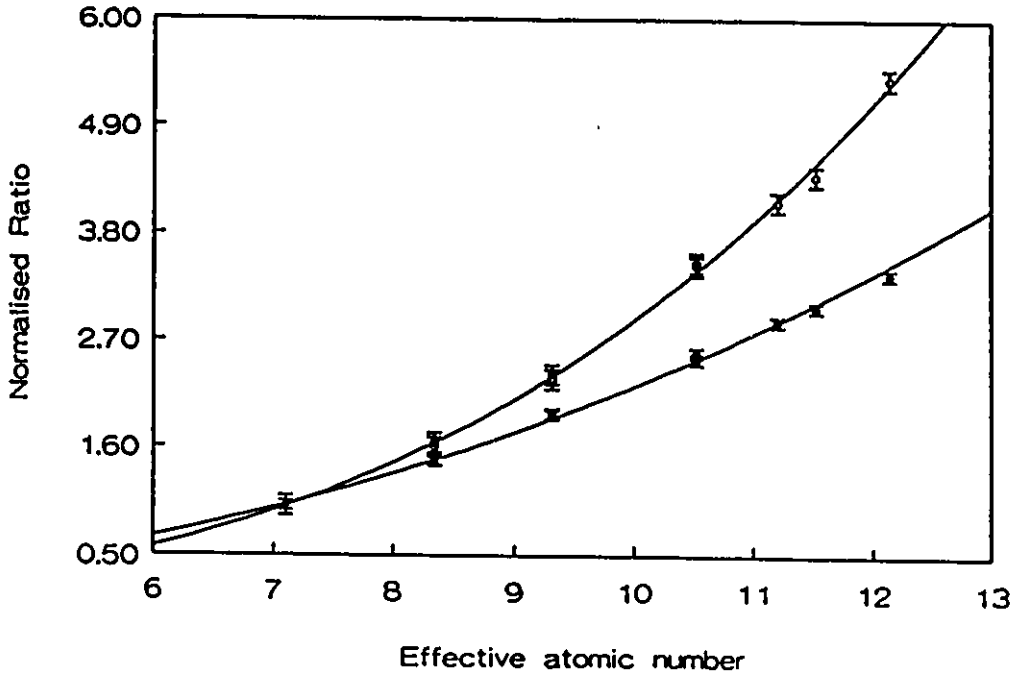

Figure 5.5 Variation of the normalised coherent/transmission (o) and the normalised coherent/Compton (•) ratios with solution effective atomic number.

technique. The variation of both coherent/ Compton and coherent/transmission normalised ratios with effective atomic number obeys a power law and makes a comparison of sensitivities rather complicated. If the upper limit for the effective atomic number is set at about 11.50 (corresponding to normal bone (White, 1977)) the relationship can, as shown in figure 5.6, be approximated to a linear function, with coefficients of determination of about 0.99. This facilitates the comparison. The sensitivities were compared using the formula:

$$S = \left(\frac{NR_2 - NR_1}{NR_1} \right) / \left(Z_{eff2} - Z_{eff1} \right) \quad x\ 100\% \qquad (5.14)$$

where S is the percentage increase in the signal, per unit change in effective atomic number, NR_2 and NR_1 are the high and low values of the normalised ratio and Z_{eff2} and Z_{eff1} are the effective atomic numbers corresponding to NR_2 and NR_1 respectively.

Using equation 5.14, the sensitivities obtained were:

$S_{(coherent/transmission)} = 5.8\%$ (i)

$S_{(coherent/Compton)} = 3.3\%$ (ii)

Dividing (i) by (ii) gives a factor of 1.8. This suggests that the coherent/transmission technique is almost twice as sensitive as the coherent/Compton technique. Despite the fact that the tantalum collimator signals are slightly

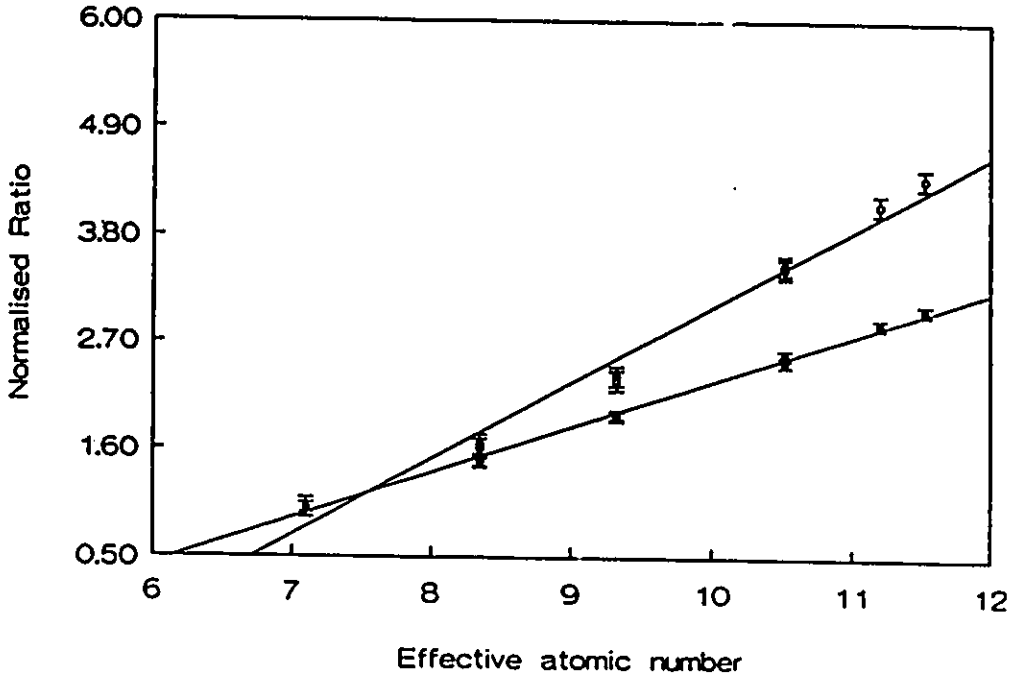

Figure 5.6 Comparison of the sensitivities of the coherent/transmission (o) and coherent/Compton (•) techniques.

higher than those of the lead single bore collimators, the relative increase in sensitivity between the two techniques is virtually unchanged.

5.7 Conclusion

The normalised simulated and experimental coherent/transmission ratios and also the normalised coherent/Compton ratios are independent of object dimensions. This demonstrates the adequacy of the attenuation correction procedure.

Both normalised ratios exhibit a power function relationship with increasing effective atomic number.

The sensitivity of the coherent/transmission technique is nearly twice that of the coherent/Compton method. Another advantage of the former technique over the latter is the fact that multiple coherent scattering is likely to be much lower than multiple Compton scattering (Bradley and Ghose, 1984). Furthermore, the coherent/transmission technique is not complicated by effects due to differential absorption of coherent and Compton scattered photons (Ling, et al., 1982).

CHAPTER 6

THE CALCANEUS AS A MEASUREMENT SITE

6.1 Anatomy of the Human Calcaneus

The bones of the foot which are shown in figure 6.1(a), fall into three groups: the tarsus, the metatarsus and the phalanges. The calcaneus, figure 6.1(b), is the largest of the tarsal bones. It is situated at the posterior part of the foot, forming the heel. It articulates with two bones, the talus proximally and the cuboid anteriorly. The calcaneus serves to transmit the weight of the body to the ground. The distal or planar surface of the calcaneus is bounded posteriorly by the calcaneal tuberosity, which is depressed in the middle and prolonged on either side. On the lateral side of the tuberosity there is a small but prominent lateral process. Medially there is a larger and broader medial process.

The lateral surface of the calcaneus is broad, subcutaneous and flat. It has a tubercle near its centre. The trochlea peronealis or peroneal tubercle is an elevated ridge that separates two oblique grooves marking a narrow surface anterior to the central lateral tubercle. The calcaneal medial surface is deeply concave. It serves to transmit planar vessels and nerves into the sole of the

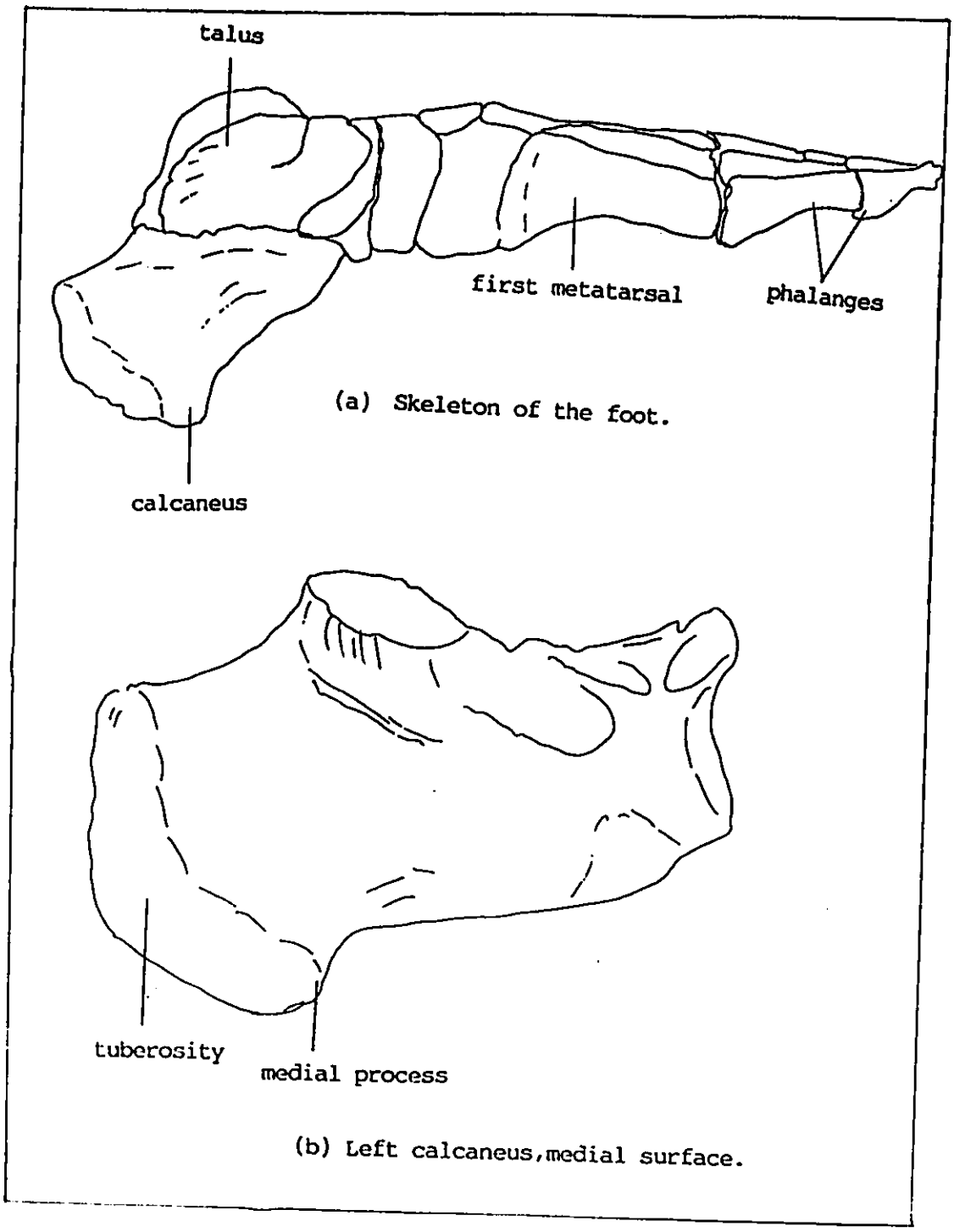

Figure 6.1 Bones of the Foot.

foot.

Figure 6.2 illustrates some of the measurable dimensions of the calcaneus. The maximal length is measured in projection along the major axis of the bone by the most projecting points, anteriorly and posteriorly. The minimal breadth is the transverse width. It is measured behind the posterior articular surface of the bone. The maximum posterior breadth, figure 6.2(a), is measured at the level of the two inferior tuberosities of the bone and the maximum anterior breadth is measured at the level of the sustentaculum tali. The minimal height is the vertical distance between the proximal and the distal calcaneal surfaces measured behind the posterior articular surface, perpendicular to the long axis. The hindmost part of the bone has a maximal posterior height. The calcaneal tubercles and adventitious tuberosities are not included when measuring the minimal height and the minimal breadth.

In adult humans, the average maximal length is 82±5 mm, the average minimum breadth is 28±3 mm and the average body height is 44±3 mm. The racial variation is minimal and the overlap between sexes is so great that sex determination from single values is not possible.

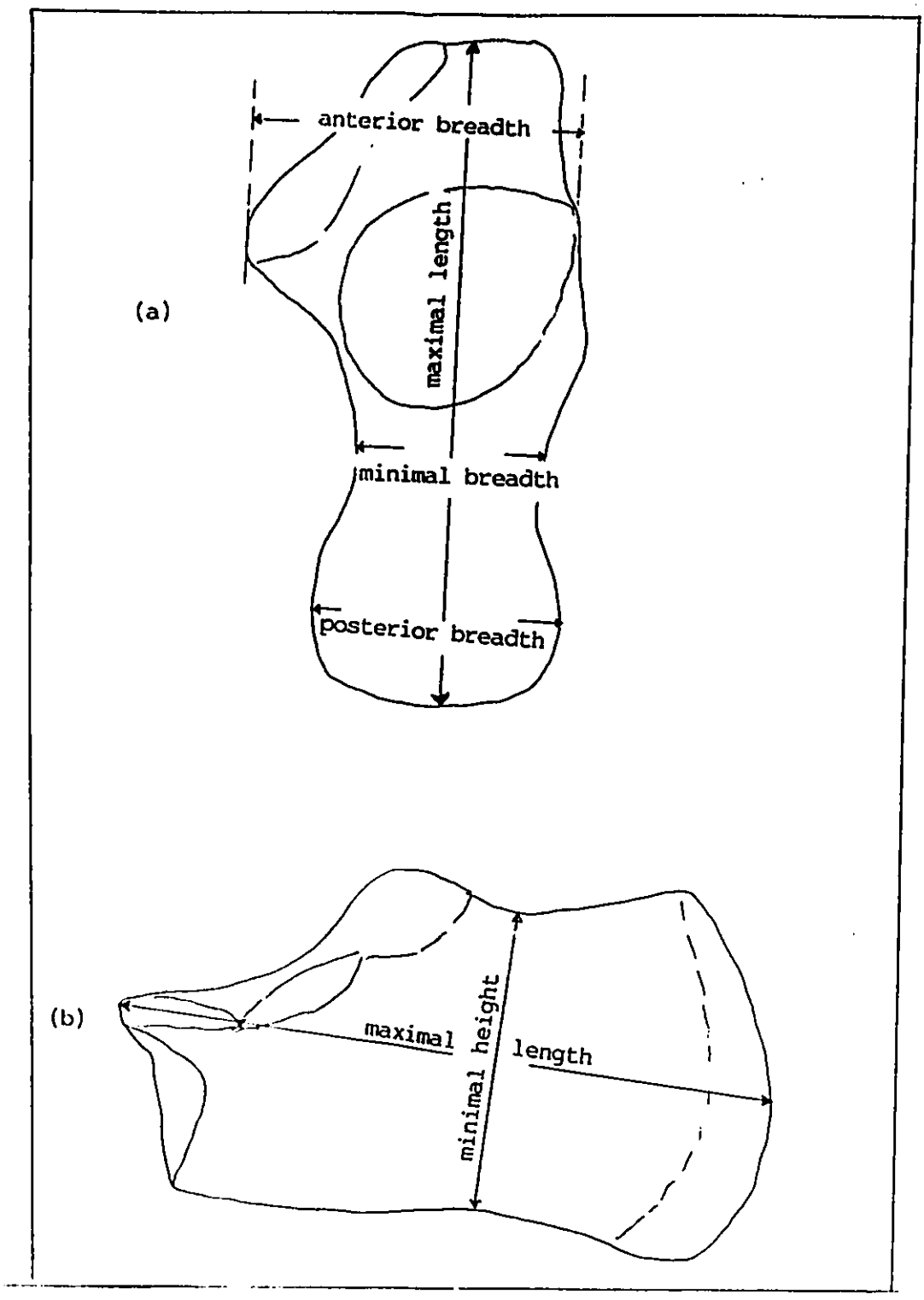

Figure 6.2 Measurements of the calcaneus.

6.2. Spatial distribution of mineral in the human calcaneus

The calcaneus is 90% trabecular bone. It is important to consider the distribution of mineral within the trabecular bone and the distribution of cortical bone. A qualitative assessment of mineral distribution is obtained from a lateral radiograph of the calcaneus. The radiograph of a mid-sagittal section through the calcaneus is shown in figure 6.3

The irregularity of the trabecular structure in the posterior half (right hand side) of the radiograph can be seen. Trabecular bone is mostly porous and is distributed unevenly within the calcaneus appearing as the fine, irregular white striations throughout the interior of the bone. The pores are occupied by yellow marrow. The compact cortical bone is seen as the white region restricted to the periphery of the calcaneus. Most of the cortical bone is distributed at the anterior and antero-superior third of the calcaneal bone, where is articulates with the talus. Immediately behind and below this very prominent cortical area is a relatively large dark (in the radiograph) region devoid of trabecular structure. When trabecular bone is depleted by aging or disease, yellow marrow expands to occupy the resultant void. From the radiograph, it is clear that most trabecular bone is in the posterior two thirds of the calcaneus in a region roughly demarcated by the lines

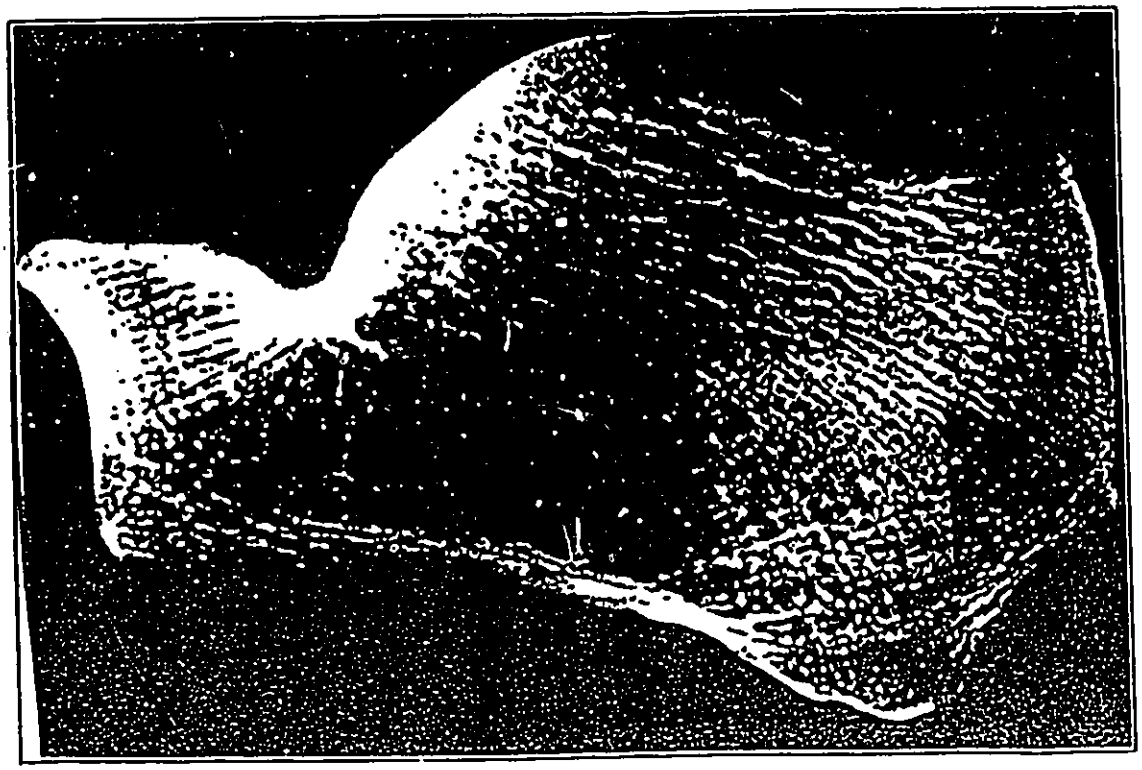

Figure 6.3 A copy of the x-ray radiograph through the mid-sagittal section through the human calcaneus. (Weaver and Chalmers 1966)

defining the minimal breadth, minimal height and the posterior tuberosity. In selecting a region in which to place the scattering volume it is, needless to say, prudent to avoid the region normally occupied by yellow marrow.

6 2.1 Measurement of the distribution

In order to investigate the internal distribution of bone mineral more closely and quantitatively, a representative sample was selected from a stock of 3 calcanei. These bones were carefully sliced antero-posteriorly, parallel to the major axis of the calcaneus as illustrated in figure 6.4. The slicing was done using a diamond saw in the Materials Science and Engineering Workshop. Each slice was about five millimetres thick. Mineral distribution in each of the slices was obtained by scanning each slice using a Single Photon Absorptiometry (Norland, 278-A) machine, in the direction parallel to the long axis, that is perpendicular to the minimum height. The photon source in this machine is ^{125}I (28 keV). The scan lines were about 5 mm apart.

The amount of bone mineral present in the bone slice path scanned is calculated from the attenuation of the photon beam as it passes through the slice, which rests in a water-filled plastic container. The count rate (intensity) profile of a typical scan path through water and bone is

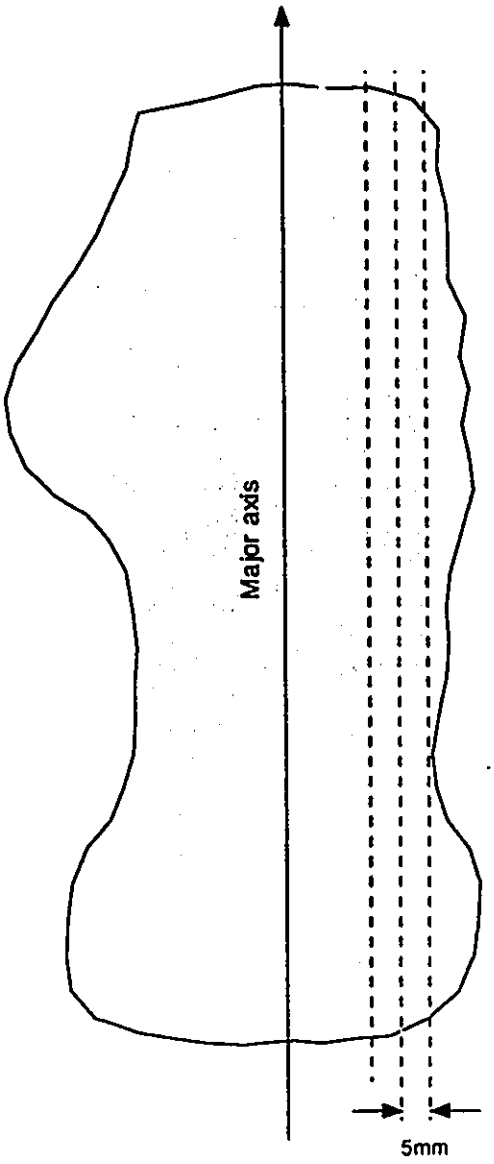

Figure 6.4 Illustrating the slicing of the calcaneus

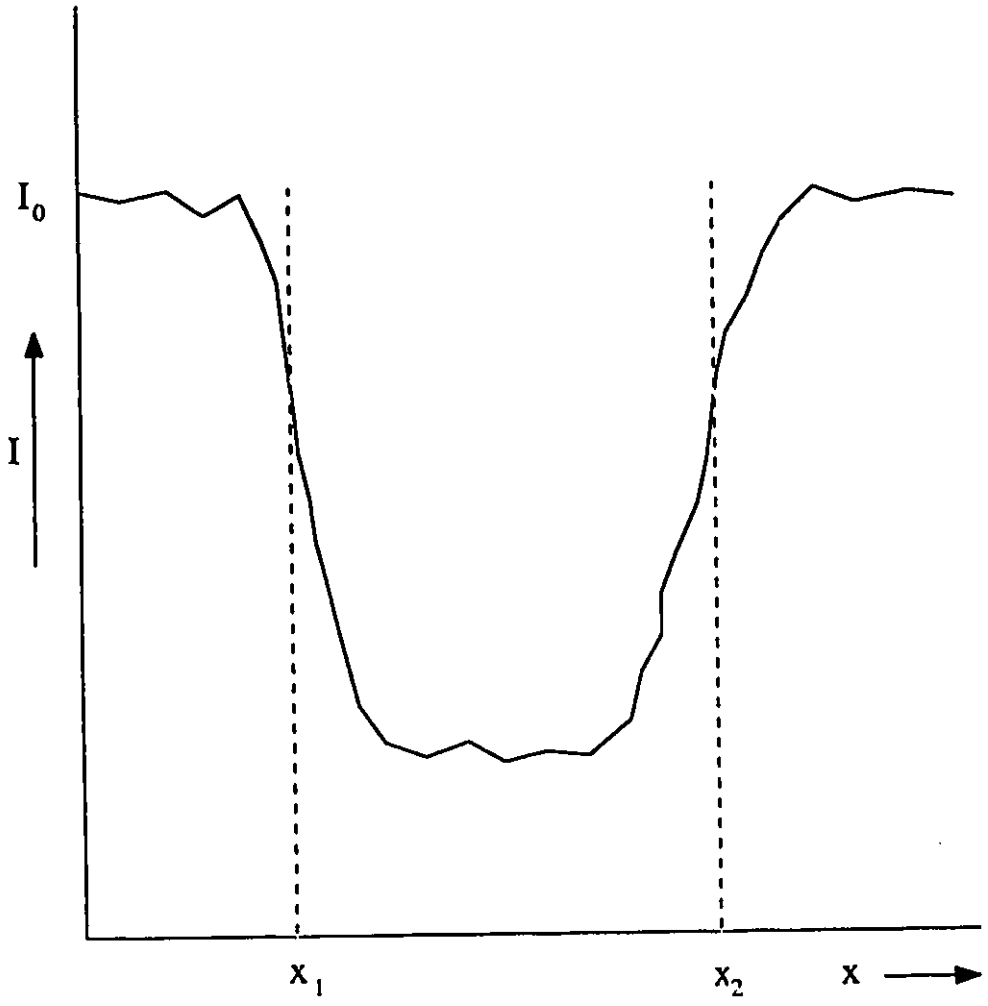

Figure 6.5 Illustrating a typical scan path profile through water (I_o) and bone and water (I).

depicted in figure 6.5, where the beam intensity at any point in the scan path in bone and water is I and the intensity at points in water alone is I_o. The bone edges are taken to be points where I is 70% of I_o, the baseline value.

The intensity profile of the scan can be stored in digital form. A cursor is provided to allow digital examination of the raw data. A Basic programme was written (courtesy of Mr. Kenrick Chin) to copy and transfer the data to a file which allowed for manipulation of the raw data. This programme is documented in Appendix 4. The spatial bone mineral distribution was obtained by plotting $\ell n(I_o/I)$ along a scan path. Several parallel paths of a single bone slice were combined to yield the mineral distribution illustrated in figure 6.6. Although this is just for one slice it is typical of the distributions of bone mineral obtained in each and every slice. In figure 6.6, the baseline is water (W), followed by cortical bone (c), trabecular bone (T), cortical bone again and finally by water. The relative amount of mineral in each component is indicated by the magnitude of $\ell n(I_o/I)$. It is once again clear from figure 6.6 that the distribution of cortical bone is peripheral.

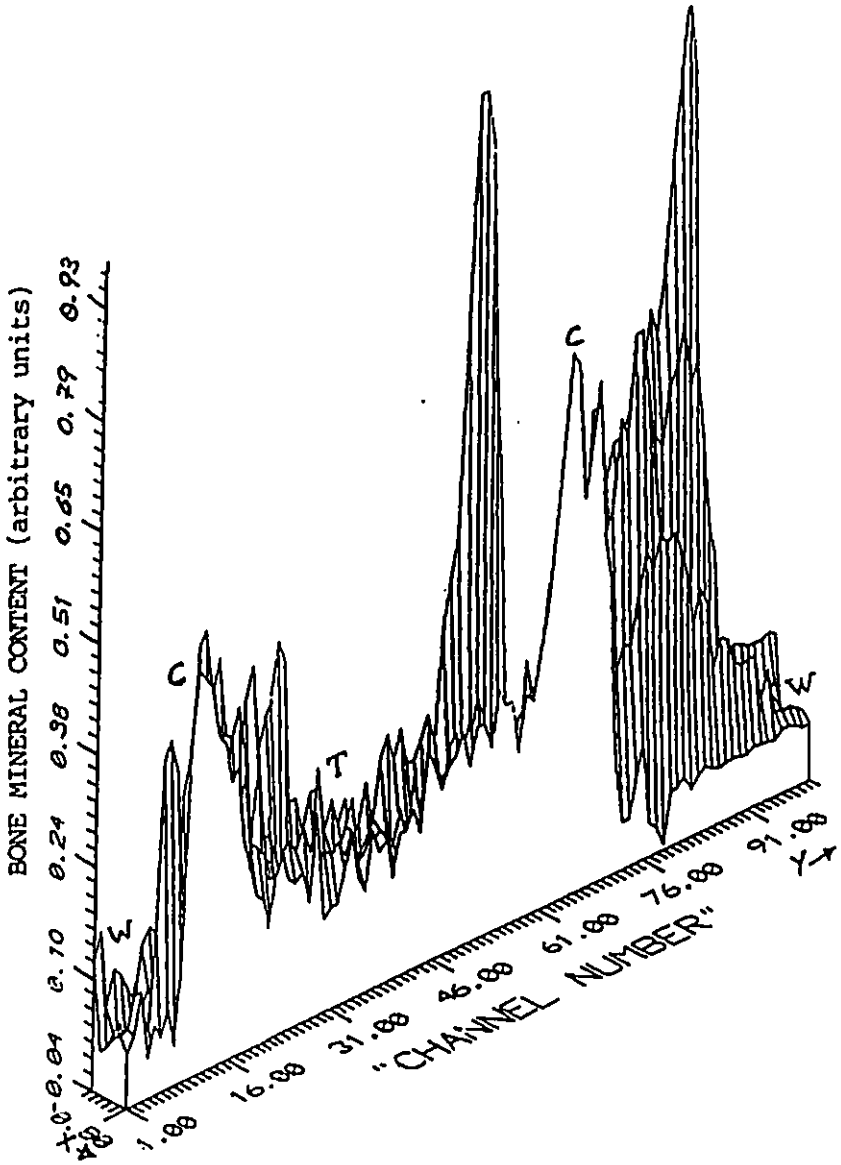

Figure 6.6 Illustrating the distribution of bone mineral in a slice of the calcaneus.

6.3. Why measure bone mineral in the calcaneus?

Trabecular bone mineral density is the mass of bone mineral (excluding organic bone material) per unit volume of trabecular bone. Bone mineral is directly related to bone strength (Carter and Hayes, 1976) which is in turn related to the ability of bone to resist fracture. Trabecular bone is known to undergo remodeling at a rate about eight times that of cortical bone (ICRP 23, 1974). Consequently changes in bone mineral density due to a variety of metabolic bone diseases (including osteoporosis) are first manifest in trabecular bone (Frost, 1966; Rasmussen and Bordier, 1974).

Since the calcaneus consists essentially of trabecular bone (Vogel et al., 1988) measurement of mineral density at this site could be useful for the diagnosis of early bone mineral loss and/or for monitoring response to therapy.

It is important to distinguish between physical density and trabecular bone mineral density. The former includes both mineral and organic components of trabecular bone tissue. It has been reported (Puumalainen et al., 1976) that for every 30% change in trabecular bone mineral density, the corresponding change in physical density is only about 10%. The reason for this anomaly is that during the bone remodeling process that results in mineral loss, the bone mineral resorbed is replaced by marrow in the

trabecular bone.

Studies by Wasnich et al., (1985), Yano et al., (1984), Vogel (1987) and Wilson (1977) have shown that the correlation coefficients of bone mineral concentration measured at one site to that measured at another site range from 0.61 to 0.95. The sites at which these studies were made were the radius, the calcaneus, the lumbar spine and three regions (the neck, intertrochanteric and Ward's triangle) of the proximal femur. The general conclusion was that there is substantial inter-correlation between the sites, with adjacent sites having the strongest correlation. It was also clear that precise mineral content at one site could not be predicted from measurement at another site. Spinal bone mineral content is as predictable from calcaneal bone mineral content (r=0.77) as lumbar L1 bone mineral content is from lumbar L4 bone mineral content (r=0.81) (Wilson, 1977). The correlation of the bone mineral content of one thoracic vertebra to another is variable, with the correlation coefficients ranging from 0.77 to 0.92. All bones lose mineral although not necessarily at the same rate nor with the same longitudinal profile. These studies suggest that osteoporosis is a systemic disease and that the calcaneus is as satisfactory a bone as any for following the dynamics of a generalised demineralising process.

The belief that weight had a disproportionate effect

on the calcaneus compared with other weight bearing bones has been dispelled. Age-adjusted correlation coefficients for height, weight and age with respect to mineral content at various skeletal sites were compared (Vogel, 1987; Horsman, 1976) and the correlations with weight are not that different for the spine (L1-L4) and calcaneus. The correlation coefficients were 0.42 and 0.49 respectively. Furthermore, the calcaneus and the lumbar spine had a similar reduction of bone mineral content with age. In both cases this reduction was shown to begin before menopause (Vogel 1987). Based upon cross-sectional data (Vogel 1987) it is evident that the bone mineral content of the calcaneus reflects changes with age in the lumbar spin bone mineral content.

Calcaneal bone mineral content can be used as an indicator of bone fracture risk. In the literature relacing to osteoporosis, there exists the concept of a fracture threshold, an arbitrary bone mass or mineral level below which the majority of fractures occur (Riggs et al., 1981). Although Ross et al. (1987) find the concept clinically useful, it has its shortcomings, not the least of which is the fact that it is not consistent with the nature of the disease. Furthermore, it cannot be applied to predicting the probability of fracture. Part of the reason is that bone mass and fracture risk are continuous and not

discrete variables. It is better to relate bone mineral content to the level of fracture risk. Prospective studies between bone mineral content and fracture risk have been reported (Ross et al., 1987; Wasnich et al., 1987; Wasnich et al., 1985; Wasnich, 1987) which show the predictive power of bone mineral measurements at four sites, after allowing for age, height and weight. The conclusion was that the relative risk of fracture increases exponentially with decreasing calcaneal bone mineral content. While lumbar spine bone mineral content also relates to spine fracture incidence, the association was found to be weaker.

In studies designed to measure therapeutic effects of estrogen and the combined effects of estrogen and thiazide by evaluating bone mineral content at the calcaneus, two radial sites and the lumbar spine (Wasnich et al., 1986) the positive effect of the drugs was greatest in magnitude for the calcaneus relative to the other three sites. This indicates that the calcaneus is more sensitive to changes in bone mineral content.

6.4 Summary

More than 90% of calcaneal bone mineral is trabecular and is easily accessible as a site for bone mineral content measurement. Age related patterns of bone loss in the calcaneus and spine are similar. The calcaneal bone mineral

content reflects the degree of spinal osteoporosis as well as the measurement of spinal bone mineral content. In certain therapeutic regimes, calcaneal bone mineral density is the best indicator of changes in trabecular bone mass.

The risk of fracture in both spine and other sites can be determined as well, if not better, from calcaneus as from the spine. It is for these reasons as well as for its accessibility that the calcaneus was chosen as the measuring site in which to test the technique that employs coherent scattering of gamma rays for measuring bone mineral concentrations.

6.5 In vitro measurements in the human calcaneus

Introduction

By the time measurements in the calcaneus were to be made, circumstances regarding the use of the McMaster University Nuclear Reactor for producing the ^{153}Sm source, had changed dramatically. The financial costs of producing the source had soared and a decision was made to seek an alternative source. Luckily, the department of Nuclear Medicine has to regularly replace its Dual Photon Absorptiometry ^{153}Gd source which is, at about 9 GBq, sufficiently active for the requirements of the in vitro measurements. Table 6.1 shows some of the physical properties of ^{153}Gd compared to ^{153}Sm. From now on, all the

Table 6.1 A comparison of the Physical properties of ^{153}Gd and ^{153}Sm

Property	^{153}Gd	^{153}Sm
Predominant gamma photon energies (MeV) and their absolute intensities (%)	97.5 (36.5%) 103.2 (26.6%)	103.2 (28.2%)
Half Life	242 days	46.3 hours

measurements were made using the 103.2 keV photons of the ^{153}Gd source.

6.5.1 Measurements in water

Three human calcanei were selected for measurement using the coherent/transmission technique. One of the three bones, bone 1, had its calcium content deliberately reduced by soaking overnight in a 200 ml beaker containing 36 g NaCl, 192 ml of water and 8 ml of concentrated hydrochloric acid.

Each of the three calcanei was separately placed in a transparent plastic container of about 53 mm diameter containing de-ionised and distilled water. The calcaneus was positioned at the centre of the container with its long axis vertical and its posterior tuberosity touching the bottom of the container. Small pieces of polyurethane foam were used as fillers to keep the calcaneus in a fixed position. To remove any air trapped in the bones and the filler foam, the bone containers were placed in a desiccator which was then evacuated. As the air was removed from the bone it was replaced by water. In this set-up, with the calcaneus surrounded by water, the water simulates the soft tissues that surrounded the bone in vivo.

Two scattering and two transmission measurements were made for each bone as per figure 5.1 using the experimental

arrangement depicted in figure 4.1. The angle of scatter was 40^{o}. The scatter ratio was obtained according to equation 5.5. In addition to the three calcanei, the scatter ratio for water was measured.

The bones were removed from their containers and dried. Three months later, the same measurements were performed with the same bones. This time though, each bone was measured five times in order to assess the reproducibility of the measurements. Between each measurement each bone was removed from its container, dried and the whole process repeated. Positioning of the calcaneus in the same spot in the water container is a difficult task, even with the use of polyurethane foam. This is expected to lower the precision since scattering volumes and attenuation path lengths will be slightly different from one measurement to the next. This was a time consuming process, which is why each bone was measured only five times. For the same reasons, only a few bone samples were measured.

The measurements for water scatter ratios were repeated ten times. Since the container was symmetrical (cylindrical) and its contents (water) homogeneous, only one scatter and one transmission measurement was required. The water scatter ratios were obtained using equation 5.6. For water, the average scatter and transmission count rates were

6.3 and 6043 counts per minute respectively. For bone, for example bone 2, the average scatter and transmission count rates (with the bones in water) were 10.9 and 5574 counts per minute respectively. The scatter measurements were each collected over a preset time of approximately 12 hours.

6.5.1.1 Results

The results of the measurements are shown in table 6.2. The ratios in column A are the one-time measurements and those in column B are the average of repeated measurements made three months after the column A measurements. The standard deviation (S.D.) relates to the B column results only. S.D. is given by the expression:

$$S.D. = \left[\frac{\Sigma(x_i - \bar{x})^2}{n - 1}\right]^{1/2} \qquad (6.1)$$

where n is the total number of measurements, x_i, and $\bar{x}$ is their mean.

The reproducibility as expressed by the coefficient of variation (CV), that is the standard deviation divided by the mean, varies from 3% to about 7%. While it is recognised that the CV is an inappropriate expression of reproducibility since it also depends upon the mean, it has unfortunately become the conventional measure of precision in bone mineral measurement literature.

The scatter ratio for bone 1 is significantly

Table 6.2 Measurements in Water

	Scatter Ratio ($x10^{-3}$)		S.D. $x10^{-3}$
	A	B	
Water	0.98	1.05	0.05
Bone 1	1.55	1.59	0.04
Bone 2	1.97	1.97	0.06
Bone 3	1.98	2.09	0.15

different from the ratios of bones 2 and 3. This is expected since the calcium component of its bone mineral was deliberately depleted before the measurement was performed.

6.5.2 Corn-oil measurements

It is known that when trabecular bone is resorbed, it is replaced by marrow fat. Puumalainen et al., (1976) found that a 30% change in trabecular bone mineral density corresponds to only a 10% change in physical bone density. Having made the calcanei measurements in water to simulate soft tissue effects, it was deemed prudent to simulate marrow fat.

Corn oil was selected for use as marrow fat substitute. Commercial corn oil (Mazola) was obtained from a local supermarket. Its specific gravity was determined to be 0.915 and its effective atomic number was determined to be 5.51. From data available from the CRC, Handbook of Chemistry and Physics (53rd edition), corn oil is made of essentially four components. These are tetradecanoic acid ($CH_3(CH_2)_{14}CO_2H$, (10%)), octadecanoic acid ($CH_3(CH_2)_{16}CO_2H$ (3%)), 9-octadecanoic acid (cis) $c9H_3(CH_2)CH{:}CH(CH_2)_7\ CO_2H$ (50%)) and 9, 12-octadecadienoic acid ($CH_3(CH_2)_7CH{:}CHCH_2CH{:}CH(CH_2)CH{:}CH(CH_2)_7CO_2H$ (35%)). The proportions of carbon, hydrogen and oxygen in the four components can be written as $C_{16}H_{32}O_2$, $C_{18}H_{36}O_2$, $C_{18}H_{34}O_2$ and $C_{18}H_{32}O_2$,

respectively. For the purposes of determining an approximate effective atomic number for corn oil, 9-octadecenoic acid was used. The effective atomic number was obtained using equation 4.4.

The same calcanei used in section 6.5.1 for water measurements were used for corn oil measurements. The bones were dried in an oven at about 100^{o} C for 24 hours. They were then placed in corn oil within rubber balloons and put aside for 24 hours to allow the corn oil to penetrate the bones. More corn oil (about 30 ml) was added to the balloons before their openings were tied. The whole package (calcaneus-in-corn oil-in balloon) was placed in plastic containers identical to those used for the water measurements. De-ionised, distilled water was added to the container. The purpose of the balloon was to prevent corn oil from mixing with water. Care was taken to position the calcaneus at the centre of the container, with the calcaneal tuberosity touching the bottom of the container. Again polyurethane foam fillers were used to keep the calcaneus in a fixed position within the water container.

As in section 6.5.1, two scatter and two transmission measurements were performed on each bone. The average scatter and transmission count rates for bone 2 in corn oil and water were 6.4 and 6798 counts per minute respectively. Once again the preset time for each scattering measurement

was about 12 hours. The scatter ratio was determined through the use of equation 5.5 and for each bone the ratio was determined a total of five times. In between the measurements the bones were removed from their water containers and their balloons and the whole procedure was repeated.

6.5.2.1 Results

The results of the corn oil measurements are shown in table 6.3. One striking feature of the results is that they are low compared to the ratios obtained for "in-water" measurements. However, their precision, as measured from the standard deviation divided by the mean, is similar in magnitude. The scatter ratio of bone 1 is, as expected, lower than that of bones 2 and 3.

6.6 Analysis of results

Trabecular bone consists of scattered trabeculae in a large marrow space. Within any sample of trabecular bone the space occupied by bone varies, not only from one site to another, but also with age. The "normal" percentage, by volume, of bone in trabecular bone can be as high as 27% (Nordin, 1983; Aaron et al., 1974) for young adults and as low as 15% (Aaron et al., 1974) for sixty year olds. Jowsey (1977) gives an average figure of about 23%. In calcaneal

Table 6.3 Corn oil measurements

Bone	Scatter Ratio ($x10^{-3}$)	S.D. ($x10^{-3}$)
1	0.80	0.03
2	0.91	0.08
3	0.89	0.07

trabecular bone, the remainder is mostly yellow marrow. The age of the calcanei used in this study is not known and the fraction of bone was assumed to be about 20%.

Since the calcanei had been dried in the above measurements, marrow space (80%) was taken up by water or corn oil. The effective atomic number of the scattering volume contents with the calcanei in water and in corn oil can be approximated by using the relation:

$$Z_{eff}(SV) = f_b Z_{eff}(b) + (1-f_b) Z_{eff}(w/co) \qquad (6.2)$$

where $Z_{eff}(SV)$ is the effective atomic number of the material in the scattering volume, f_b is the fraction by volume, of bone in the scattering volume, $Z_{eff}(b)$ is the effective atomic number of bone and $Z_{eff}(w/co)$ is the effective atomic number of water or corn oil. If the scattering volume contains 20% bone and the remainder is either water or corn oil, then the appropriate effective atomic numbers for bone in water and bone in corn oil will be respectively:

$$Z_{eff}(SV) = (0.20 \times 11.40) + (0.8 \times 7.10) = 7.96 \qquad (6.3)$$

$$Z_{eff}(SV) = (0.20 \times 11.40 + (0.8 \times 5.51) = 6.69 \qquad (6.4)$$

The effective atomic numbers for bone, water and corn oil are 11.40, 7.10 and 5.51 respectively.

Assuming the normalised bone scatter ratios (NBR) are

governed by the same power law, equation 5.13, exhibited by aqueous solutions of K_2HPO_4 in their relation with effective atomic numbers, then the effective atomic numbers calculated using equation 6.2, can be checked using the equation:

$$Z_{eff} = \left(\frac{NBR}{a_o} \right)^{1/n} \qquad (6.5)$$

where NBR is the normalised coherent/transmission ratio for bone in either water or corn oil, a_o and n, are the parameters determined for equation 5.13.

The results calculated using equation 6.5, are shown in tables 6.4 and 6.5. Agreement between the results of equation 6.2 through to 6.5 is good.

6.7 Measuring bone volume and bone mineral density

From the three calcanei whose coherent/transmission ratios were determined above, cuboid samples, of side approximately 16 mm were cut out of the posterior region of each bone. Care was taken to exclude cortical bone.

Since trabecular bone is porous, the bone sample dimension do not correspond to the bone matrix volume and so the actual bone material volume was determined using the Archimedes method as shown in figure 6.7. Each cuboid trabecular bone sample was first weighed in air to get its weight, W_a. In order to ensure that the dry bone weight was obtained, the samples were left in an oven at 80^oC for 24

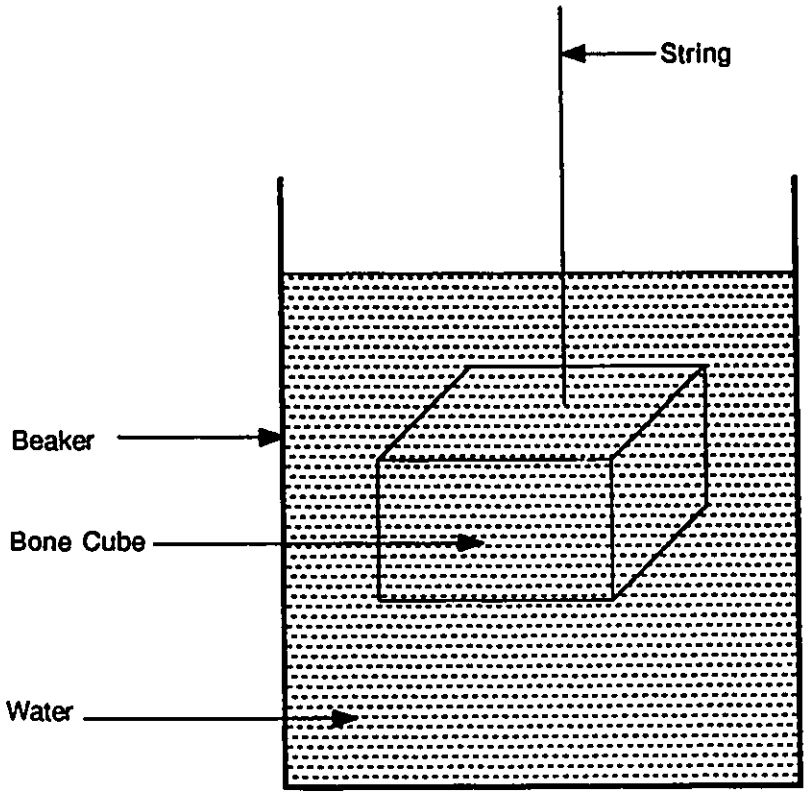

Figure 6.7 Determination of bone volume by Archimedes' method.

Table 6.4 Calculated effective atomic numbers and their associated normalised coherent transmission ratios (Water measurements)

	Normalised ratio (NBR)	Effective atomic numbers (Z_{eff})
Water	1.00	7.03
Bone 1	1.51	7.97
Bone 2	1.88	8.51
Bone 3	1.99	8.66

Table 6.5 Calculated effective atomic numbers and their associated normalised coherent/transmission ratios (Corn oil measurements)

	Normalised ratio (NBR)	Effective atomic number (Z_{eff})
Water	1.00	7.03
Bone 1	0.76	6.47
Bone 2	0.87	6.74
Bone 3	0.85	6.69

hours and were weighed within about two minutes of removal from the oven. They were then weighed in water to obtain the weight W_w. The latter is the difference between the weight in air, W_a, and the weight of the volume of water displaced by the bone, $V_b\rho_w$. We can write the equation:

$$W_w = W_a - V_b\rho_w \qquad (6.6)$$

where V_b is the volume of water displaced and is equal to the volume of bone and ρ_w is the density of water. The volume of bone is obtained by re-arranging equation 6.6.

In order to ensure that there was no air in the bone cavities during the water displacement measurement, the bone samples were put in beakers of water in a desiccator which was then closed and evacuated. As the air was sucked out of the bone cavities, it was replaced by water, and the bone cube which would initially be floating in the water, would slowly sink to the bottom of the beaker. The cube was then suspended with a thin cotton thread and weighed while still submerged in water. Care was taken to ensure that the sample did not touch the sides nor the bottom of the beaker during the weighing.

The results of the measurements and the bone sample volumes calculated from the measurements are given in table 6.6.

Table 6.6 Determination of bone volume

	Weight in air (W_a) (grams)	Weight in water (W_w) (grams)	Bone volume (cm^3) $(W_a-W_w)/\rho_w$
Bone 1	1.359	0.754	0.605
Bone 2	2.349	1.366	0.983
Bone 3	2.487	1.465	1.022

6.7.1 Bone mineral density

Once the volumes of the bone samples were determined, the bone mineral content of the samples was determined by ashing. The cubes were individually placed in pre-weighed crucibles and put in a muffle furnace at 600^{o} C for 48 hours. The weight of the ash is the bone mineral without the organic components. The crucibles were weighed within 10 minutes of being taken out of the furnace. When the weight of each bone sample is divided by the volume of the sample determined by the Archimedes method, the trabecular bone mineral density is obtained.

The bone mineral densities of the three calcanei used and their measured normalised coherent/transmission ratios are shown in table 6.7.

6.7.2 Discussion

The variation of the normalised coherent/transmission ratio with bone mineral density for the three calcanei measured appears to be linear as shown in figure 6.8. The coefficient of determination is 0.99. Figure 6.8 is a calibration curve which predicts the bone mineral density (BMD) from a measurement of the normalised coherent/transmission ratio according to the equation:

Table 6.7 Bone mineral density and normalised coherent/ transmission ratio

	Bone mineral (ash) (g/cm^3)	Normalised coherent/ transmission ratio (NBR)
Bone 1	1.43	1.51
Bone 2	1.70	1.88
Bone 3	1.73	1.99

$$NBR = 1.51 * BMD - 0.66 \quad (6.7)$$

or $$BMD = 0.65 * NBR + 0.45 \quad (6.7a)$$

Although the correlation between bone mineral density and NBR is high, only three calcanei were studied. A larger number and range of bone mineral density values is required in order to establish a more robust calibration curve than that described by equation 6.7.

6.8 Skin dose

Entrance and exit skin doses were measured using thermoluminescent dosimeters (TLD). The experimental arrangement for the procedure is shown in figure 6.9.

The TLD was lithium borate ($Li_2B_4O_7$:Cu) in the form of chips. This material is tissue-equivalent, with an effective atomic number of 7.3. To measure the entrance skin dose, the chip was sandwiched between the water container and a 2 mm thick sheet of perspex. This was done in order to effect charged particle equilibrium at the chip.

The TLD's were obtained already annealed from the McMaster University Health Physics Unit. They were irradiated, as shown, for 24 hours. Another 24 hours after cessation of irradiation, the chips were read using the Panasonic 702E Manual reader. For a patient measurement in which the total cumulated coherent counts would be about 10,000, the skin entrance and exit doses are found to be 6 and 1.5 milliSievert respectively. The uncertaintly of the measurement is 7%.

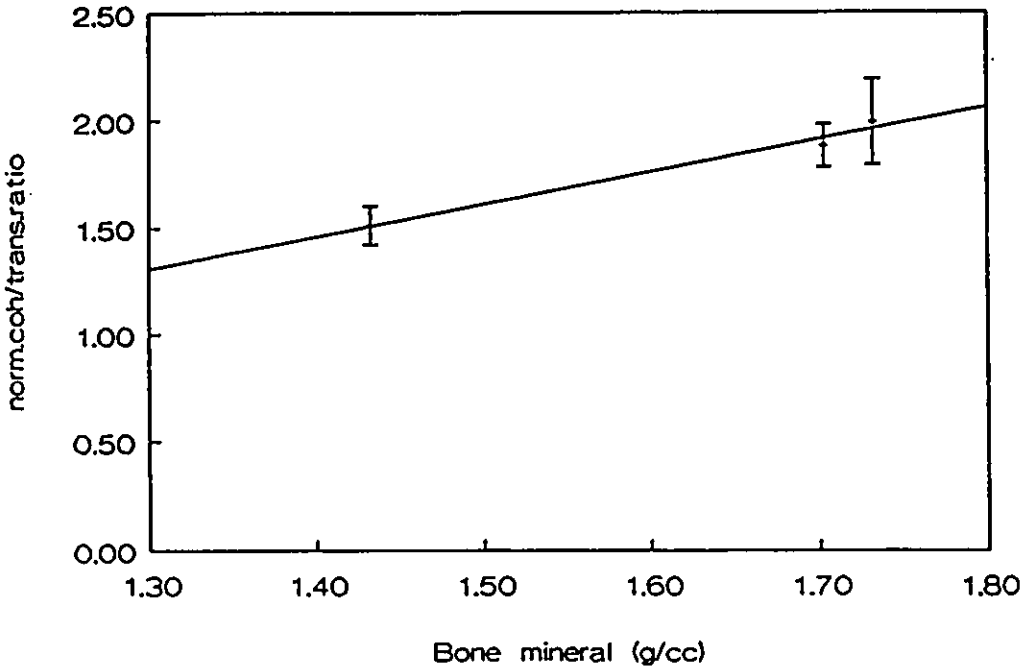

Figure 6.8 The variation of the normalised coherent/transmission ratio with bone mineral.

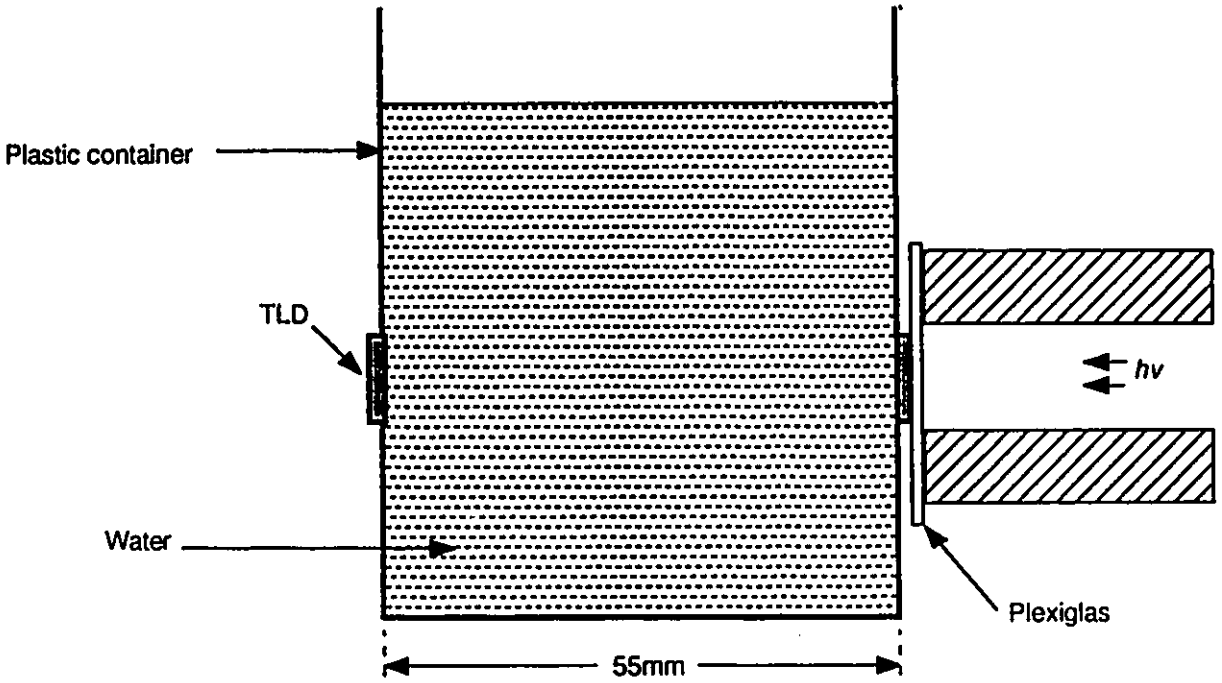

Figure 6.9 Measurement of skin entrance and exit dose.

CHAPTER 7

CONCLUSION

7.1 Introduction

This research indicates that a bone mineral measurement technique based on the coherent scattering of gamma rays is possible. Correction for attenuation of photons before and after scattering is provided by performing two scatter and two transmission measurements. The ratio of the former to the latter has been shown to be independent of overlying tissue thickness and to be an indicator of bone mineral density. However, before a clinical system can be built and tested, some work still needs to be done, particularly with regard to reducing the measuring time which is currently impractically long.

In this chapter possibilities for improvement are considered, a means of calibration of a clinical system is proposed and a clinical trial is described which will reveal the sensitivity of the system to a known in vivo difference in bone mineral concentration.

7.2 Improvements

The feasibility of the technique has been established. A viable clinical system will require a

reduction of the measurement time by an order of magnitude. There are four options. The source strength could be increased. The problem with this route is that the cost of procuring the source will be prohibitively high. Currently a 40 GBq source of ^{153}Gd costs about $6,000. An additional nuisance is that the source half life is relatively short and the source has to be replaced every year or so, adding further to the cost.

A second option would be to use several detectors or a ring of detectors. Unfortunately the detectors are also very expensive. The single detector used in this study cost $13,000.

A third approach would be to investigate further the possibility of reducing the scattering angle somewhat to increase the coherent count rate. This would require an improved means of separating the coherent and Compton peaks perhaps by obtaining a detector of better energy resolution. This option is rather weak, since, as was indicated in Chapter 4, smaller scattering angles tend to produce scattering volumes which are difficult to confine completely within a restricted and desired region of trabecular bone.

A fourth option may be a combination of the above three.

7.3 Techniques currently in clinical use

Another important question to consider is what improvements may arise clinically from a coherent-transmission system. Currently the clinical techniques available to physicians for assessing bone mineral status are dual photon absorptiometry (DPA) and quantitative computed tomography (QCT). It is generally accepted that the rapid turnover rate of trabecular bone, and its concomitant rapid response to metabolic stimuli, makes it a sensitive site for measuring changes in bone mineral concentration. The major disadvantage of DPA is that even when the measuring site is a cancellous bone like the spine, where the fractional content of trabecular bone is high, the posterior processes which consist predominantly of cortical bone are included. The measurement is therefore an integral of compact and trabecular bone and some sensitivity to changes in trabecular bone mineral concentration is lost. The measurement also depends upon the size of the subject since it cannot measure mineral concentration. However it is relatively inexpensive, simple to perform, has relatively low radiation dose and partially fulfills a need.

Quantitative computed tomography measures bone mineral concentration within the trabecular bone of a vertebral body. The equipment is, however, very expensive and is not dedicated to measuring bone density. Furthermore

it is difficult to reposition exactly the same location for sequential measurements and the radiation dose to the patient is high.

The coherent-to-transmission ratio technique would measure the mineral density of trabecular bone in a convenient skeletal site which indicates reliably the mineral status of the skeleton.

7.4 System calibration

Once a clinical system has been built, rigorous determination of accuracy and precision of the technique will be required. A number of cadaver calcanei with a large range of bone mineral density values will be collected. The coherent-to-transmission ratios will be measured for each calcaneus. In order to obtain the mineral mass per unit volume for each calcaneus, accurately known volumes (cuboids) would be cut and ashed. Plotting the coherent-to-transmission ratio against ash weight will yield the calibration curve. Accuracy of the bone mineral density measurement can be assessed from the average deviation of the points from the calibration curve. The precision of the technique would be determined by measuring a single calcaneus repeatedly over a period of time.

7.5 Sample size estimation

The final evaluation will be to test the ability of the system to detect the known clinical difference in bone mineral density between normal young adult women and normal older women. The 25-35 year old, normal women group will constitute one population with a mean trabecular mineral density of $\bar{x}_o$ and a standard deviation of σ_o. The second population of elderly adult women will have a mean trabecular mineral density of $\bar{x}_y$ and a standard deviation of σ_y. Statistical formulae are available for sample size determination for studies whose aim is to demonstrate a significant difference. The null hypothesis that there is no difference between the means can be tested statistically. The probability of incorrectly rejecting the null hypothesis (the alpha level) is conventionally set equal to 0.05. The probability of incorrectly accepting the null hypothesis (the beta level) can be set equal to 0.10. Selection of these α and β levels means that a sample size can be no smaller than n where n is given by

$$n = \frac{(Z_\alpha + Z_\beta)^2(\sigma_y^2 + \sigma_o^2)}{(\bar{x}_o - \bar{x}_y)^2} \qquad (7.1)$$

Z_α and Z_β are determined by the chosen α and β levels and in this case are 1.96 and 1.28 respectively.

According to equation 7.1, the means of the two

variables and their standard deviations are required in order to determine the minimum sample size for the study to assess the clinical sensitivity of the technique. Since such data are not available for the coherent-to-transmission technique, data for the QCT technique can be used for the purposes of calculating a minimum sample size. The justification for this approach is two fold. First, both the coherent-to-transmission technique and the QCT technique measure the same parameter, trabecular mineral mass per unit volume. While one measures spinal mineral density and the other measures calcaneal mineral density, age related bone loss in the spine and calcaneus are similar (section 6.3). Second, the minimum size is just an estimate which is usually increased to allow for possible non response or drop-outs and the need to control for confounding variables in the analysis. Genant et al. (1985) have published mineral densities for younger and older adult women. The values were 175 ± 28 mg/ml and 125 ± 28 mg/ml respectively. Using these values means that the clinical sensitivity study will require sample sizes of about 10 subjects in each group.

In conclusion a dedicated, clinical system based on coherent gamma ray scattering will provide clinicians with an assessment of skeletal status which combines the advantages of both DPA and QCT.

REFERENCES

Aaron, J.E., Gallagher, J.C., Anderson, J., Stasiak, L., Longron, E.B., Nordin, B.B.C., Nicholson, M. (1974) Frequency of Osteomalacia and Osteoporosis in fractures of the proximal femur. Lancet 1I 229-233.

Anderson, J.B., Shimmins, J., Smith, D.A. (1966) A new technique for measurement of metacarpal density. Br. J. Radiol. 39, 443-450.

Attix, F.B. (1986) Introduction to Radiological Physics and Radiation Dosimetry. (John Wiley and Sons, New York).

Bevington, P.R. (1969) Data Reduction and Error Analysis for Physical Sciences. McGraw-Hill Book Company, Toronto.

Bradley, J.G., Huang, H.K., Ledley, R.S. (1978) Evaluation of Calcium concentration in bones from CT scans. Radiol. 128, 103-107.

Bradley, D.A., Ghose, A.M. (1984) Photon scattering in biomedically important elements. Phys. Med. Biol. 29, 1385-1397.

Brenner, S., Brown, G.E., Woodward, J.B. (1954) Coherent scattering of γ-rays by K electrons in heavy atoms (Part II): Scattering of 0.32 mc^2 γ-rays in mercury. Proc. Roy. Soc. A227, 59.

Brown, G.E., Peierls, R.E., Woodward, J.B. (1954) Coherent scattering of γ-rays by K electrons in heavy atoms (Part I). Proc. Roy. Soc. A227, 51-58.

Brown, G.E., Mayers, D.F. (1955) Coherent scattering of γ-rays by K electrons in heavy atoms (Part III): The scattering of 0.64 mc^2 γ-rays in mercury. Proc. Roy. Soc. A234, 387-390.

Brown, G.E., Mayers, D.F. (1957) Coherent scattering of γ-rays by K electrons in heavy atoms (Part IV): The scattering of 1.28 and 2.56 mc^2 γ-rays in mercury. Proc. Roy. Soc. A242, 89.

Brown, W.D. (1966) Boeing Co. (Seattle, Wash.) Report D2-125137-1.

Cameron, J.R., Sorenson, J. (1963) Measurement of bone mineral in vivo: An improved technique. Science 142, 230-232.

Carter, D.R., Hayes, W.C. (1976) Bone compressive strength: The influence of density and strain rate. Science 194, 1174-1176.

Christiansen, M.S., Christiansen, C., Naestoft, J., McNair, P., Transbol, I. (1981) Normalisation of bone mineral content to height, weight and lean body mass: Implications for Clinical Use. Calcif. Tissue Int. 35, 5-8.

Clark, R.L., Van Dyk, G. (1973) A new method for measurement of bone mineral content using both transmitted and scattered beams of gamma rays. Phys. Med. Biol. 18, 532-539.

Cohn, S.H. (1976) Non-invasive measurements of bone mass and their clinical applications. CRC Press.

Compton, A.H. (1923) Quantum theory of the scattering of x-rays by light elements. Phys. Rev. 21, 207 and 483-502.

--------. (1930) Determination of electron distributions from measurements of scattered x-rays. Phys. Rev. 35, 925-938.

Compton, A.H., Allison, S.K. (1935) X-rays in theory and experiment. Van Nostrand, New Jersey.

Cromer, D.T., Mann, J.B. (1968) X-rays scattering factors computed from numerical Hartree-Fock wave functions. Acta Crys. A24, Part 2, 321-324.

Davis, M.W., Webber, C.E. (1978) The reactor production of a low energy high intensity beam. Nucl. Instr. Meth. 154, 395-398.

Davisson, C.M., Evans, R.D. (1952) Gamma-ray absorption coefficients. Rev. Mod. Phys. 24, 79-107.

Davisson, C.M. (1965) Alpha-beta-gamma-ray spectroscopy. ed. Seigbahn, K. Ch. 2, 1, 37.

Debye, P. (1923) Scattering of x-rays and the quantum theory. Phys. Zeits. 24, 161.

Debye, P., Harm, F. (1930) X-ray interference and atomic dimensions. Phys. Zeits. 31, 419-428.

Delbrück, M. (1933) "Zusatz bei der Korrektur". Z. Physik 84, 144.

Dunn, W.L., Wahner, H.W., Riggs, B.L. (1980) Measurement of BMC in human vertebrae and hips by dual photon absorptiometry. Radiol. 136, 485-487.

Dyson, N.A. (1973) X-rays in atomic and nuclear physics (Longman, London).

Dyson, N.A. (1981) An Introduction to Nuclear Physics with Applications in Medicine and Biology. (Ellis Horwood Limited, Publishers Chichester).

Farrell, T.J., Webber, C.E. (1989) The error due to fat inhomogeneity in lumbar spine bone mineral measurements. Clin. Phys. Physiol. Meas. 10, 57-64.

Farrell, T.J. (1990) Photon absorptiometry in three component systems. Ph.D. Thesis, McMaster University, Hamilton, Ontario.

Florescu, V., Gavrila, M. (1976) Elastic scattering of photons by K-shell electrons at high energies. Phys. Rev. A14, 211-235.

Fock, V. (1930) Approximate method of solution of the problem of many bodies in quantum mechanics. Z. Phys. 61, 126-148.

Fock. V., Petrashen, M.J. (1934) Numerical solution of generalised equations of the self-consistent field. Phys. Z. Sowjetunion 6, 638-414.

Franz, W. (1935) "Streuung harter strahlung durch gebundene elektronen". Z. Physik 95, 652-668.

--------. (1936) "Rayleighsche streuung harter strahlung an schureren atomen". Z. Physik 98, 314-320.

Fricke, H., Glasser, O. (1925) A theoretical and experimental study of the small ionisation chamber. Am. J. Roentgenology 13, 453-461.

Frost, H.M. (1966) Bone dynamics in metabolic disease. J. Bone and Joint Surg. 48A, 1192-1203.

Garnett, E.S., Kennett, T.J., Kenyon, D.B., Webber, C.E. (1973) A photon scattering technique for measurement of absolute bone desnity in man. Radiol. 106, 209-212.

Genant, H.K., Cann, C.E., Chafetz, N.I., Helms, C.A. (1981) Advances in computed tomography of the muscoskeletal system. Radiol. Clin. North America 19, 645-647.

Genant, H.K., Block, J.E., Steiger, P., Glueer, C-C., Smith, R. (1987) Quantitative computed tomography in assessing osteoporosis. Sem. Nuc. Med. XVII, 316-333.

Goldberger, M.L., Low. F.E. (1968) Photon scattering from bound atomic systems at very high energy. Phys. Rev. 176, 1778-1781.

Grodstein, G.W. (1957) X-ray attenuation coefficients from 10 keV to 100 MeV. Nat. Bur. St. Cir. 583 (54 pages).

Hanna, G.C. (1961) The depression of thermal neutron flux and density by absorbing foils. Nuclear Science and Engineering 11, 338-339.

--------. (1963) The nuetron flux perturbation due to an absorbing foil: A comparison of theories and experiments. Nuclear Science and Engineering 15, 325-337.

Hansen, J.S., McGeorge, J.C., Nix, D., Schmidt-Ott, W.D., Unus, I., Fink, R.W. (1973) Accurate efficiency calibration and properties of semiconductor detectors for low energy photons. Nucl. Instr. Meth. 106, 365-379.

Hartree, D.R. (1925) The atomic structure factor in the Intensity of Reflection of x-rays in crystals. Philos. Mag. 50, 289-306.

--------. (1928) The wave mechanics of an atom with a non-Coulomb central field. Proc. Cambridge Phil. Soc. 24, 89-132.

Hendee, W.R. (1970) Medical Radiation Physics. Yearbook Medical Publisher, Chicago.

Horsman, A. (1976) (Bone mass) In: Nordin, B.E.E., ed. Calcium Phosphate and Magnesium Metabolism. (Churchill, Livingstone)

Hubbell, J.H. (1965) Common volume of two intersecting cylinders. J. Research Nat. Bureau Standards - C, 69C, 139.

Hubbell, J.H., Overbo, I. (1979) Relativistic atomic form factors and photon coherent scattering cross sections. J. Phys. Chem. Ref. Data 8, 69-105.

Hubbell, J.H., Veigele, W.J., Briggs, E.A., Brown, R.T., Crommer, D.T., Howerton, R.J. (1975) Atomic form factor, incoherent scattering functions and photon scattering cross sections J. Phys. Chem. Ref. Data 4, 471-538.

ICRP Report #23 (1974) Report of the task group on Reference Man. Pergamon Press.

James, R.W. (1962) The Optical Principles of the Diffraction of x-rays. Bell, London.

Jowsey, J. (1977) Metabolic Diseases of Bone. W.B. Saunders. Philadelphia.

Karellas, A., Leichter, I., Craven, J.D., Greenfield, M.A. (1983) Characterisation of tissue via coherent-to-Compton scattering ratio: Sensitivity considerations. Med. Phys. 10, 605-609.

Kennett, T.J., Webber, C.E. (1976) Bone density measured by photon scattering. II. Inherent sources of error. Phys. Med. Biol. 21, 770-780.

Kerr, S.A., Kouris, K., Webber, C.E., Kennett, T.J. (1980) Coherent scattering and the assessment of mineral concentration in trabecular bone. Phys. Med. Biol. 25, 1037-1047.

Kissel, L., Pratt, R.H. (1978) New predictions for Rayleigh scattering: 10 keV - 10 MeV. Phys. Rev. Lett. 40, 387-391.

Kissel, L., Pratt, R.H., Roy, S.C. (1980) Rayleigh scattering by neutral atoms, 100 eV to 10 MeV. Phys. Rev. A22, 1970-2004.

Kirkwood, B.R. (1988) Essentials of Medical Statistics, Blackwell Scientific Publications, Oxford.

Klein, O., Nishina, Y. (1929) "Uber die streuung von strahlung durch freie electronen nach neuen relatioischen quanten-dynamik von Dirac". Z. Physik 52, 853-868.

Krolner, B., Nielsen, S.P. (1980) Measurement of bone mineral content (BMC) of the lumbar spine, 1. Theory and application of a new two dimensional dual photon attenuation method. Scand. J. Clin. Lab. Invest. 40, 653.

Lahtinen, T., Vaananen, A., Karjalainen P. (1980) Effect of intraosseous fat on the measurements of bone mineral of distal radius. Calcif. Tissue Int. 32, 78.

Ling, S.S., Rustgi, S., Karellas, A., Craven, J.D., Whiting, J.S., Greenfield, M.A. Stern, R. (1982) The measurement of trabecular bone mineral density using coherent and Compton scattered photons in vitro. Med. Phys. 9, 208-215.

Mayneord, W.V. (1937) Significance of the röntgen. Acta. de l'Union Internationale Centre le Cancer, 2, 271-282.

Mazess, R.B. (1971) Estimation of bone and skeletal weight by direct photon absorptiometry. Invest. Radiol. 6, 52-60.

--------. (1979) Measurement of skeletal status by non-invasion methods. Calcif. Tissue Int. 28, 89.

--------. (1981) in Non-invasive measurements of bone mass and their clinical applications. ed. Cohn, S.H. CRC Press, 85-89.

McCullough, E.C. (1975) Photon attenuation in computed tomography. Med. Phys. 2, 307-320.

Meema, H.E., Meema, S. (1969) Cortical bone mineral density versus cortical thickness in the diagnosis of osteoporosis: A Roentglnologic-densitometric study. J. Am. Geront. Soc. 17, 120.

Meema, H.E., Meema, S. (1975) Improved Roentgenological diagnosis of osteomalacia by microradioscopy of hand bones. Am. J. Roentgen. 125, 925-935.

Messiah, A. (1965) Quantum Mechanics I, North-Holland, Amsterdam.

Mossop, R.J., Kerr, S.A., Bradley, D.A., Chong, C.S., Ghose, A.M. (1987) The use of coherent gamma ray scattering for characterisation of materials. Nucl. Instr. Meth. A255, 419-422.

Moon, P.B. (1950) The hard components of scattered gamma-rays. Proc. Phys. Soc. (London), A63, 1189.

NEMA, (1980) Performance Measurements of Scintillation Camera (Nema), Standard Publication No. NU1.

Oeser, H., Krokowski, E. (1963) Quantitative analysis of inorganic substances in the body. br. J. Radiol. 36, 274-279.

Peppler, W.W., Mazess, R.B. (1981) Total body mineral and lean body mass by DPA, I. Theory and measurement procedure. Calcif. Tissue Int. 23, 353-359.

Price, R.R., Wagner, J., Larsen, J., Patton, J., Brill, A.B. (1976) Regional and whole-body mineral content measurement with a rectilinear scanner.Am. J. Roentgen. 126, 1277-1278.

Puumalainen, P., Uimarihuhta, A., Alhava, E., Olkkonen, H. (1976) A new photon scattering method for bone mineral density measurement. Radiol. 120, 723.

Radford, D.C. (1985) Program GELIFIT, available from AECL, Chalk River Nuclear Labs, Chalk River, Ontario, Canada.

Rasmussen, H., Bordier, P. (1974) The Physiological and Cellular Basis of Metabolic Bone Disease (Williams and Wilens, Baltimore).

Riggs, B.L., Wahner, H.W., Dunn, W.L., Mazess, R.B., Offord, K.P., Melton, L.J. (1981) Differential changes in bone mineral density of the appendicular and axial skeleton with aging. Relationship to spinal osteoporosis. J. of Clin. Invest. 67, 328-335.

Roos, B., Skoldborn, H. (1974) Dual photon absorptiometry in lumbar vertebrae I. Theory and Methods, Act. Radiol. Ther. Phys. Biol. 13, 266.

Ross, P.D., Wasnich, R.D., Heilbrun, L.K., Vogel, J.M. (1987) Definition of spine fracture threshold based upon prospective fracture risk. Bone 8, 271-278.

Roy, R.R., Reed, R.D. (1968) Interactions of photons and leptons with matter. (Academic, New York).

Schiff, L.I. (1955) Quantum Mechanics. 2nd ed. (McGraw-Hill Company, New York).

Siegbahn, K. (1965) Alpha, beta, gamma ray spectroscopy. North-Holland Amsterdam.

Shimmins, J., Smith, D.A., Aitken, M., Anderson, J.B., Gillespie, F.C. (1972) The accuracy and reproducibility of bone mineral measurements in vivo (a) and (b). Clin. Radiol., 23, 42-57.

Smith, D.L. (1971) Variation of the intrinsic efficiency of a cylindrical planar Ge(Li) Gamma ray detector with source distance. Nucl. Instr. Meth. 94, 157-163.

Shukla, S.S., Karellas, A., Leichter, I., Craven, J.D., Greenfield, M.A. (1985) Quantitative assessment of bone mineral by photon scattering: Accuracy and precision considerations Med. Phys. 12, 447-448.

Spiers, F.W. (1946) Effective atomic number and energy absorption in tissues. Br. J. Radiol. 19, 52-63.

Slater, J.C. (1951) A simplification of the Hartree-Fock method. Phys. Rev. 81, 385-390.

Tsoulfanidis, N. (1983) Measurement and Detection of Radiation. McGraw-Hill, Hemisphere Publishing Corporation.

Vigorita, V.J. (1984) Symposium on metabolic bone diesases. Orthop. Clin. N. America 15.

Veigele, W.J. (1967) Kaman Sciences Corp. (Colorado Springs) Report KN-378-67-3(R).

--------. (1973) Photon cross sections from 0.1 keV to 1 MeV for elements Z=1 to Z=94. Atomic Data Tables 5, 51-11.

Vogel, J.M. (1987) Applications and technical considerations in SPA. In: Genant, H.K. ed. Osteoporosis update 1987, Berkeley: University Press, 219-231.

Vogel, J.M., Wasnich, R.D., Ross, P.D. (1988) The clinical relevance of calcaneus bone mineral measurements: a review. Bone and Mineral 5, 35-58.

Wahner, H.W. (1987) Measurements of bone mineral by photon absorptiometry, in Fogelman I(ed): Bone Scanning in Clinical Practice. Berlin, Springer-Verlag.

Wasnich, R.D., Ross, P.D., Heilbrun, L.K., Vogel, J.M. (1985) Prediction of postmenopausal fracture risk with use of bone mineral measurements. Am. J. Obst. Gynecol. 153, 745-751.

Wasnich, R.D., Vogel, J.M., Yano, K., Ross, P.D. (1985) Osteoporosis among Hawaii Japanese: A review of the major findings of the Kuakini osteoporosis study. Hawaii Medical Journal 44, 309-312.

Wasnich, R.D., Ross, P.D., Heilbrun, L.K., Vogel, J.M., Yano, K., Benfante, R.J. (1986) Differential effects of thiazide and estrogen upon bone mineral content and fracture prevalence. Obst. and Gynecol. 67, 457-462.

Wasnich, R.D. (1987) Fracture prediction with bone mass measurements. In: Genant, H.K., ed. Osteoporosis update 1987. Berkeley: University Press, 95-101.

Wasnich, R.D., Ross, P.D., Heilbrun, L.K., Vogel. J.M (1987) Selection of the optimal site for fracture risk prediction. Clin. Orthop. Rel. Res. 216, 262-269.

Weaver, J.K., Chalmers, J. (1966) Cancellous Bone: Its strength and changes with aging and an evaluation of some methods for measuring its mineral content. J. of Bone and Joint Surg. 48-A, 289-299.

Webber, C.E., Garnett, E.S. (1976) Density of os calcis and limb dominance. J. of Anatomy 121, 203-205.

Webber, C.E., Kennett, T.J. (1976) Bone density measured by photon scattering. I. A system for clinical use. Phys. Med. Biol. 21, 760-769.

Webber, C.E. (1979) In: Non-invasive measurements of bone mass and their clinical applications. Cohn, S.H. ed. CRC Press, Florida.

Weiss, R.J. (1966) X-ray determination of electron distributions. Wiley and Sons, New York.

White, D.R. (1977) An analysis of the Z dependence of photon and electron interactions. Phys. Med. Biol. 22, 219-228.

Williams, E.D., Boddy, K., Harvey, Iris. Haywood, J.K. (1978) Calibration and evaluation of a system for toral body in vivo activation analysis using 14 MeV neutrons. Phys. Med. Biol. 23, 405-415.

Wilson, C.R., Madsen, M. (1977) Dichromatic absorptiometry of vertebral bone mineral content. Invest. Radiol. 12, 180-184.

WSU-NRC (1970) Gamma-ray energy tables for Neutron Activation Analysis, WSU-NRC-97(2).

Yano, K., Wasnich, R.D., Vogel, J.M., Heilbrun, L.K. (1984) Bone mineral measurements among middle-aged and elderly Japanese residents in Hawaii. Am. J. Epidemiol. 119, 751-764.

APPENDIX 1

DERIVATION OF THE COHERENT PEAK COUNTS

About 200 channels on either side of the centroid of the coherent peak are analysed. The spectrum in this region consists of the coherent peak superimposed on the high energy tail of the Compton peak. It is assumed that the coherent peak is Gaussian and that the Compton tail is described by a polynomial of up to order 4 and an inverse term. Thus the spectrum data is fitted to a function f(x) of a form given by;

$$f(x) = a_0 + \alpha_1 x + \alpha_2 x^2 + \alpha_3 x^3 + \alpha_4 x^4 + \frac{\alpha_5}{x} + \alpha_6 \, G(x,\sigma,x_0) \qquad \text{(A1.1)}$$

where α_0 to α_6 are parameters of the fit, x is the channel number and $G(x,\sigma,x_0)$ is a Gaussian with centroid x_0 and full width at half maximum (FWHM) σ.

Equation A1.1 is linear in the α's. (A's in the programme). Originally it was thought that σ and x_0 are constants rather than parameters to be fit. For this reason a linear least squares fit to the generalised function, that is, equation A1.1 was used (Bevington, 1969).

Subsequently, it was realised that x_0 and σ were not strictly constant and a non linear procedure was adopted.

It consisted of determining the value of χ^2 at five points, $[(x_0-\Delta x_0,\sigma),\ (x_0,\sigma),\ (x_0+\Delta x_0,\ \sigma),\ (x_0,\sigma-\Delta\sigma),\ (x_0,\sigma+\Delta\sigma)]$, in the (x_0,σ) space using the above-mentioned linear procedure. x_0 and σ were the first estimates of the centroid and FWHM. The value of the χ^2 was fit to a parabola in x_0 and σ and the minimum χ^2 was estimated.

The fitting procedure was run iteratively, with the minimum becoming the next estimate for the next iteration and with the step sizes Δx_0 and $\Delta\sigma$ chosen interactively. This yielded fits, with χ^2 of the order of 1 to 2.5. As indicated in Chapter 3, the coherent peak counts derived using this method agreed to within 5% those determined using an independent technique.

The data acquisition system used was an Aptec personal computer based multichannel analyser (PC/MCA). The spectrum file is a binary file with 32 bit unsigned integers. The programme to determine the coherent-peak counts is listed below. Line 220 converts the 32 bit unsigned integer into a real number. Lines 130 and 140 determine the start and end of the region of interest. The size of this region can be varied (lines 150 and 160).

```
10 REM DETERMINATION OF COHERENT PEAK COUNTS
20 DIM R(6,6),S(6),XM(6),X(6,100)
30 DIM A$(4),A(11)
40 DIM UN(6),RY(6),IK(6),JK(6)
50 DIM CHIG1(5),CHIG2(5),CHIH1(5),CHIH2(5)
60 DIM CH(100),Y(100),SG(100)
70 REM this section inputs the roi from the pcmca file
80 INPUT "input file",FI$
90 FI$=FI$+".dat"
100 FOR I=1 TO 4: A(I)=2^(8*I-8): NEXT I
110 OPEN FI$ AS #1 LEN=4
120 FIELD #1, 1 AS A$(1), 1 AS A$(2), 1 AS A$(3), 1 AS A$(4)
130 GET #1,156: LPT=ASC(A$(1))+ASC(A$(2))*A(2)
140 GET #1,206: HPT=ASC(A$(3))+ASC(A$(4))*A(2)
150 PRINT "low end ";LPT,"high end ";HPT
160 INPUT "new low end ",LPT
170 NPTS%=HPT-LPT+1
180 NPTS%=0
190 REM this gets the low and high points demarcating the roi
200 FOR J=LPT TO HPT: JF=J+256: GET #1,JF: B=0
210 REM this converts the 32 bit unsigned integer into real number
220 FOR I=1 TO 4: B=B+ASC(A$(I))*A(I): NEXT I
230 IF B=0 THEN GOTO 290
240 REM  ** ch(pts) stores the channel number, y is the channel   **
250 REM  ** number contents and SG is the inverse of the variance **
260 REM  ** of the channel contents (in doing the fits the counts **
270 REM  ** are weighted by the  variance                         **
280 NPTS%=NPTS%+1: J%=J+1-LPT: CH(NPTS%)=J%: SG(NPTS%)=1/B: Y(NPTS%)=B
290 NEXT J: CLOSE #1
300 INPUT "CENTRE OF GAUSSIAN ",CH0: INPUT "WIDTH OF GAUSSIAN ",CHW
310 CH0=CH0+1-LPT
320 INPUT "Centre grid size ",CHG: INPUT "Width grid size ",WG
330 FOR I=1 TO 3: CHIG2(I)=CHW: CHIG1(I+2)=CH0: NEXT I
340 CHIG2(4)=CHW-WG: CHIG2(5)=CHW+WG
350 CHIG1(1)=CH0-CHG: CHIG1(2)=CH0: CHIG1(3)=CH0+CHG
360 INPUT "ORDER OF POLYNOMIAL ",OP
370 FOR IG=1 TO 5: CH0=CHIG1(IG): CHW=CHIG2(IG): GOSUB 400
380 GOSUB 1550: NEXT IG
390 GOTO 1630
400 FOR I=1 TO OP: FOR J=1 TO NPTS%: X(I,J)=CH(J)^I: NEXT J: NEXT I
410 FOR J=1 TO NPTS%: X(OP+1,J)=EXP(-((CH(J)-CH0)/CHW)^2): NEXT J
420 FOR J=1 TO NPTS%: X(OP+2,J)=1/CH(J): NEXT J
430 REM NOW THE FITTING WILL PROCEED
440 REM sets up sums for the matrix
450 YM=0: FOR I=1 TO NPTS%: YM=YM+Y(I): NEXT I: YM=YM/NPTS%
460 FOR J=1 TO OP+2: XM(J)=0: FOR I=1 TO NPTS%: XM(J)=XM(J)+X(J,I): NEXT I
470 XM(J)=XM(J)/NPTS%: NEXT J
480 SY=0: FOR I=1 TO NPTS%: SY=SY+SG(I)*(Y(I)-YM)^2: NEXT I: SY=SQR(SY)
490 FOR J=1 TO OP+2: S(J)=0: FOR I=1 TO NPTS%: S(J)=S(J)+SG(I)*(X(J,I)-XM(J))^2
500 NEXT I: S(J)=SQR(S(J)): NEXT J
```

```
510 FOR I=1 TO OP+2: FOR J=1 TO OP+2: R(I,J)=0
520 FOR K=1 TO NPTS%: R(I,J)=R(I,J)+SG(K)*(X(I,K)-XM(I))*(X(J,K)-XM(J)): NEXT K
530 R(I,J)=R(I,J)/(S(I)*S(J)): NEXT J: NEXT I
540 GOSUB 930
550 REM given the inverse of r(i,j),now works out the parameters,a
560 FOR J=1 TO OP+2: RY(J)=0: FOR I=1 TO NPTS%
570 RY(J)=RY(J)+SG(I)*(X(J,I)-XM(J))*(Y(I)-YM): NEXT I
580 RY(J)=RY(J)/(S(J)*SY): NEXT J
590 FOR I=1 TO OP+2: A(I)=0: FOR J=1 TO OP+2
600 A(I)=A(I)+RY(J)*R(I,J): NEXT J
610 A(I)=A(I)*SY/S(I): NEXT I
620 A0=0: FOR I=1 TO NPTS%: A00=Y(I): FOR J=1 TO OP+2
630 A00=A00-A(J)*X(J,I): NEXT J: A0=A0+SG(I)*A00: NEXT I
640 A00=0: FOR I=1 TO NPTS%: A00=A00+SG(I): NEXT I
650 YM=A0/A00
660 RETURN
670 REM prints the parameters for the fit at the minimum
680 PRINT "here are the graphs": GOSUB 1370
690 PRINT "the polynomial first":PRINT "order","coefficient","error"
700 FOR I=1 TO OP+2: UN(I)=SQR(R(I,I))/S(I): NEXT I
710 UN0=0: FOR I=1 TO OP+2: FOR J=1 TO OP+2
720 UN0=UN0+XM(I)*XM(J)*R(I,J)/(S(I)*S(J)): NEXT J: NEXT I
730 UN0=UN0+1/A00
740 PRINT 0,YM,UN0: FOR I=1 TO OP: PRINT I,A(I),UN(I):NEXT I
750 PRINT "-1";A(OP+2),UN(OP+2):PRINT
760 PRINT"channel offset ";(LPT-1):PRINT
770 PRINT "THE HEIGHT OF THE GAUSSIAN IS ";A(OP+1);" +- ";UN(OP+1)
780 PRINT "the area is ";A(OP+1)*CHW
790 PRINT"chi-sq ";CHISQ;
800 PRINT "   Reduced ";CHISQ/(NPTS%-OP-3)
810 PRINT: FOR I=1 TO 5: PRINT CHIG1(I),CHIG2(I),CHIH1(I),CHIH2(I): NEXT I
820 PRINT "centre ";CH0+LPT-1,"width ";CHW
830 IF INKEY$="" THEN 830
840 CLS
850 PRINT "want to try again? Y or N "
860 INPUT AN$
870 IF AN$<>"Y" AND AN$<>"y" THEN END
880 PRINT "want the same file? Y or N "
890 INPUT AN$
900 IF AN$="Y" OR AN$="y" THEN GOTO 300
910 GOTO 80
920 REM determines the inverse of the correlation matrix r(i,j)
930 DET=1: DR=OP+2: FOR K=1 TO DR: MAX=0
940 FOR I=K TO DR: FOR J=K TO DR
950 IF ABS(MAX)>ABS(R(I,J)) THEN GOTO 970
960 MAX=R(I,J): IK(K)=I: JK(K)=J
970 NEXT J: NEXT I: IF MAX=0 THEN DET=0: RETURN
980 I=IK(K): IF I<K THEN GOTO 940
990 IF I=K THEN GOTO 1050
1000 FOR J=1 TO DR
```

```
1010 SV=R(K,J)
1020 R(K,J)=R(I,J)
1030 R(I,J)=-SV
1040 NEXT J
1050 J=JK(K): IF J<K THEN GOTO 940
1060 IF J=K THEN GOTO 1120
1070 FOR I=1 TO DR
1080 SV=R(I,K)
1090 R(I,K)=R(I,J)
1100 R(I,J)=-SV
1110 NEXT I
1120 FOR I=1 TO DR: IF I<>K THEN R(I,K)=-R(I,K)/MAX
1130 NEXT I
1140 FOR I=1 TO DR: FOR J=1 TO DR
1150 IF I<>K AND J<>K THEN R(I,J)=R(I,J)+R(I,K)*R(K,J)
1160 NEXT J: NEXT I
1170 FOR J=1 TO DR: IF J<>K THEN R(K,J)=R(K,J)/MAX
1180 NEXT J
1190 R(K,K)=1/MAX
1200 DET=DET*MAX: NEXT K
1210 FOR L=1 TO DR: K=DR+1-L: J=IK(K)
1220 IF J<=K THEN GOTO 1280
1230 FOR I=1 TO DR
1240 SV=R(I,K)
1250 R(I,K)=-R(I,J)
1260 R(I,J)=SV
1270 NEXT I
1280 I=JK(K)
1290 IF I<=K THEN GOTO 1350
1300 FOR J=1 TO DR
1310 SV=R(K,J)
1320 R(K,J)=-R(I,J)
1330 R(I,J)=SV
1340 NEXT J
1350 NEXT L: RETURN
1360 REM plots the data and the background for comparison
1370 YMX=0: FOR I=1 TO NPTS%: IF Y(I)>YMX THEN YMX=Y(I)
1380 NEXT I: CLS: SCREEN 2: YMX=200/YMX: XINC=INT(600/NPTS%): CHISQ=0
1390 X1=2-XINC: KEY OFF: FOR I=1 TO NPTS%: X1=X1+XINC: Y1=200-Y(I)*YMX
1400 LINE (X1,Y1-1)-(X1,Y1+1): LINE (X1-1,Y1)-(X1+1,Y1): NEXT I
1410 Y0=YM: FOR J=1 TO OP+2: Y0=Y0+A(J)*X(J,1): NEXT J
1420 CHISQ=CHISQ+SG(1)*(Y(1)-Y0)^2: Y0=200-Y0*YMX
1430 X0=2: FOR I=2 TO NPTS%: X1=X0+XINC
1440 Y1=YM: FOR J=1 TO OP+2: Y1=Y1+A(J)*X(J,I): NEXT J
1450 CHISQ=CHISQ+SG(I)*(Y(I)-Y1)^2
1460 Y1=200-Y1*YMX: LINE (X0,Y0)-(X1,Y1): X0=X1: Y0=Y1: NEXT I
1470 Y0=200-Y(1)*YMX: X0=2: FOR I=2 TO NPTS%: X1=X0+XINC: Y1=YM
1480 FOR J=1 TO OP: Y1=Y1+A(J)*X(J,I): NEXT J: Y1=Y1+A(OP+2)*X(OP+2,I)
1490 Y1=200-Y1*YMX: LINE (X0,Y0)-(X1,Y1): X0=X1: Y0=Y1: NEXT I
1500 LOCATE 1,1: PRINT FI$
```

```
1510 IF INKEY$="" THEN 1510
1520 SCREEN 0: PRINT: PRINT
1530 PRINT "here are the parameters":PRINT:RETURN
1540 REM determines chisq at grid point
1550 CHIH2(IG)=A(OP+1)
1560 CHISQ=0
1570 FOR I=1 TO NPTS%: Y1=YM
1580 FOR J=1 TO OP+2: Y1=Y1+A(J)*X(J,I): NEXT J
1590 CHISQ=CHISQ+SG(I)*(Y(I)-Y1)^2
1600 NEXT I
1610 CHIH1(IG)=CHISQ/(NPTS%-OP-3)
1620 PRINT CHIG1(IG),CHIG2(IG),CHIH1(IG),CHIH2(IG): RETURN
1630 D3=CHIH1(2)
1640 D1=CHIH1(1)+CHIH1(3)-2*D3: D1=D1/2
1650 D2=CHIH1(3)-D1-D3
1660 CHO=CHIG1(2)-CHG*D2/(2*D1)
1670 D1=CHIH1(4)+CHIH1(5)-2*D3: D1=D1/2
1680 D2=CHIH1(5)-D1-D3
1690 CHW=CHIG2(2)-WG*D2/(2*D1)
1700 GOSUB 400: GOTO 680
```

APPENDIX 2

THE COMMON VOLUME OF TWO CONES

The scattering volume is defined by the intersection of the projections of the source and detector collimators. It can be determined as follows. Consider a cone lying at the origin in the y-z plane with its central axis coincident with the z axis. The general equation of a surface of a cone in space is given by:

$$Ax^2 + By^2 + Cz^2 + Dxy + Eyz + Fzx + Gx + Hy + Jz + K = 0 \qquad (A2.1)$$

and the equation of the cone is

$$x^2 + y^2 - \tan^2\alpha z^2 = 0 \qquad (A2.2)$$

where α is the half cone angle. If a cone in the x", y", z" coordinate system figure A2.1(i), is now rotated about the x" axis through angle ϕ in the same plane, its new coordinate (x′,y′,x′) figure A2.1(ii), are related to the old coordinates by

$$z'' = z'\cos\phi - y'\sin\phi \qquad (A2.1)$$

$$y'' = z'\sin\phi + y'\cos\phi \qquad (A2.3.2)$$

$$x'' = x' \qquad (A2.3.3)$$

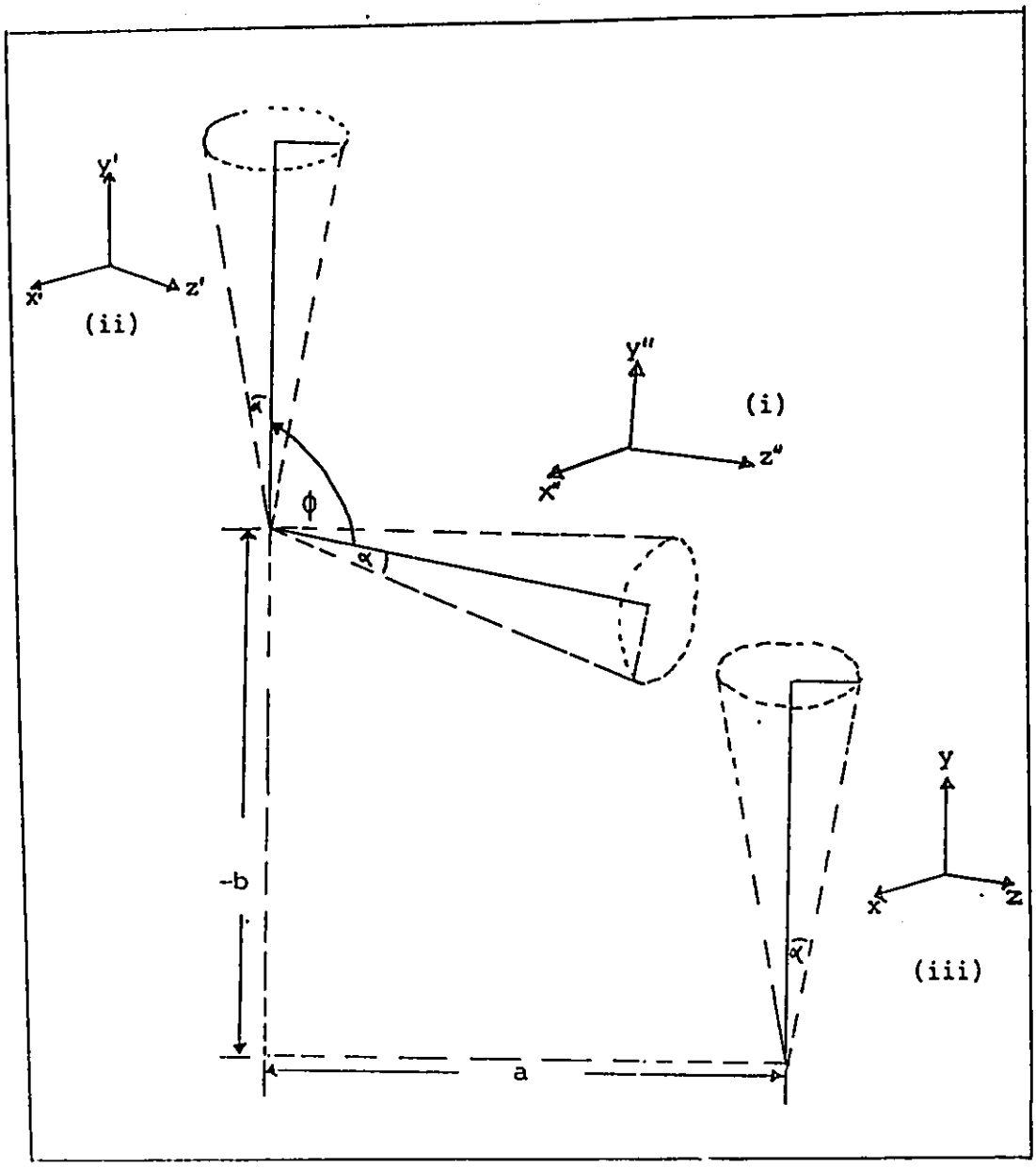

Figure A2.1 Illustration of rotation of the cone through angle ϕ,(i) to (ii) and translation to (0,-b,a),(ii) to (iii).

and the equation of the cone is now

$$x''^2 + y''^2 = \tan^2\alpha z''^2 \qquad \text{(A2.4)}$$

Substituting equations (A2.3) into equation 2.2, gives the equation of the cone rotated by angle ϕ from the original position.

$$(x')^2 + (z'\sin\phi + y'\cos\phi)^2 - [\tan\sigma(z'\cos\phi - y'\sin\phi)]^2 = 0 \qquad \text{(A2.5)}$$

If the cone is now translated to a position (o,a,-b) figure A2.1(iii), the new coordinates (x,y,z) are related to the previous coordinates (x',y',z') by:

$$z' = (z + a) \qquad \text{(A2.6.1)}$$

$$y' = (y - b) \qquad \text{(A2.6.2)}$$

$$x' = x \qquad \text{(A2.6.3)}$$

Substituting equations (A2.6) into equation (A2.5) gives the general equation of the cone rotated and translated to position (0,a,-b) is

$$\begin{aligned} x^2 &+ (z-a)^2 \sin\phi + 2(z-a)(y+b) \sin\phi \cos\phi \\ &+ (y+b)^2 \cos^2\phi - \tan^2\alpha [(z-a)^2 \cos^2 \phi] \\ &- 2(z-a)(y+b) \sin\phi \cos\phi + (y+b)^2 \sin^2\phi = 0 \end{aligned} \qquad \text{(A2.7)}$$

Equation (A2.7) can be expanded and re-arranged in a form similar to equation (A2.1). The cross terms in x arise from the rotation of the cone. Since x is unchanged any such

terms must be zero. The coefficients A, B, C etc., from equation (A2.7), are as follows:

$$A = 1, \quad B = \cos^2\phi - \tan^2\alpha \sin^2\phi$$
$$C = \sin^2\phi - \tan^2\alpha \cos^2\phi, \; D = G = F = 0$$
$$E = -2\sin\phi \cos\phi (1 + \tan^2\alpha)$$
$$H = 2b \cos\phi - 2a\tan^2\alpha \sin\phi$$
$$J = -2b\sin\phi - 2a\tan^2\alpha \cos\phi$$
$$K = b^2 - a^2\tan^2\alpha$$

Therefore the equation of the cone is now

$$\begin{aligned} & x^2 + y^2(\cos^2\phi - \tan^2\alpha \sin^2\phi) + z^2(\sin^2\phi - \tan^2\alpha \cos^2\alpha) \\ & - yz(2\sin\phi \cos\phi (1 + \tan^2\alpha) + y(2b \cos\phi - 2a\tan^2\alpha \sin\phi) \\ & - z(2b\sin\phi - 2a\tan^2\alpha \cos\phi + b^2 - a^2 \tan^2\alpha \\ & = 0 \end{aligned} \qquad \text{(A2.8)}$$

Now consider a second cone lying in the original position of the first cone and whose defining equation is given by equation (A2.2). The volume of intersection of the two cones can be determined using a Monte Carlo method by sampling isotropically distributed points in an arbitrary volume V which includes the intersection. Consider such a point (x,y,z). It will lie in the volume of intersection if the following relations are satisfied.

i) $x^2 + y^2 - \tan^2\alpha z^2 < 0$ (A2.9.1)

ii) Equation (A2.8) < 0 (A2.9.2)

Relations (A2.9.1) and (A2.9.2) refer to cones 2 and 1 respectively as indicated in figure A2.2.

The volume of intersection, V_I, is given by

$$V_I = \frac{\text{number of points satisfying A2.9.1 and A2.9.2}}{\text{total number of random points}} \times \text{volume, V.} \qquad \text{(A2.10)}$$

The arbitrary volume V in equation A2.10 was the volume of cone 1 between the planes Z_{max} and Z_{min}, with Z_{max} and Z_{min} the extreme values of Z that could lie within the volume of intersection. These were determined by finding the coordinates of the vertices of the quadrilateral ABCD, formed by the intersection of the x=0 plane with the volume of intersection. The values of the z coordinates were determined by setting x=0 in equation (A2.2) which yielded the results.

$$y = \tan\alpha Z \qquad \text{(A2.11.1)}$$

$$y = -\tan\alpha Z \qquad \text{(A2.11.2)}$$

These were substituted into equation (A2.8), with x=0 and solved yielding four values of Z. The Z_{max} and Z_{min} values were chosen from these.

The random points (x,y,z) were chosen by first selecting a value Z_p between Z_{max} and Z_{min} and randomly

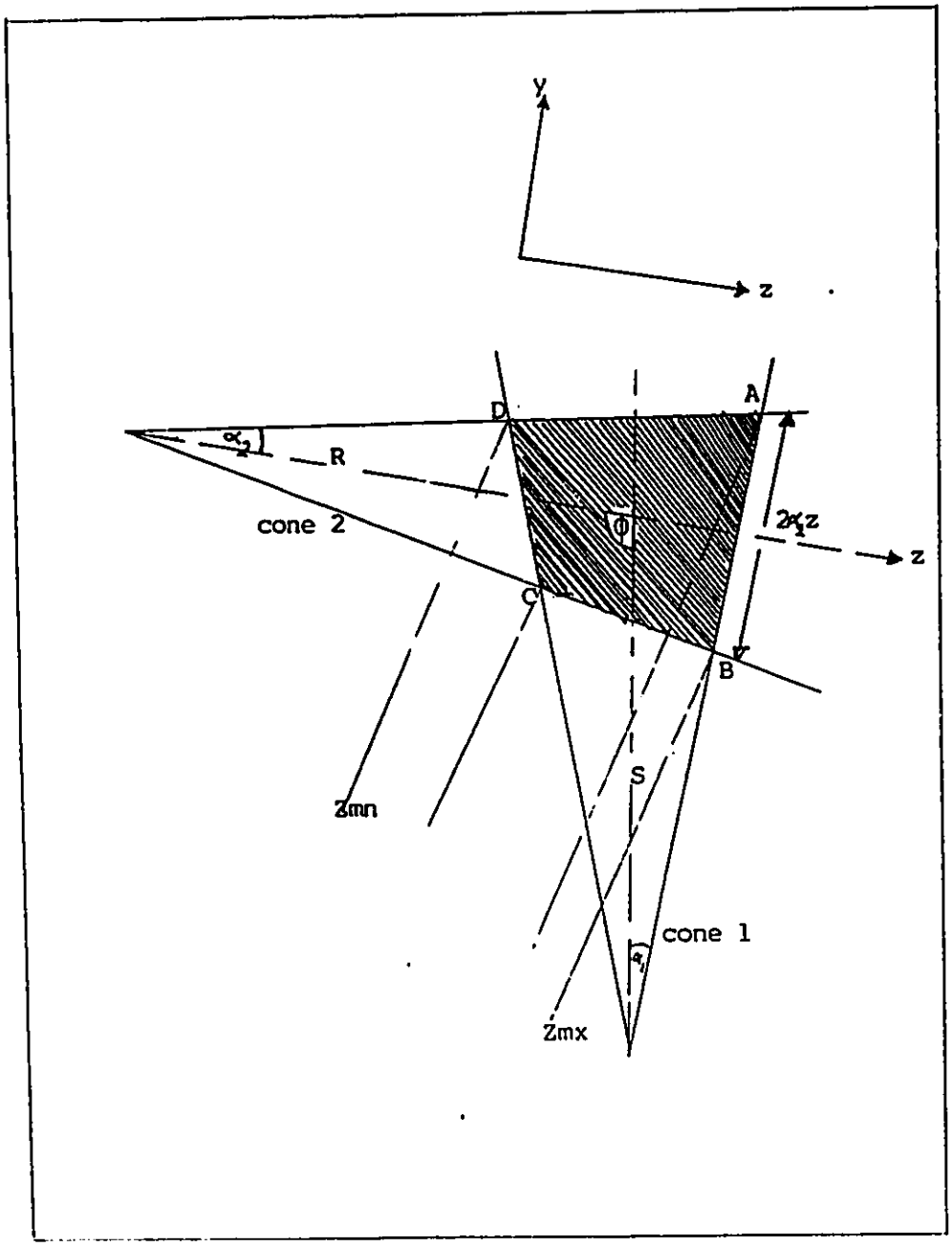

Figure A2.2 Determination of Zmn and Zmx

choosing a point x,y within the circle.

$$x^2 + y^2 \leq \tan^2\alpha z_p^2 \qquad \text{(A2.12)}$$

Z_p was chosen using the inverse of the cumulative probability distribution function, CDF, for Z. The probability that a point will be at Z_p is proportional to the area of the cone at Z_p, $\pi\tan^2\alpha Z_p^2$. The normalised CDF is given by:

$$CDF(Z) = \frac{\int_{Z_{mn}}^{Z_p} z_p^2\, dZ}{\int_{Z_{mn}}^{Z_{mx}} z_p^2\, dZ} = \frac{Z^3 - Z_{mn}^3}{Z_{mx}^3 - Z_{mn}} \qquad \text{(A2.13)}$$

Z_p was generated using a random number R by

$$Z_p = [(Z_{mx}^3 - Z_{mn}^3)R + Z_{mn}^3]^{1/3} \qquad \text{(A2.14)}$$

In the programme R is RND (lines 820, 830), Z_{mn}^3 is Z0 (line 730) and Z_p is Z line 800.

A point (x_p,y_p) in the plane $Z=Z_p$ was chosen within a square centred at the origin, with sides $2\tan\alpha Z_p$ using

$$x_p = \tan\alpha\ Z_p\ (2R-1) \qquad \text{(A2.15)}$$

$$y_p = \tan\alpha\ Z_p\ (2R-1) \qquad \text{(A2.16)}$$

They were rejected if

$$x_p^2 + y_p^2 > \tan^2\alpha\ z_p^2 \qquad \text{(A2.17)}$$

and new x_p and y_p values were chosen.

Since the points (x_p, y_p, z_p) were chosen to be within cone 2, it sufficed to check if condition (A2.9.2) was satisfied to determine if the point was in the volume of intersection.

The following programme was written to compute the common volume of two cones. The half cone angles α_1 and α_2, are represented by u and v in the programme. They need not be the same magnitude and the cone apex to point of intersection distances for the detector and source cones are R and S respectively. Note that

$$a = R + S \cos\phi \qquad \text{(A2.18)}$$

$$b = S \sin\phi \qquad \text{(A2.19)}$$

```
10 REM: DETERMINATION OF THE COMMON VOLUME OF TWO CONES
20 REM: BY A MONTE CARLO METHOD.
30 DIM PHIFL(18)
40 PHIFL(1)=20: PHIFL(2)=30: PHIFL(3)=40: PHIFL(4)=50
50 PHIFL(5)=60: PHIFL(6)=80: PHIFL(7)=90: PHIFL(8)=100
60 PHIFL(9)=102: PHIFL(10)=110: PHIFL(11)=119: PHIFL(12)=120
70 PHIFL(13)=130: PHIFL(14)=140: PHIFL(15)=150: PHIFL(16)=155
80 PHIFL(17)=160: PHIFL(18)=165
90 DIM ZL(4)
100 INPUT "filename",F$: OPEN F$ FOR OUTPUT AS #1
110 INPUT "ENTER THE NUMBER OF POINTS ",IP
120 INPUT "enter the number of repeats",REP
130 INPUT "ENTER DISTANCE D1",R
140 INPUT "ENTER DISTANCE D2",S
150 FOR IANG=1 TO 18: T=PHIFL(IANG): WRITE #1,T
160 U=4.68
170 C=.017453292#
180 T=T*C
190 V=5.62
200 U=U*C
210 V=V*C
220 A1=R-S*COS(T)
230 B1=S*SIN(T)
240 W= SIN(T)
250 T= COS(T)
260 U= TAN(U)
270 V= TAN(V)
280 A=1
290 B=T*T-V*V*W*W
300 C=W*W-V*V*T*T
310 D=0
320 E=-2*W*T*(1+V*V)
330 F=0
340 G=0
350 H=2*B1*T-2*A1*V*V*W
360 J=-2*B1*W-2*A1*V*V*T
370 K=B1*B1-A1*A1*V*V
380 A2=C+B*U*U+E*U
390 B2=J+H*U
400 C2=K
410 D2=B2*B2-4*A2*C2
420 IF D2<0 GOTO 470
430 D2=SQR(D2)
440 ZL(1)=(-B2+D2)/(2*A2)
450 ZL(2)=(-B2-D2)/(2*A2)
460 GOTO 490
470 ZL(1)=0
480 ZL(2)=0
490 A2=A2-2*E*U
500 B2=B2-2*H*U
```

```
510 D2=B2*B2-4*A2*C2
520 IF D2<0 THEN GOTO 570
530 D2=SQR(D2)
540 ZL(3)=(-B2+D2)/(2*A2)
550 ZL(4)=(-B2-D2)/(2*A2)
560 GOTO 590
570 ZL(3)=0
580 ZL(4)=0
590 FOR I=1 TO 4: PRINT ZL(I):NEXT I
600 FOR I=1 TO 4
610 IF ZL(I)<=0 THEN GOTO 650
620 ZMN=ZL(I)
630 ZMX=ZL(I)
640 GOTO 660
650 NEXT I
660 FOR I=1 TO 4
670 IF ZL(I)<=0 THEN GOTO 700
680 IF ZL(I)<ZMN THEN ZMN=ZL(I)
690 IF ZL(I)>ZMX THEN ZMX=ZL(I)
700 NEXT I
710 PRINT ZMN,ZMX
720 ZRG=ZMX-ZMN
730 Z0=ZMN^3: Z1=ZMX^3-Z0
740 III=0
750 VOLMN=0: VOLSQ=0: IIMN=0
760 CRT=1/3
770 FOR IK=1 TO REP: III=0
780 RANDOMIZE VAL(RIGHT$(TIME$,2))
790 FOR II=1 TO IP
800 Z=(RND*Z1+Z0)^CRT
810 YRG=Z*U
820 Y=YRG*(2*RND-1)
830 X=YRG*(2*RND-1)
840 ZS=Z*Z
850 YS=Y*Y
860 XS=X*X
870 IF XS+YS>YRG^2 THEN GOTO 820
880 W=A*XS+B*YS+C*ZS+D*X*Y+E*Y*Z+F*X*Z+G*X+H*Y+J*Z+K
890 IF W<0 THEN III=III+1
900 NEXT II
910 VOL=Z1*U^2*3.1416*III/(3*IP)
920 WRITE #1,"VOLUME ";VOL,"using ";III;" pointe"
930 VOLMN=VOLMN+VOL: VOLSQ=VOLSQ+VOL^2: IIMN=IIMN+III
940 NEXT IK
950 VOLMN=VOLMN/REP: IIMN=IIMN/REP
960 WRITE #1,"mean volume ";VOLMN,"using ";IIMN;" pointe"
970 VOLSQ=VOLSQ-REP*VOLMN^2: VOLSQ=SQR(VOLSQ/(REP-1))
980 WRITE #1,"stan. dev. ",VOLSQ
990 NEXT IANG
```

APPENDIX 3

SIMULATION OF SCATTER RATIOS

Introduction

This simulation was undertaken to verify the attenuation correction procedure. The approach used here is an extension of the technique used to determine the scattering volume. First the geometry (volume) of scatter is determined as in Appendix 2, and then the probability of scatter is obtained using randomly generated points within this volume. Second, the transmission probability is determined and the scatter ratio is obtained as a quotient of the two probabilities.

Scatter probabilities

The probability of scatter is calculated with the aid of figure A3.1, in which p is a scattering point inside the scattering volume and in the solution. S_1 and S_0 are the distances from the point of scatter to the detector and source. S_2 and S_4 are distances within the solution container, to and from the point of scatter respectively. The sum of the distances S_2 and S_4 is set equal to ℓ, the attenuation path length. The cylindrical solution container has a radius of r. The angle θ_p is the angle from the

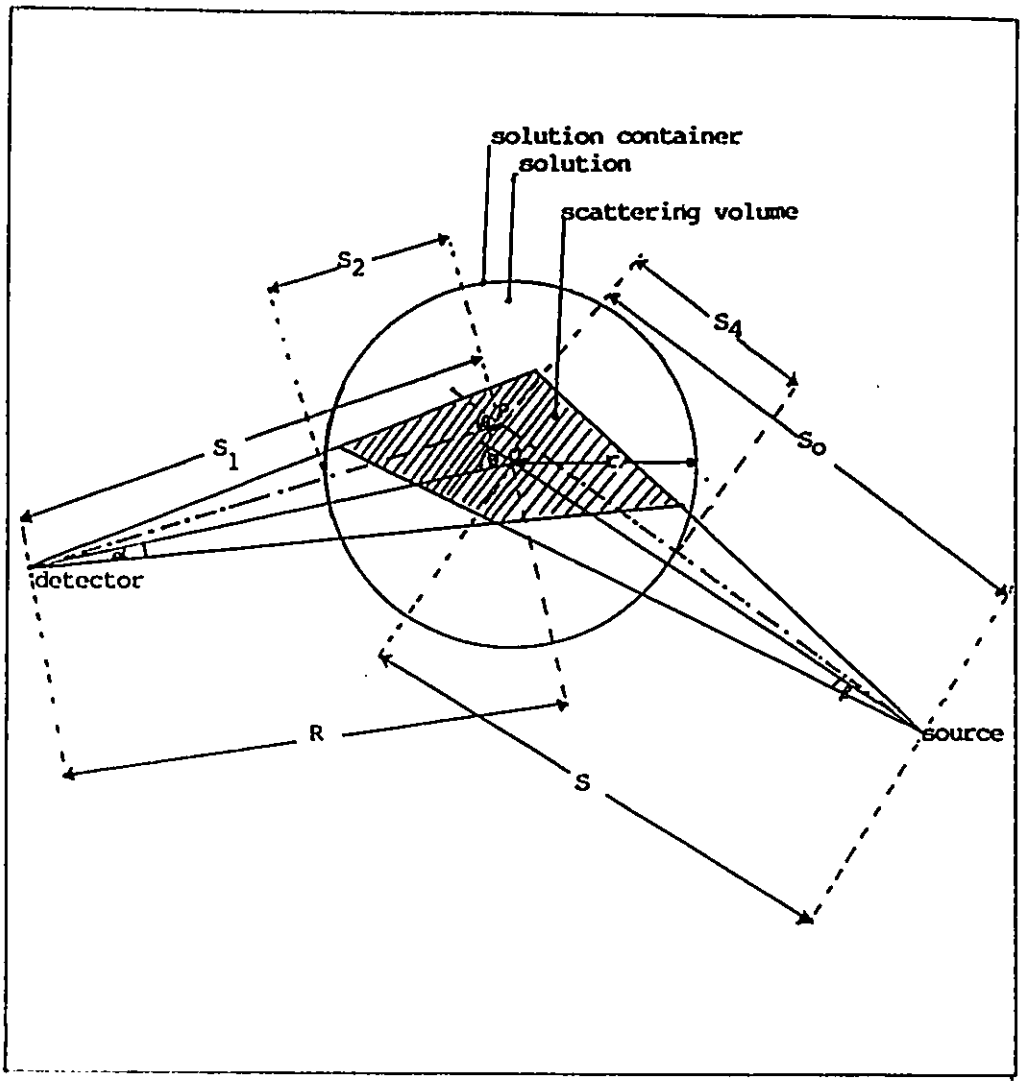

Figure A3.1 Determination of the scattering probability

scattering point, p, required to ensure that the scattered photon enters the detector "cone". θ_p is therefore the "local" scattering angle for the given scattering location.

The probability of a photon being coherently scattered at a given value of θ is given by:

$$P_S(\theta) = nv \langle\sigma\rangle \qquad \text{(A3.1)}$$

where n is the number of atoms per unit volume for a solution of a given physical density and v is the scattering volume (determined by the Monte Carlo method detailed in Appendix 2). $\langle\sigma\rangle$ is the mean probability per atom per photon and is given by:

$$\langle\sigma\rangle = \frac{\int_V \frac{d\sigma_{coh(\theta)}}{d\Omega} e^{-\mu\ell} \phi(v)}{v} \, d\Omega \, DR \, dv \qquad \text{(A3.2)}$$

where $\phi(V)$ is the photon flux density and for constant flux $\phi(V)$ is simply ϕ and can be approximated as the inverse of the beam area at the centre of rotation. ℓ is the attenuation path length and is the sum of S_2 and S_4; μ is the total linear attenuation coefficient at a given solution density and the values are given in Table A3.1; $d\Omega$ is the solid angle subtended by the detector; DR is the detector response. The differential coherent cross section, $[d\sigma_{coh(\theta)}]/d\Omega$ is given by the expression

Table A3.1 100 keV interaction macroscopic cross-sections for K_2HPO_4; $\Sigma_{total} = \Sigma n_i \sigma_i \times 10^{-3}$ cm^{-1}

solution density (grams/cm)	coherent	photo-electric	Compton	Total
1.00 water	5.4175	2.8538	162.725	170.996
1.11	7.7041	8.9042	177.570	194.178
1.24	10.177	15.322	195.534	221.034
1.42	13.970	25.485	219.326	258.781

n_i = number of atoms per unit of solution volume for element i

σ_i = interaction cross-section per atom (barns/atom) for element i for given process.

Values of σ were obtained from, Veigele, 1973.

$(1/2)r_e^2(1+\cos^2\theta)FF_{eff}^2$ where r_e is the classical electron radius (2.82×10^{-13}cm); θ is the angle between the cones and FF_{eff}^2 is the square of the effective form-factor for the average scattering atom in the solution. It is given by the expression $FF_{eff}^2 = \Sigma n_i FF_i^2 / \Sigma n_i$, where n_i is the number of atoms of element i per unit volume and FF_i is the form factor for element i. Table A3.2 lists values of form-factor squared, FF_i^2 for hydrogen, oxygen, phosphorus and potassium for 100 keV photons at various scatter angles. Thus FF_{eff}^2 is a function of scattering angle and solution density. Values for FF_{eff}^2 for the K_2HPO_4 soluations have been tabulated in Table A3.3 for the same values of momentum transfer. For values of θ in between those tabulated in table A3.3, FF_{eff}^2 values are obtained by linear interpolation.

Transmission probability

The transmission geometry is shown in figure A3.2 from which it can be seen that

$$w = \pi - 2\phi$$

so that

$$\sin w = \sin 2\phi$$

and

$$\cos \phi = \cos(\pi - \phi_0).$$

Table A3.2 Momentum transfer and form-factors for 100 keV photons

Atomic Form-factor Square $[FF(x,Z)]^2$

m.tr. "x"	cor.sct. angle θ	H	O	P	K
1.00	13.78	4.750 E-5	1.8942	9.6721	23.3705
1.25	17.25	8.970 E-6	1.3971	4.9107	13.0321
1.50	20.74	2.230 E-6	0.9922	3.0203	7.2399
2.00	27.77	2.400 E-7	0.4516	1.7654	3.0113
2.50	34.92	4.140 E-8	0.1951	1.2486	1.8433
3.00	42.20	9.804 E-9	0.1014	0.8921	1.4135
3.50	49.67	2.887 E-9	0.0381	0.5055	1.0406
4.00	57.37	9.988 E-10	0.0232	0.4225	0.8030
5.00	73.74	1.689 E-10	0.0045	0.1652	0.4202
6.00	92.11	3.946 E-11	0.0013	0.0696	0.2128

m.tr. = momentum transfer, $x = (1/\lambda)\sin(\theta/2)$

λ = wavelength of incident photons

cor.sc. angle θ = corresponding scattering angle, θ.

Table A3.3 K_2HPO_4 Solutions (in water) and their effective form-factor squared FF^2_{eff}

		Solution density (grams/cc)			
		1.00 (water)	1.11	1.24	1.42
m.tr. "x"	sct. angle	FF^2_{eff}	FF^2_{eff}	FF^2_{eff}	FF^2_{eff}
1.00	13.78	0.6314	0.9554	1.2814	1.8240
1.25	17.25	0.4657	0.6470	0.8283	1.1305
1.50	20.74	0.3307	0.4351	0.5388	0.7121
2.00	27.77	0.1505	0.1971	0.2433	0.3205
2.50	34.92	0.0650	0.0937	0.1224	0.1702
3.00	42.20	0.0338	0.0549	0.0763	0.1118
3.50	49.67	0.0127	0.0276	0.0427	0.0678
4.00	57.67	0.0077	0.0190	0.0304	0.0494
5.00	73.74	0.0015	0.0070	0.0126	0.0219
6.00	92.11	0.0004	0.0031	0.0059	0.0105

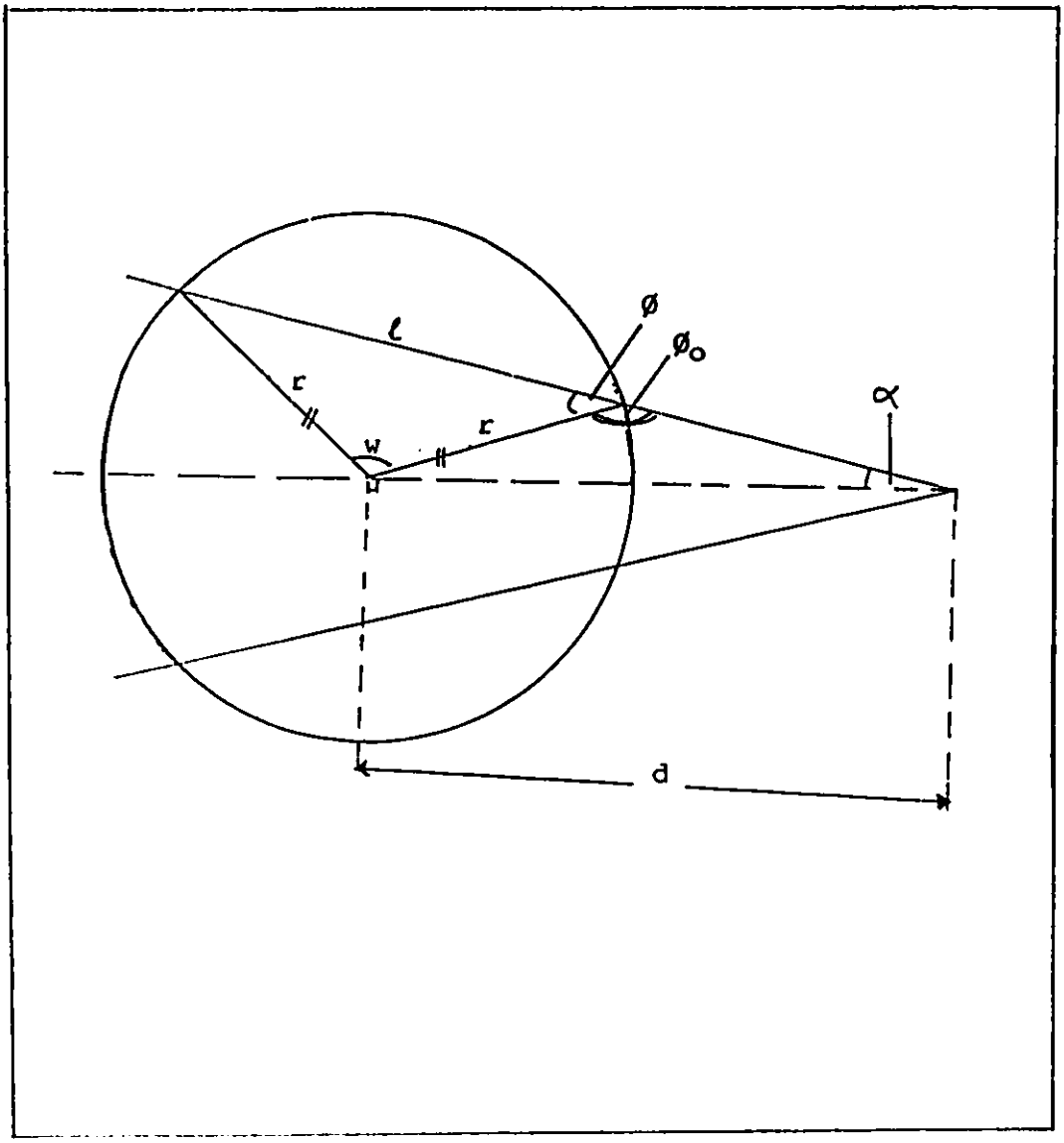

Figure A3.2 The transmission geometry. (Beam divergence has been exaggerated for clarity.)

It can also be shown that

$$\ell = r\sin 2\phi/\sin\phi.$$

To obtain the 2 average value of $\exp(-\mu\ell)$ We wish to obtain an expression for ℓ in terms of r, α and d. From geometrical considerations it can be shown that:

$$d/\sin\phi_0 = r/\sin\alpha$$

or

$$\sin\phi_0 = \sin\alpha d/r$$

It follows that

$$\ell = 2r\cos\phi$$

$$= 2\sqrt{(r^2 - \sin^2\alpha d^2)}$$

$$= 2r\sqrt{(1 - \sin^2\phi_0)}$$

$$= 2r\sqrt{(1-(\sin^2\alpha d^2/d^2))}$$

The average attenuation factor, $\langle e^{-\mu\ell}\rangle$ is given by:

$$\langle e^{-\mu l}\rangle = \frac{\int_0^{\alpha_{max}} e^{(-\mu 2\sqrt{r^2-d^2\sin^2\alpha})}\, 2\pi \sin\alpha\, d\alpha}{\int_0^{\alpha_{max}} 2\sqrt{\ } \sin\alpha\, d\alpha} \qquad (A3.3)$$

In the above equation α_{max} is obtained from the relation:

$\alpha_{max} = \alpha_1 =$ arc tan[detector collimator internal radius/(R + S)] where R is the detector-to-centre-of-

rotation distance and S is the source-to-centre-of-rotation distance.

The denominator of equation (A3.3) is simply $1-\cos\alpha_{max}$ and the integrand

$$\int_0^{\alpha_{max}} e^{(-\mu 2\sqrt{(r^2-d^2\sin^2\alpha)}} \sin\alpha \, d\alpha$$

is obtained numerically as part of the computer programme.

Figure A3.3 shows that only a fraction $P(\alpha_1)$ of the flux emitted by the collimated source reaches the detector. This fraction is given by:

$$P(\alpha_1) = \frac{\int_0^{\alpha_1} 2\pi \, \alpha \, \exp-(\alpha/\sigma)^2 \, d\alpha}{\int_0^{\infty} 2\pi \, \alpha \, \exp-(\alpha/\sigma)^2 \, d\alpha}$$

$$= 1 - [\exp-(\alpha_1/\sigma)^2] \qquad \text{(A3.4)}$$

where α is the polar angle, σ is the angle obtained from the beam divergence (FWHM) and α_1 is equivalent to α_{max}.

The probability of transmission, per photon, is given by:

$$P_t = \langle e^{-\mu\ell} \rangle \cdot P(\alpha_1) \qquad \text{(A3.5)}$$

The quotient of equation (A3.1) divided by equation (A3.5) gives the scatter ratio.

The computer programme that follows, was written to

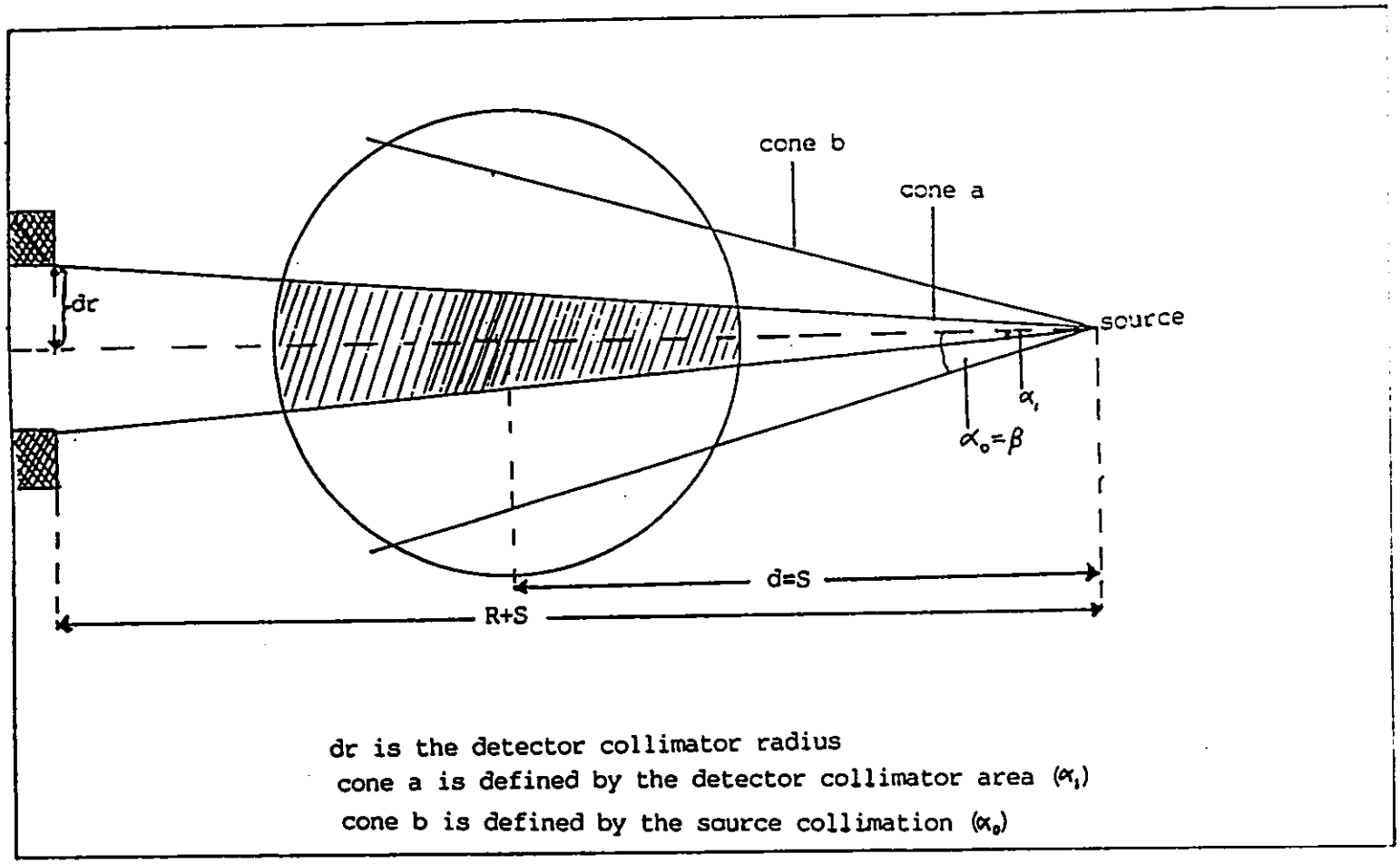

Figure A3.3 Illustrating the derivation of the factor $P(\alpha_1)$.

calculate this scatter ratio as a function of K_2HPO_4 solution density (hence effective atomic number) and solution container diameter, at the scattering angle of 40^{o}.

```
10 REM: calculation of scatter ratios using r and s equal
20 REM: to 7.60 and 6.58cm respectively
30 REM
40 DIM FFS(10),ANG(10),CT(9),ZL(4),RAD1(4),DTSET(4),SCT(2)
50 GOSUB 2120
60 INPUT "enter the number of points for volume ",IP
70 INPUT "enter the step size for the transmission ",STSZ
80 INPUT "output filename ",FOUT$: OPEN FOUT$ FOR OUTPUT AS #1
90 FOR DS%=1 TO 4
100 FOR RD%=1 TO 4
110 FOR SC%=1 TO 2
120 GOSUB 1150
130 GOSUB 310
140 GOSUB 920
150 VOL=4*ZRG*YRG*YRG*(IP1+III)/IP
160 IF III+IP1=0 THEN SCATPR=999: GOTO 180
170 SCATPR=CRSX#*VOL*ETA*1.0014/(III+IP1)
180 GOSUB 1560
190 PRINT #1,"density ";DTSET(DS%)
200 PRINT #1,"radius ";RAD1(RD%)
210 PRINT #1,"scattering angle ";SCT(SC%)
220 PRINT #1,"scatter volume is ";VOL: BEEP
230 IF III+IP1=0 THEN PRINT #1,"fraction is n/a": GOTO 250
240 PRINT #1,"fraction of scatter volume in cylinder is ";III/(IP1+III)
250 PRINT #1,"scatter probability/photon ";SCATPR
260 PRINT #1,"using ";III;" photons"
270 PRINT #1,"transmission probability/photon ";SUM*.1903
280 PRINT #1,"scatter/trans ratio ";SCATPR/(SUM*.1903)
290 PRINT DTSET(DS%),RAD1(RD%),SCT(SC%): NEXT SC%,RD%,DS%
300 CLOSE #1: END
310 REM determines the geometry of scatter
320 T=SCT(SC%): T=180-T
330 U=4.68
340 C=.017453292#
350 T=T*C
360 V=5.62
370 U=U*C
380 R=7.6
390 V=V*C
400 S=6.58
410 A1=R-S*COS(T)
420 B1=S*SIN(T)
430 W= SIN(T): CT(8)=W
440 T= COS(T): CT(9)=-T
450 U= TAN(U)
460 V= TAN(V)
470 A=1
480 B=T*T-V*V*W*W
490 C=W*W-V*V*T*T
500 D=0
```

```
510 E=-2*W*T*(1+V*V)
520 F=0
530 G=0
540 H=2*B1*T-2*A1*V*V*W
550 J=-2*B1*W-2*A1*V*V*T
560 K=B1*B1-A1*A1*V*V
570 A2=C+B*U*U+E*U
580 B2=J+H*U
590 C2=K
600 D2=B2*B2-4*A2*C2
610 IF D2<=0 GOTO 660
620 D2=SQR(D2)
630 ZL(1)=(-B2+D2)/(2*A2)
640 ZL(2)=(-B2-D2)/(2*A2)
650 GOTO 680
660 ZL(1)=0
670 ZL(2)=0
680 A2=A2-2*E*U
690 B2=B2-2*H*U
700 D2=B2*B2-4*A2*C2
710 IF D2<=0 THEN GOTO 760
720 D2=SQR(D2)
730 ZL(3)=(-B2+D2)/(2*A2)
740 ZL(4)=(-B2-D2)/(2*A2)
750 GOTO 780
760 ZL(3)=0
770 ZL(4)=0
780 FOR I=1 TO 4
790 IF ZL(I)<=0 THEN GOTO 830
800 ZMN=ZL(I)
810 ZMX=ZL(I)
820 GOTO 840
830 NEXT I
840 FOR I=1 TO 4
850 IF ZL(I)<=0 THEN GOTO 880
860 IF ZL(I)<ZMN THEN ZMN=ZL(I)
870 IF ZL(I)>ZMX THEN ZMX=ZL(I)
880 NEXT I
890 ZRG=ZMX-ZMN
900 YRG=ZMX*U
910 RETURN
920 REM generates points in space and determines prob. scatter
930 III=0: CRSX#=0: IP1=0
940 FOR II=1 TO IP
950 Z=ZMN+ZRG*RND
960 Y=YRG*(2*RND-1)
970 X=YRG*(2*RND-1)
980 ZS=Z*Z
990 YS=Y*Y
1000 XS=X*X
```

```
1010 W=XS+YS-ZS*U*U
1020 IF W>=0 THEN GOTO 1080
1030 W=A*XS+B*YS+C*ZS+D*X*Y+E*Y*Z+F*X*Z+G*X+H*Y+J*Z+K
1040 IF W>=0 THEN GOTO 1080
1050 W1=SQR(Y*Y+(Z-R)^2)
1060 IF W1>RAD THEN IP1=IP1+1: GOTO 1080
1070 GOSUB 1100
1080 NEXT II
1090 RETURN
1100 REM increments counter of scatters and determines prob. scatter
1110 III=III+1
1120 GOSUB 1730
1130 CRSX#=CRSX#+CRSXIN
1140 RETURN
1150 REM fills tables with form factors
1160 I=DS%: ON I GOTO 1170,1250,1330,1410
1170 MU=.171: ETA=1.00365E+23
1180 RESTORE 1220
1190 FOR I=1 TO 10
1200 READ FFS(I)
1210 NEXT I
1220 DATA .631437,.4657,.33074,.15053,.06503
1230 DATA .0338,.0127,.00773,.00149,.00044
1240 GOTO 1480
1250 MU=.1942: ETA=9.966E+22
1260 RESTORE 1300
1270 FOR I=1 TO 10
1280 READ FFS(I)
1290 NEXT I
1300 DATA .95535,.6469988,.435122,.19708,.09365
1310 DATA .05493,.02757,.01895,.006985,.00314
1320 GOTO 1480
1330 MU=.221: ETA=1.0107E+23
1340 RESTORE 1380
1350 FOR I=1 TO 10
1360 READ FFS(I)
1370 NEXT I
1380 DATA 1.28144,.82828,.53884,.243304,.12236
1390 DATA .07627,.042707,.03038,.012609,.005903
1400 GOTO 1480
1410 MU=.2588: ETA=1.00037E+23
1420 RESTORE 1460
1430 FOR I=1 TO 10
1440 READ FFS(I)
1450 NEXT I
1460 DATA 1.8240,1.1305,.71205,.3205,.17019
1470 DATA .11175,.06783,.04935,.02193,.01048
1480 RESTORE 1520
1490 FOR I=1 TO 10
1500 READ ANG(I)
```

```
1510 NEXT I
1520 DATA 13.78,17.25,20.74,27.77,34.92
1530 DATA 42.2,49.67,57.67,73.74,92.11
1540 RAD=RAD1(RD%)
1550 RETURN
1560 REM finds the transmission probability
1570 TMX=1.7*ATN(1)/45: T=TMX
1580 GOSUB 1690
1590 SUM=SINC/2
1600 STSZ0=STSZ*ATN(1)/45
1610 T=STSZ0
1620 WHILE T<TMX
1630 GOSUB 1690
1640 SUM=SUM+SINC
1650 T=T+STSZ0
1660 WEND
1670 SUM=SUM*STSZ0/(1-COS(TMX))
1680 RETURN
1690 REM finds pathlength through the cylinder for transmision prob
1700 SINC=SQR(RAD*RAD-43.296*SIN(T)^2)
1710 SINC=SIN(T)*EXP(-2*MU*SINC)
1720 RETURN
1730 REM finds probability of scatter of photon into detector
1740 CT(1)=X
1750 CT(2)=Y
1760 CT(3)=Z
1770 S0=SQR(CT(1)^2+CT(2)^2+CT(3)^2)
1780 FOR I=1 TO 3
1790 CT(I)=CT(I)/S0
1800 NEXT I
1810 CT(4)=-X
1820 CT(5)=B1-Y
1830 CT(6)=A1-Z
1840 S1=SQR(CT(4)^2+CT(5)^2+CT(6)^2)
1850 FOR I=4 TO 6
1860 CT(I)=CT(I)/S1
1870 NEXT I
1880 CT0=CT(1)*CT(4)+CT(2)*CT(5)+CT(3)*CT(6)
1890 T0=ATN(SQR(1-CT0*CT0)/CT0)
1900 T0=T0*45/ATN(1)
1910 S4=Y*CT(2)+CT(3)*(Z-R)
1920 S2=SQR(S4^2-(CT(2)^2+CT(3)^2)*(Y^2+(Z-R)^2-RAD^2))
1930 S2=(S2+S4)/(CT(2)^2+CT(3)^2)
1940 S4=Y*CT(5)+CT(6)*(Z-R)
1950 S3=SQR(S4^2-(CT(5)^2+CT(6)^2)*(Y^2+(Z-R)^2-RAD^2))
1960 S4=(S3-S4)/(CT(5)^2+CT(6)^2)
1970 FOR JJJ=1 TO 9
1980 IF ANG(JJJ+1)>T0 THEN GOTO 2000
1990 NEXT JJJ
2000 FFSQ=FFS(JJJ)+(T0-ANG(JJJ))*(FFS(JJJ+1)-FFS(JJJ))/(ANG(JJJ+1)-ANG(JJJ))
```

```
2010 CRSXIN=(1+CT0*CT0)*FFSQ*3.97E-26
2020 CRSXIN=CRSXIN*EXP(-MU*(S2+S4))
2030 CT0=ATN(SQR(1-CT(3)*CT(3))/CT(3))
2040 GPR=EXP(-(CT0/.129)^2)
2050 CRSXIN=CRSXIN*GPR
2060 CT(7)=CT(5)*CT(8)+CT(6)*CT(9)
2070 CT0=ATN(SQR(1-CT(7)*CT(7))/CT(7))
2080 GPR=EXP(-(CT0/.108)^2)
2090 CRSXIN=CRSXIN*GPR
2100 CRSXIN=CRSXIN*.557*CT(7)/(S1*S1)
2110 RETURN
2120 REM sets up tables of radii and density
2130 RESTORE 2170
2140 FOR I=1 TO 4
2150 READ RAD1(I)
2160 NEXT I
2170 DATA 1.92,2.50,3.00,3.64
2180 FOR I=1 TO 4
2190 READ DTSET(I)
2200 NEXT I
2210 DATA 1.0,1.11,1.24,1.42
2220 READ SCT(1): READ SCT(2)
2230 DATA 25,40
2240 RETURN
```

APPENDIX 4

DATA RETRIEVAL FROM THE NORLAND 278-A SINGLE PHOTON ABSORPTIOMETRY BONE DENSITOMETER

This work is due to Mr. Kenrick Chin and is reproduced here for completeness.

The Norland Model 278-A Bone Densitometer acquires and saves data internally. It is capable of saving data for archival purposes on 5 1/4-inch magnetic flexible disks via an external Disk Unit connected to the Densitometer. This unit is also used for retrieving stored information. The format of the data recorded on the disk is unknown. Subsequently, another method of retrieving information on the disk was developed.

The densitometer is connected to the Disk Unit via an industry standard RS-232 serial interface. Thus it is possible to intercept the serial data while the Disk Unit is being read. This action is initiated by pressing the MEASURE followed by the READ DISK control buttons.

An IBM Compatible PC computer equipped with an RS-232 Serial Interface is used to intercept the data from the Disk Unit. The Disk Unit is configured as Data Terminal Equipment (DTE) with data transmitted on pin-2 of a standard DB-258 connector. This signal is wired to pin-3 of the DB-

25P connector on the PC serial interface. At this connector, pin-20 DTR (Data Terminal Ready) is connected to pin-6 DSR (Data Set Ready) and pin-8 CD (Carrier Detect). The common Signal Ground connection is made via pin-7 of both connectors.

The programme shown below is used to capture on the PC the information as it is being transferred from the Disk Unit to the Densitometer. Important features of this programme are now explained. The subroutine from lines 470 to 560 clears the PC screen and presents a message with instructions for the user. The serial data format is 19200 baud, no parity checking, and eight data bits. Line 90 is used to open file #1 on the serial communication channel "COM1:" with the data format of 9600 baud, no parity checking, 8 data bits and one stop bit. The data rate of 19200 baud could not have been requested since the MS-BASIC interpreter program only allows a maximum data rate of 9600 baud. Lines 100 to 160 are therefore used to directly change the data rate to the desired 19200 baud.

Data is transmitted as 2194 bytes (8-bit characters) formatted as follows. There are 17 blocks of 128 bytes. Each block is preceded by an additional lead-in byte of decimal value 64. An additional trailing byte (decimal 64) appears after the 17th block.

Densitometric information is contained in the 2nd to

the 17th block whereby each reading is stored as a low-byte, high-byte pair packed consecutively. Thus the data consists of 1024 points, (64 times 16), of 16-bit information.

Program lines 170 to 190 are used to gather 17 blocks of 129 bytes into a strong array A$(). Line 200 reads in the last trailing character and line 210 closes the communication channel.

Program lines 250 to 340 are used to extract the data from the string array A$(). The first block A$(1) is discarded and blocks 2 to 17 are processed. Each block contains 64 data points packed as a lo/hi byte pair. The extracted 16-bit data is stored in a 1024-element integer array D().

The subroutine at lines 380 to 460 is used to graphically show the extracted data points on the video screen of the PC. Since the screen width is too small to accommodate the full 1024-point scan only the last 600 points are shown.

Finally, the subroutine at lines 570 to 700 gives the user the opportunity of saving the data to a PC disk file if desired. If a file name is specified at the prompt then a file by that name is saved. If no name is specified then no file is created. The file created consists of a text file containing 1024 lines of numeric data. This file is used for subsequent data analysis.

```
10 REM *** NORLAND DATA GRABBER ***
20 REM      written by Kenrick Chin
30 REM      24 Mar 1989
40 DIM A$(100),D(1024)
50 NBLOCKS = 17
60 NB = 129
70 N = 1024
80 GOSUB 470
90 OPEN "COM1:9600,N,8,1" AS #1
100 REM --- change baud to 19200 ---
110 ACIA = &H3F8
120 LCR = ACIA + 3
130 LCRDATA = INP(LCR)
140 OUT LCR,128+LCRDATA
150 OUT ACIA,6
160 OUT LCR,LCRDATA
170 FOR B = 1 TO NBLOCKS
180  A$(L) = INPUT$(NB,#1)
190 NEXT B
200 C$ = INPUT$(1,#1)
210 CLOSE #1
220 PRINT
230 PRINT "Data received."
240 PRINT "Crunching numbers, please wait ..."
250 REM --- pack data into array ---
260 I = 1
270 FOR B = 2 TO NBLOCKS
280   FOR J = 1 TO 64
290     LO = ASC(MID$(A$(B),(J*2),1))
300     HI = ASC(MID$(A$(B),(J*2+1),1))
310     D(I) = 256*HI + LO
320     I = I + 1
330   NEXT J
340 NEXT B
350 GOSUB 380
360 GOSUB 570
370 END
380 REM --- plot data ---
390 ISTART = 425
400 Y0 = 199
410 FOR I = ISTART TO N
420   X = I - ISTART
430   Y = Y0 - D(I)
440   PRESET (X,Y),1
450 NEXT I
460 RETURN
470 REM --- set up ---
480 KEY OFF
490 SCREEN 2
500 CLS
```

```
510 PRINT "                    * * * NORLAND DATA GRABBER * * *"
520 PRINT
530 PRINT "waiting for data ..."
540 PRINT "                          press MEASURE"
550 PRINT "                          press READ DISK"
560 RETURN
570 REM --- save data file ---
580 PRINT
590 BEEP
600 INPUT "Name of data file to be saved: ",F$
610 IF F$<>"" GOTO 640
620 PRINT "Data not saved."
630 RETURN
640 OPEN F$ FOR OUTPUT AS #2
650 FOR I = 1 TO N
660   PRINT #2,D(I)
670 NEXT I
680 PRINT
690 PRINT F$; " saved."
700 RETURN
```